Hydrologic Dynamics of Dryland Playas and Their Catchments in the Chihuahuan Desert

by

Charles Robert Kimsal

A Thesis Presented in Partial Fulfillment
of the Requirements for the Degree
Master of Science

Approved June 2023 by the
Graduate Supervisory Committee:

Enrique R. Vivoni, Chair
Kelin X. Whipple
Jiwei Li

ARIZONA STATE UNIVERSITY

August 2023

ABSTRACT

In the southwestern United States, water is a precious resource that influences landscapes and their respective ecosystems. Ephemeral lakes, known as playas, are drainage points for closed or endorheic basins and serve as important locations for plant productivity, biogeochemical processes, and groundwater recharge. In this study, I explore the hydrologic dynamics of eighteen (18) instrumented playas in the Jornada Basin of the Chihuahuan Desert with respect to the drivers of playa inundation and how their behaviors vary in space and time. To this end, I combine water level observations in playas with gauge-corrected radar precipitation estimates to determine hydrologic dynamics over the more than 6-year period of June 2016 to October 2022. Results indicate that all playa inundation events are associated with precipitation and that 76% of events occur during the warm season from April to September that is characterized by the North American monsoon. Mean annual runoff ratios in the playa catchments range from 0.01% to 9.28%. I observe precipitation depth and 60-minute intensity thresholds for playa inundation ranging from 16.1 to 71.3 mm and 8.8 to 40.5 mm/hr, respectively. Although playa inundation is typically caused by high rainfall amounts and intensities, other factors such as antecedent wetness conditions and the spatial variability of rainfall within the playa catchment also play a role. The magnitudes, durations, and occurrence of inundation events vary among playas, but their responses to precipitation generally agree with groupings determined based on their geological origin. Logistic and linear regressions across all playas reveal the relative importance of catchment variables, such as area, sand fraction, slope, and the percentage of bare ground. It is shown that larger catchment areas are strongly associated with a lower likelihood of inundation and higher

precipitation thresholds for inundation. An analysis of precipitation data from 1916 to 2015 leads to the estimation of historical playa inundation and suggests that an increase has occurred in the frequency of large rainfall events that may be associated with increasing frequency of playa inundation. This study highlights the complex nature of playa inundation in the Jornada Basin, which can change over time in an evolving climate and landscape.

ACKNOWLEDGEMENTS

There are many people I would like to thank as I complete and reflect on my master's degree. First, I want to thank Dr. Enrique Vivoni for the opportunity to work on this research and for his guidance. Thank you to my committee members, Jiwei Li and Kelin Whipple, for their feedback and suggestions. I was very fortunate to have the friendship and support of many colleagues and peers at different points in my journey, including Josh Cederstrom, Zac Keller, Eli Perez, Agustin Robles, Zhaocheng Wang, Kristen Whitney, Luisa Orci, Ruby Hurtado, Jose Becerra, Wren Raming, Akram Hossain, Swastik Ghimire, Mary Ferguson, Haoran Hao, Danna Villarreal, Sara Alonso, and others. I am also grateful for my family and close friends who have always been there for me. I would like to thank the great researchers and staff from the Jornada Basin LTER, especially John Anderson and Curtis Monger. Thank you to Owen McKenna for his research that helped serve as a launching pad for my project and for being available to answer questions. Thank you to Gesuri Ramirez for all his help and technical expertise with the Tromble Weir telemetry network. Finally, this work was supported by funding from the Jornada Basin LTER (NSF Award #2025166) in the form of a graduate research fellowship. Thank you.

TABLE OF CONTENTS

Page

LIST OF TABLES

Table Page

Table Page

LIST OF FIGURES

Figure Page

Figure Page

Figure Page

Figure Page

Figure Page

Figure Page

Figure Page

CHAPTER 1

INTRODUCTION

In the arid southwestern United States, water is a critical resource that determines the few places that can support the survival of plants and humans (Cayan et al., 2010). Understanding the hydrological processes that govern this system is crucial for the sustenance of life and human development. The primary water input in the region is precipitation from localized, high intensity monsoon storms in the summer months and broad, frontal systems in the winter months, with the former being the dominant storm type for runoff generation (Goodrich et al., 1997). Hydrologic connectivity describes the movement of water across a landscape, and surface runoff, especially through river and stream channels, is one of the most important pathways for water transport (Bracken and Croke, 2007). According to the National Hydrography Dataset (NHD), 94% of streams in Arizona and 88% of streams in New Mexico are intermittent or ephemeral, meaning they only flow at certain times of the year when they receive water from snowmelt or directly from precipitation (NHD, 2008; USEPA, 2015). This limited presence of surface water constrains hydrologic connectivity in the region and makes any direct measurements of water, whether in transit or in storage, even more valuable.

A common landscape in the Basin and Range province of the southwestern U.S. consists of parallel mountain ranges and broad valleys. Many of these valleys are internally drained or endorheic basins, meaning they have no surface water outlet (Connell et al., 2005). Due to this internal drainage, hydrologic connectivity in endorheic basins is between mountain or piedmont slopes and the basin floor. Characterizing how

precipitation that falls on upland slopes reaches lower parts of these basins is difficult due to channel transmission losses, evaporation, and water uptake by plants, as well as relatively sparse data in these often-remote landscapes. Studies of small watersheds are important for quantifying hillslope runoff and streamflow in upland regions, areas which transport water and sediment to the basin floor and are one endmember of basin-scale hydrologic connectivity (Osborn and Lane, 1969; Schreiner-McGraw and Vivoni, 2017). On the basin floor, desert playas are topographic low points that experience ephemeral flooding and constitute the other endmember of this connectivity (Shaw and Bryant, 2011). Two types of playas are discharge playas, which are flooded by the discharge of groundwater at the playa surface, and recharge playas, which are flooded by precipitation and surface runon (Rosen, 1994; Shaw and Bryant, 2011). This study will focus on recharge playas, which are characterized by clayey soils and are important grassland communities in an otherwise shrub-dominated landscape (Peters and Gibbens, 2006). The role of recharge playas as termini of their upstream catchments and as areas of focused groundwater recharge (McKenna and Sala, 2018) make them and their inundation dynamics of special interest. The playas examined in this study are instrumented with water level sensors and are located north of Las Cruces, New Mexico, within the U.S. Department of Agriculture's (USDA) Jornada Experimental Range (JER) and New Mexico State University's (NMSU) Chihuahuan Desert Rangeland Research Center (CDRRC).

Research Motivation

A key motivation of this work is to understand and quantify playa inundation dynamics. Playas have long been known to play an important role in the hydrologic cycle of arid systems (Evans and Thames, 1981). In order to understand their role, it is important to discuss how playas are defined and what characteristics make them unique. Given their abundance and variety across the western U.S., many definitions exist for the word "playa". A broad definition classifies a playa as a depositional landform located at the lowest point of a closed or intermontane basin and that is ephemerally flooded and has fine grained soils (Hawley and Parsons, 1980; Shaw and Bryant, 2011). Some definitions specify that playas are barren of vegetation, but this is mainly applicable to discharge playas where the salinity of the soil or frequency of inundation inhibits plant growth (Motts, 1969; Peterson, 1981). The playas at the JER and CDRRC are infrequently flooded with fresh water from surface runon and support perennial grasses and forbs, with shrubs on the periphery, making the broader definition more appropriate (Wondzell et al., 1990).

One of the properties that distinguishes playas from their surrounding landscape is their soil. These soils lack the calcium carbonate horizon that is present in much of the shallow subsurface of the basin, allowing them to function as areas of groundwater recharge (Peters and Gibbens, 2006; McKenna and Sala, 2018). Additionally, playa soils in the JER and CDRRC are very clay-rich compared to the rest of the landscape and have been observed to contain as much as 69% clay (Monger, 2006). Due to their high clay content, some playa soils form vertisols in response to frequent wetting and drying. Wondzell et al. (1990) state that this shrinking and swelling of the soil can create a very

uneven surface with small mounds and depressions known as gilgai microtopography. They also found that smaller floods sometimes only fill the micro-depressions and do not uniformly inundate the playa. Other research has shown that disturbance of soil due to cattle trampling in and around impoundments results in increased runoff production (Magliano et al., 2022), a phenomenon which could also affect playas in western rangelands. Similarly, soil surface sealing caused by rainfall is a process known to decrease infiltration rates and increase runoff (Assouline, 2004) and could affect the hydrologic activity of both playas and their catchments.

The plant life supported by playas also makes them a significant part of the hydrological cycle and local ecosystems. The dominant plant species present in playas in the JER and CDRRC are *Pleuraphis mutica* (tobosa grass) and *Panicum obtusum* (vine mesquite grass) (Peters, 2013). Net primary productivity in playas has been found to have high interannual variability, since times of high production are closely tied with inundation patterns that control the growth of grasses (Huenneke et al., 2002). This makes playas what are known as "islands of hydrologically enhanced biotic productivity," which highlight the high heterogeneity in water and resource distribution across the landscape (Rango et al., 2006). This heterogeneity has also been exacerbated by the proliferation of shrubs replacing grasses, and despite the susceptibility of the piedmont slopes to this encroachment, playas have proven to be much more resistant and successful in remaining grasslands (Rachal et al., 2012). This doesn't mean that their hydrological functioning is unaffected, however, since woody plant encroachment could still alter runoff generation in playa catchments (McAuliffe, 1994).

Early studies of playa inundation were often based on a small number of playas and had limited quantitative or anecdotal inundation data (Motts, 1969; Loring et al, 1987). Motts (1969) produced a quite detailed study of several playas in the western U.S. that focused on their geology and soil properties, only mentioning playa runon in the context of its effect on the playa surfaces. One of the first studies to discuss the process of playa inundation and the relevant hydrologic factors was done by Hauser (1966) on two playas in western Texas. Hauser examined rainfall-runoff relationships in the playa catchments and playa inundation volume on daily and monthly scales but did not go into depth about the types of rainfall events that cause inundation. Studies of playa inundation in the CDRRC begin with Richardson (1971) and Loring et al. (1987). Both investigations focused on College Playa, referred to in the present work as Playa 7, and relied on observations of flooding without much detail. Van Vactor (1989) built upon previous work by gathering the existing observational inundation data and daily precipitation data from nearby rain gauges and examining the rainfall events that resulted in inundation at College Playa. One of his key findings was that runoff contribution from the playa's upstream catchment is not always necessary for inundation, and rainfall over just the playa can be enough to inundate it. Another interesting finding was that floods in July and August almost always occurred on a dry initial condition, and floods in September and October almost always occurred on a wet initial condition. These results have implications for both spatial and temporal variability in playa inundation behavior that can be further explored now that more data is available.

In recent years, playa inundation studies have gotten more complex but still face challenges related to data availability. Some studies rely on remote sensing products to

quantify the frequency of inundation and determine the effects of surrounding land use and other factors (Collins et al., 2014; Russell et al., 2020; Starr and McIntyre, 2020; Solvik et al., 2021). These investigations provide useful insight into playa dynamics at a seasonal or long-term scale and over large areas, but the limited spatiotemporal resolution of data makes it difficult to make conclusions about single events or playas. Nevertheless, researchers have been able to link factors such as higher precipitation and lower cultivated area within catchments to higher frequency of inundation in playas (Collins et al., 2014; Russell et al., 2020). Collins et al. (2014) also found that surrounding land use can greatly affect hydroperiod, which describes the duration of playa inundation. Solvik et al. (2021) were able to create a Long Short Term Memory (LSTM) neural network to predict playa inundation in the western Great Plains. Although their model had a 95.9% accuracy for predicting the probability of inundation, their data was at a monthly scale, and due to the nature of LSTMs, there were no interpretable coefficients to determine the relative importance of different factors on inundation. Not all playa inundation studies have been limited to remote sensing products. Gitz and Brauer (2016) had in-situ playa inundation data, but their work mainly focused on the evaporation and infiltration of the water that inundated the playas rather than the precipitation and other factors that caused the inundations. They did find, however, that rainfall dynamics had a stronger influence on playa inundation occurrence than the effect of nearby land use on runoff processes (Gitz and Brauer, 2016).

Despite extensive research on playas over the last several decades, very few studies have been able to use high frequency, reliable playa water level data to characterize the rainfall characteristics and catchment properties that are conducive to

playa inundation and determine thresholds for inundation. Most of the existing literature that employs high resolution data to examine the flooding of dryland areas is related to the flooding of ephemeral streams and their catchments. Although these catchments do not terminate in playas, the rainfall-runoff relationships and analyses from these studies are very applicable to dryland playa inundation. Serrano-Notivoli et al. (2022) analyzed rainfall-runoff relationships in the catchments of two ephemeral streams in western Spain using Generalized Additive Models (GAMs). Their data was at daily scale and they determined that a 4-day rainfall event ranging from 4 to 20 mm in size was required to generate flow with at least 95% probability. They also showed that the two catchments saw different results in terms of the significance of the event magnitude and hourly maximum rainfall predictors (Serrano-Notivoli et al., 2022). A study on runoff generation in low-order ephemeral streams in the U.S. Virgin Islands used a similar approach to identify thresholds for flow (Ramos and LaFevor, 2018). They employed a logistic regression that considered the Antecedent Precipitation Index (API) and either total rainfall or rainfall intensity and observed different thresholds for runoff depending on whether or not the catchment contained roads. A similar idea could be applied to playas that have diverse catchment properties.

Returning to the southwestern U.S., Kampf et al. (2018) quantified thresholds for runoff generation in ephemeral catchments in southern Arizona and compare these thresholds among their study catchments. Their method of determining thresholds was simple and involved iterating through a range of thresholds to see which one resulted in the optimal proportion of correct predictions to total observations based on single variables such as hourly rainfall intensity (MI_{60}). One of their findings was that

thresholds tended to increase with catchment area, a result which they even corroborated with thresholds determined for ephemeral catchments from other published studies. They also saw distinct behaviors between catchments with drainage areas greater than 1 km^2 vs. less than 1 km^2, with thresholds for larger catchments affected by partial area storm coverage and thresholds for smaller catchments unaffected. This leads them to recommend using a mean MI_{60} threshold over the catchment as opposed to the maximum MI_{60} (Kampf et al., 2018). These methods have the potential to produce similar results for thresholds for playa inundation in the southwestern U.S., especially considering the similar landscape and climate across the region.

The latest work on playa inundation in the JER and CDRRC was done by McKenna and Sala (2018), in which they estimated groundwater recharge rates at 20 playas based on a chloride mass balance approach. To predict the effect of climate change on groundwater recharge in playas, they modeled the inundation response at their 20 study playas to 560 rainfall events that occurred from 1992-2011. This model produced a threshold of 20 mm/day of rainfall for playas to inundate, from which they made the conclusion that if the occurrence of large rainfall events increases due to climate change, playa inundation and therefore playa groundwater recharge will also increase. Another important result of theirs was that playas with larger, steeper, and less sandy catchments experience greater groundwater recharge, which is directly related to more inundation.

The results of McKenna and Sala (2018), as well as the results and methods of the investigations mentioned above, serve as a starting point for this research, which deepens the current understanding of playa inundation dynamics and their spatial and temporal

variation. The important role of playas makes their investigation critical for characterizing the hydrologic conditions of arid basins as well as for the management of dryland ecosystems. This study builds upon previous work on playas and rainfall-runoff relations and takes advantage of novel, high temporal resolution water level data to fill some of the knowledge gaps about playa inundation at the event scale and test the findings of prior models and observations. The contribution of this study is outlined in the following objectives, which are fulfilled through the analysis of data at 18 instrumented playas and their catchments over a more than 6-year period from June 2016 through October 2022:

Objective 1:

The first objective is to characterize and quantify the conditions necessary for playas to inundate. This is achieved through analysis of a variety of datasets, including precipitation and playa water level data to identify thresholds and understand the patterns in the ambient conditions throughout each inundation event.

Objective 2:

The second objective is to understand the spatial controls on playa inundation. This is achieved by performing regressions and comparisons among playas with different characteristics and in different locations within the JER and CDRRC. Inundation thresholds and behaviors of the playas are also placed in the context of these characteristics.

Objective 3:

The third objective is to apply the observations and results of this study to historical precipitation data to estimate the long-term trends in playa inundation, which helps improve the current understanding of how playa inundation patterns have changed over time. Comparison to existing historical observations of playa inundation also helps validate the results.

CHAPTER 2

METHODS

Regional Setting

The Jornada Basin is located in the Chihuahuan Desert of south-central New Mexico, within a portion of the basin and range province associated with the Rio Grande Rift (Figure 1). The Chihuahuan Desert stretches from northern Mexico to southern parts of Texas and New Mexico and is the product of an active and extensive geologic history. The Rio Grande Rift tectonic system is characterized by north-south trending mountain ranges and broad desert basins, and the rift has been active since middle Tertiary time (Seager 1975). The oldest rocks in this region are the Precambrian crystalline basement rocks, which are primarily found at the base of mountain ranges and represent the accretion of the southern part of the North American continent (Seager, 1981; Condie, 1982). Later rock units are mostly sedimentary, with Paleozoic limestone, sandstone, and shale making up a majority of the Doña Ana mountains, which are on the southwestern edge of the basin, as well as the San Andres mountains, which form the eastern edge of the basin (Monger et al., 2006). Important tectonic changes in the region began with the Laramide Orogeny in the early Cenozoic era, leading to extensive uplift, thrust faulting, and folding. The Laramide Orogeny was followed by volcanism and the Rio Grande Rift extension, leading to minor uplift and the beginning of basin formation (Monger et al., 2006). A second phase of extension resulted in even more rift basins to form and is responsible for the basins and faults present today. Faulting has played an important role

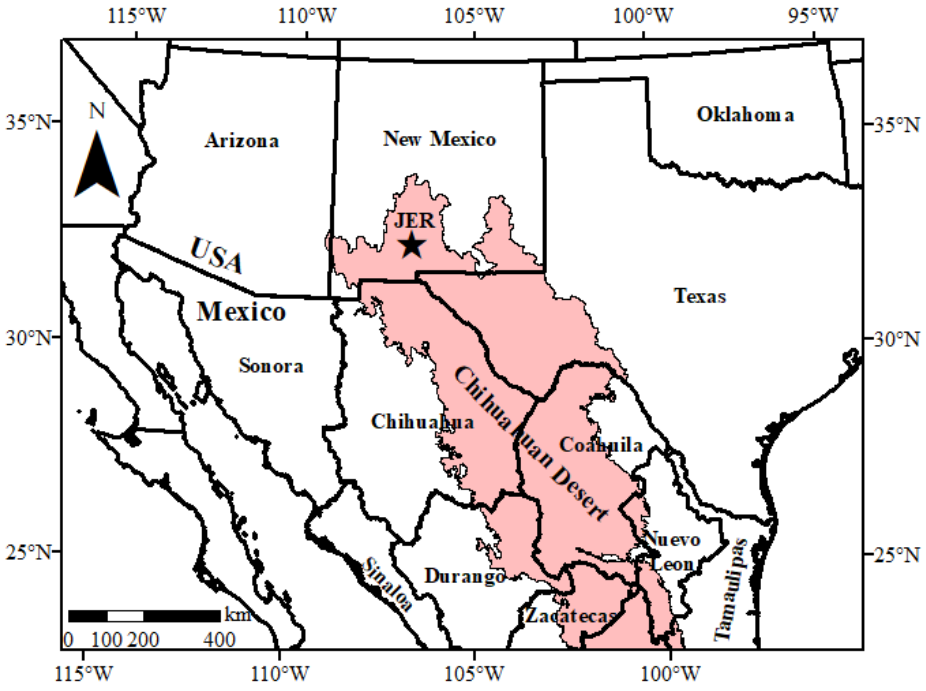

Figure 1. Regional setting of the Jornada Experimental Range (JER) in the northern Chihuahuan Desert in southern New Mexico.

in shaping the Jornada Basin and has even significantly impacted its hydrological development by isolating it from the Rio Grande, which once flowed through the basin, and creating low points where playas have formed (Monger et al., 2006).

The modern Jornada Basin has been filled with sediment shed from the surrounding mountain ranges and is characterized by three main physiographic provinces: mountains, the piedmont slope, and the basin floor (Gile et al., 1981). The piedmont slope, or bajada, consists of coalescing alluvial fans and has a desert pavement with abundant shrubs and bare space. In the shallow subsurface, a cemented calcium carbonate horizon is present, which is commonly known in desert environments as caliche. Caliche forms when calcium carbonate deposited from windblown dust dissolves in water that infiltrates into the shallow subsurface and precipitates out the calcium carbonate upon

drying (Reeves, 1970). Extending from the piedmont slope down to most of the basin floor, this horizon limits deep percolation, although some water does penetrate and is even stored in this layer to be used by plants during drought (Duniway et al., 2007; 2010). The movement of water down the piedmont slope primarily occurs through large channels that drain the mountain slopes as well as smaller watersheds and channel networks that originate on the piedmont itself. Much of this water is lost through channel transmission losses and evapotranspiration (Schreiner-McGraw and Vivoni, 2017), but some water does continue flowing until it reaches playas on the basin floor (McKenna and Sala, 2018). This creates an important hydrological connection between the mountain block, piedmont slope, and basin floor in the form of playas with large upstream contributing areas draining the slopes (Figure 2). This continuum also means that the playas receive abundant fine-grained sediments, such as clays, that are transported downslope in suspension and settle during playa inundation events. Inundated playas are dried through evapotranspiration and deep percolation and often leave the clayey soils in a dry, cracked state (Snyder et al., 2006). Water that percolates through playas is expected to recharge the Jornada del Muerto aquifer, since the absence of a calcium carbonate horizon permits deeper movement (Peters and Gibbens, 2006; McKenna and Sala, 2018). The water table is generally very deep, up to 100 meters below the surface on the piedmont slope but can be as shallow as 20 m below the surface in lower elevation parts of the basin (King and Hawley, 1975; Kambhammettu et al., 2010). This makes the playas in the Jornada Basin significant not only as end members of surficial hydrologic connectivity, but also as a point of hydrological connection with the subsurface.

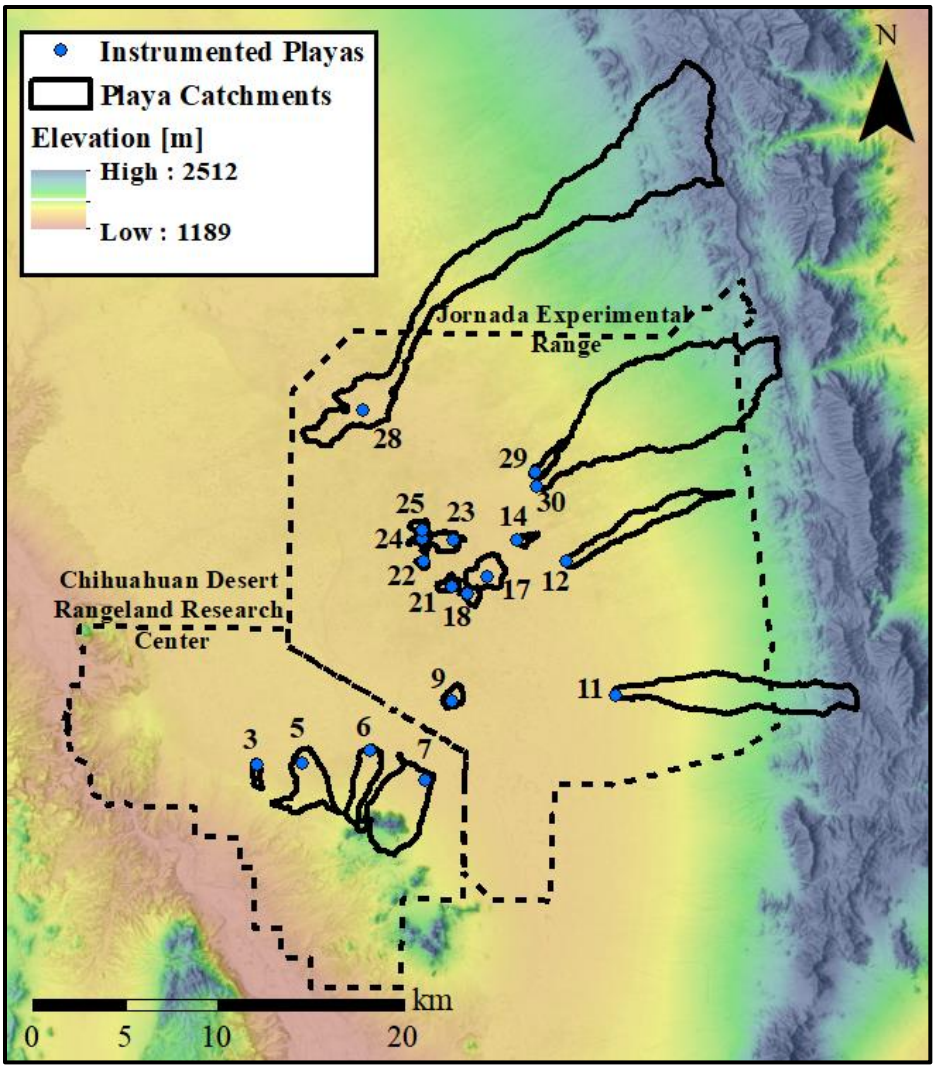

Figure 2. Instrumented playas and their catchment boundaries in the Jornada Experimental Range (JER) and Chihuahuan Desert Rangeland Research Center (CDRRC).

The climate of the basin is considered to be arid to semiarid with high spatial and temporal variability among different elevations and over the long-term century scale period (Wainwright, 2006). The average annual temperature between 1915 and 1993 is 14.70 ± 0.58 °C, with monthly averages of 3.78 °C in January and 26.03 °C in July (Wainwright, 2006). Average annual rainfall between 1939 and 2018 is around 250 mm,

more than half of which occurs from July through October and is associated with the North American Monsoon (NAM) (Peters et al., 2021). The NAM is a phenomenon related to the heating of the land surface causing a reversal in wind patterns that brings moist air from the Gulf of California and the Gulf of Mexico to the southwestern United States and northern Mexico (Adams and Comrie, 1997). Rainfall events during the NAM are typically short, intense, and highly spatially variable. These characteristics lead to increased runoff production during summer months due to high intensity storms exceeding the infiltration capacity of the soil (Michaud et al., 2001). On the other hand, winter precipitation is associated with frontal systems that bring longer but less intense storms, with moisture primarily from the Pacific Ocean. Winter precipitation is also affected by El Niño-Southern Oscillation (ENSO), which brings above average precipitation in El Niño years and below average precipitation in La Niña years (Wainwright, 2006). Overall, this strong seasonality and interannual variability in precipitation plays a significant role in determining the hydrological processes that occur in the Jornada Basin and the availability of water for its ecosystems.

Study Site and History

Researchers at the U.S. Department of Agriculture (USDA) have been working in the Jornada Basin since 1912, which is when the Jornada Experimental Range (JER) was established for rangeland and livestock research. Funding from the National Science Foundation in 1982 led to the establishment of the Jornada Basin Long Term Ecological Research (LTER) program, which is part of a national network of ecological research sites. This led to a collaboration between USDA and New Mexico State University

(NMSU) researchers, which has now expanded to other universities as well, including Arizona State University (ASU). Research at the JER has been motivated by a vegetation shift from grasslands to shrublands that have been linked to overgrazing, fire suppression, and drought and currently seeks to understand these and other natural processes that govern dryland environments.

The JER and Chihuahuan Desert Rangeland Research Center (CDRRC) are situated about 40 km north of Las Cruces, New Mexico, within the southern portion of the Jornada Basin. This area has experienced enhanced desertification and a change in vegetation over the past century that has been well-documented and has been of great interest to ranchers and researchers throughout the region. Grasslands rich in *Bouteloua eriopoda* (black grama) that were once used for grazing have been largely replaced by shrublands dominated by *Larrea tridentata* (creosotebush), *Prosopis glandulosa* (honey mesquite), and *Flourensia cernua* (tarbush). This transition has been driven by factors such as livestock grazing and drought and has had a profound effect on the ecosystems present on the landscape (Peters and Gibbens, 2006).

Woody plant encroachment has exacerbated the heterogeneity of this landscape in terms of both water and nutrients. Features such as mesquite coppice dunes alter the topography in a way that affects the flow of water, and the dunes become strongholds for mesquite shrubs known as “islands of fertility,” which are zones where an altered local distribution of water and nutrient resources promotes further plant growth at that site (Schlesinger et al., 1990). These features also occur on larger scales, such as vegetation patches and even catchments. “Islands of hydrologically enhanced biotic productivity” is a term that describes features like these that form in areas with higher availability of

water than their surroundings (Rango et al., 2006). Ephemeral channels, stock ponds, and playas are examples of these "islands" and are important hydrologic features in a changing landscape and in ecosystems with limited water availability.

Landscape heterogeneity is represented well in the playas and their surrounding catchments that are examined in this study. The 18 study playas are a subset of 30 playas that were originally studied and defined by McKenna and Sala (2016). The catchments of these 18 playas cover about 12.3% of the area of the JER and CDRRC. The features of these playas, generally resulting from the way in which they formed, lead to six natural groupings that facilitate the understanding of their behavior. These groupings are mapped in Figure 3 and photographic examples of each grouping are shown in Figure 4.

One group of playas is associated with a fault that runs through the CDRRC and includes Playas 3, 5, 6, and 7. Playas 3, 5, and 6 are located on the edge of an uplifted alluvial plain, and Playa 7 is located on the edge of the fan piedmont coming off Mt. Summerford (Monger et al., 2006). For simplicity, this group will be referred to as the "Uplifted Plain" playas.

Playas 29 and 30 constitute another group of playas that drains the eastern piedmont slope. These playas formed on the edge of the piedmont slope, possibly related to the change in slope at the basin floor. These will be referred to as the "Piedmont Slope" playas.

Another grouping consists of Playas 12 and 14, which are part of a linear feature in the landscape marked by a high concentration of vegetation that is associated with faulting. These playas essentially form a chain of islands of hydrologically enhanced biotic productivity, so they will be referred to as the "Island Chain" playas.

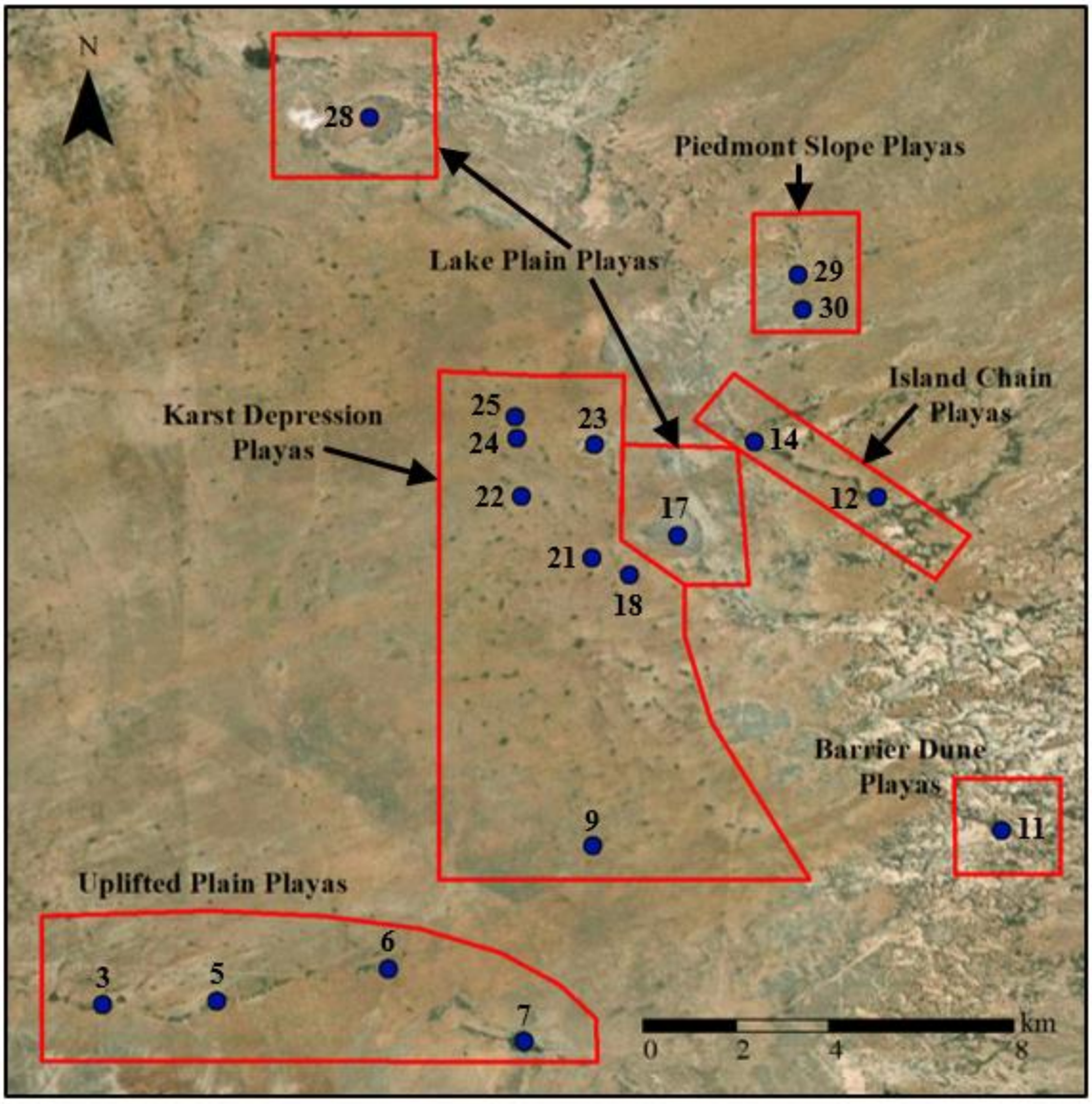

Figure 3. Map of playa groupings in the Jornada Basin based on geological origin.

Playas 9, 18, 21, 22, 23, 24, and 24 form a large group of playas that are in a sandy region dominated by mesquite coppice dunes. These playas formed from subsidence associated with dissolution pipes in the calcium carbonate horizon below them and are thus referred to as the "Karst Depression" playas. It is worth noting that the Karst Depression playas have generally smaller and more circular catchments, while most of the rest of the playas have larger, more elongated catchments. This is related to the

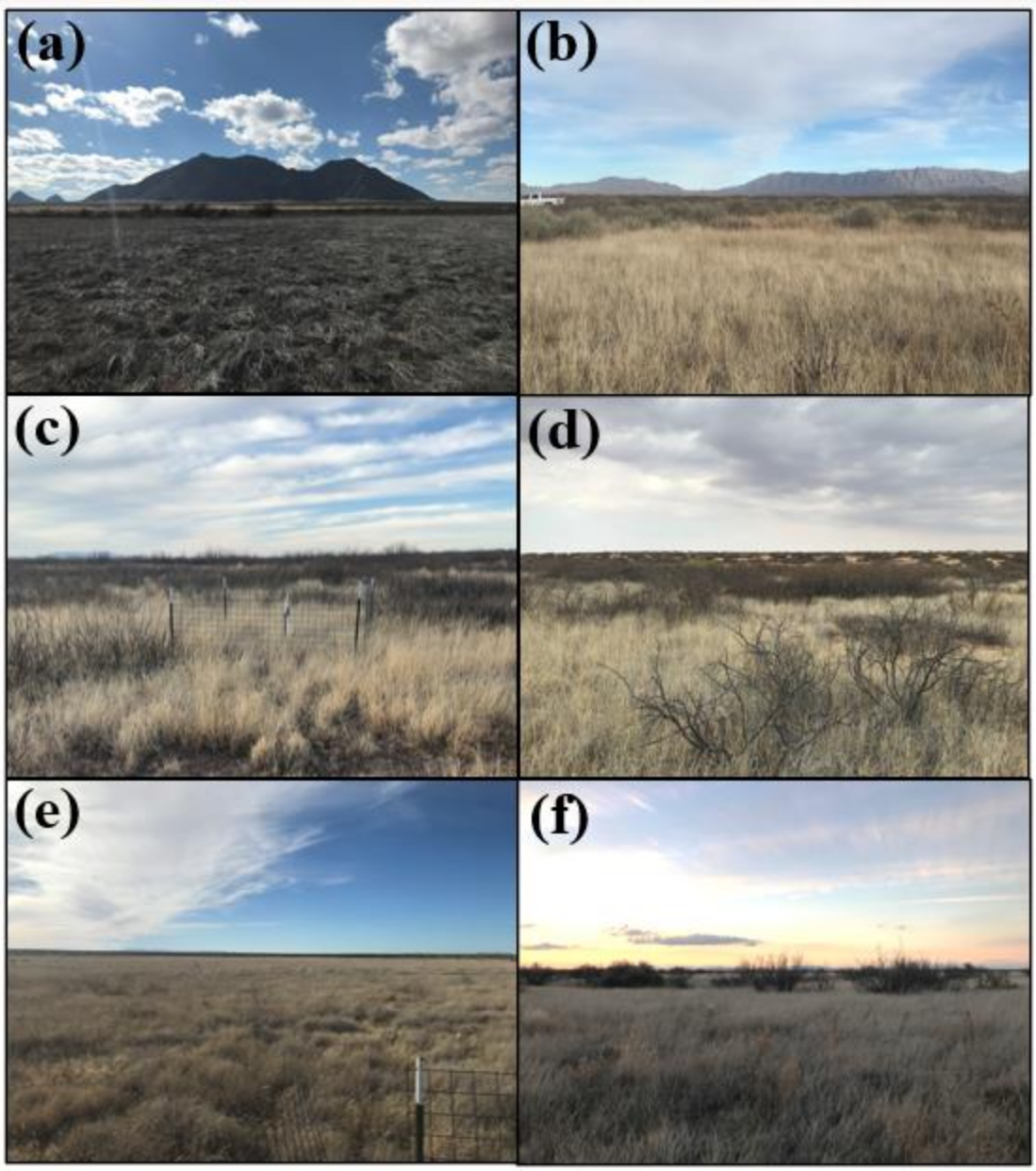

Figure 4. Photographs of four playa groupings. (a) Playa 7 of the Uplifted Plain playas, looking south (upstream) towards Mt. Summerford. (b) Playa 30 of the Piedmont Slope playas, looking east (upstream) towards the San Andres Mountains. (c) Playa 14 of the Island Chain playas. (d) Playa 23 of the Karst Depression playas. (e) Playa 17 of the Lake Plain playas. (f) Playa 11, the Barrier Dune playa.

way the Karst Depression playas formed in local depression on the basin floor isolated from the large piedmont slopes.

Playas 17 and 28 are much larger than other playas in the study area and are actually remnants of pluvial lakes from the last glacial maximum. They have gypsiferous soils and have previously been documented as “Lake Plain” playas (Monger et al., 2006).

Playa 11 is a unique playa in this study and is in a grouping of its own. This playa is located on the eastern piedmont slope, in an area where windblown sand coming eastward up the slope counteracts water-transported sediment coming westward down the slope. On this heterogeneous landscape, what are known as banded vegetation-dune complexes have formed as a result of these interacting processes (Weems and Monger, 2012). These dunes restrict overland flow, thus resulting in increased vegetation growth in those areas (Weems and Monger, 2012). This playa will be referred to as a “Barrier Dune” playa.

These groupings based on geological and geomorphological origins will be referred to throughout the study and are useful to place the behavior of the playas into context to help explain spatial patterns.

Dataset Descriptions

The long history of data collection at JER provides a bounty of information for performing scientific investigations. This work combines established, long-term datasets and recent, novel datasets to make new insights into playa inundation dynamics.

Geospatial Data

The definition and characterization of the study area were achieved through analysis of a bare earth Digital Elevation Model (DEM) obtained from a Light Detection and Ranging (LiDAR) flight over southwestern New Mexico performed in 2020. This product has a 1 m spatial resolution and a 0.2 m vertical accuracy. The DEM was used for delineating playa catchments, determining catchment properties, and understanding playa bathymetry to develop water depth-area-volume rating curves.

Catchment soil characteristics, specifically the sand fraction across the study area, were obtained from the USDA Gridded Soil Survey Geographic (gSSURGO) database at a resolution of 10 m (Soil Survey Staff, 2022). The Landscape Cover Analysis and Reporting Tools (LandCART), an online mapping application created by the Bureau of Land Management, U.S. Geological Survey, and University of California, Los Angeles, was used to obtain data related to vegetation cover, specifically the percentage of bare ground in the study area (Okin et al., 2022). This was obtained as an annual average for 2022 with a spatial resolution of 30 m. These data are shown in Figures 5 and 6 and were analyzed for fractional coverage across playa catchments to determine soil and vegetation metrics for each catchment.

Satellite imagery obtained from Planet Labs (https://www.planet.com/explorer/) provided an important additional perspective of playa inundation and served as a comparison for the inundated area estimates derived from the DEM. These images, which are PlanetScope Ortho Tile products, are acquired by a constellation of CubeSats in a low-Earth orbit and offer surface reflectance data in four spectral bands (Red, Blue, Green, and Near Infrared (NIR)) at a 3m spatial resolution and near-daily temporal

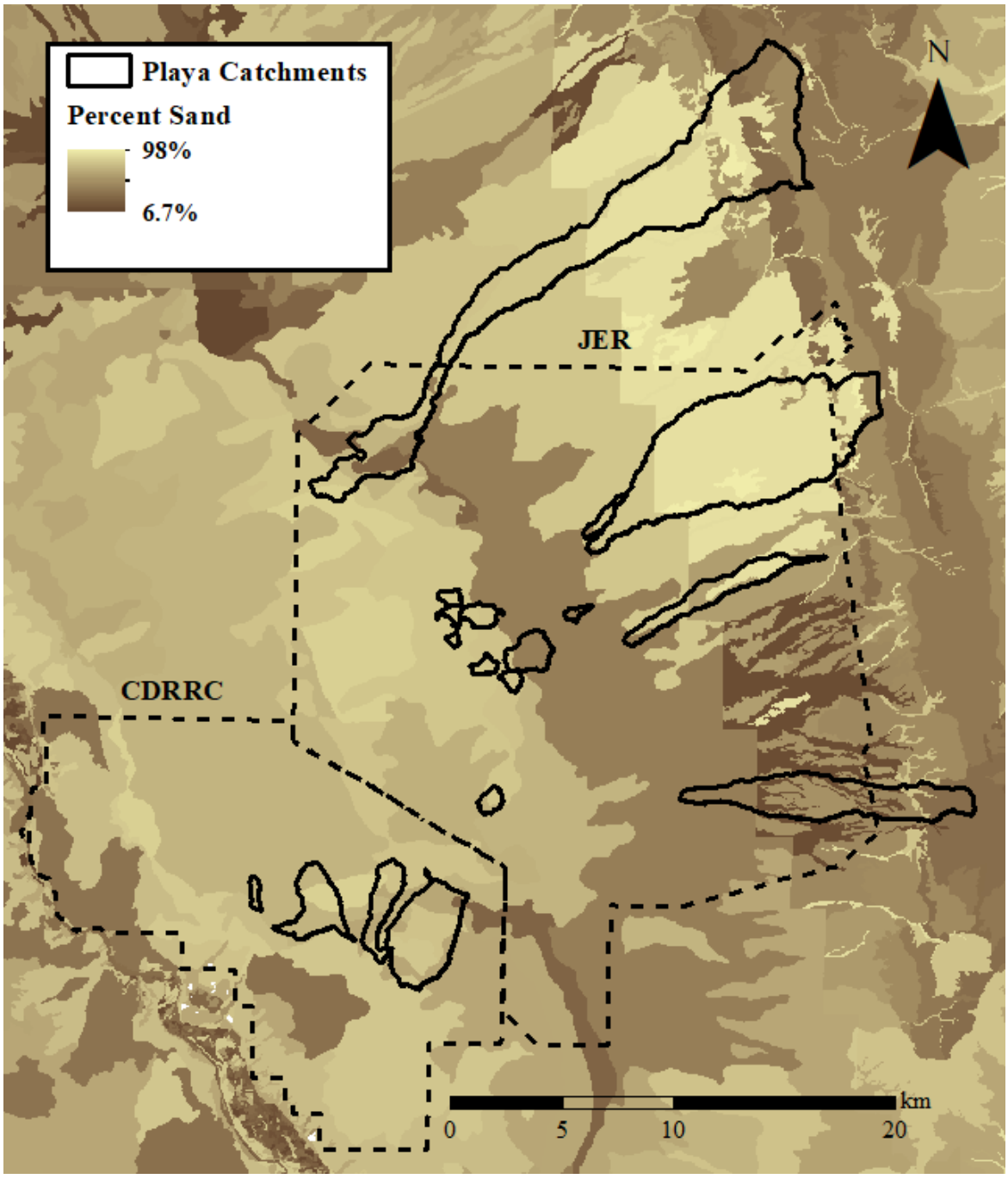

Figure 5. Percent sand over the study site, shown with playa catchment boundaries.

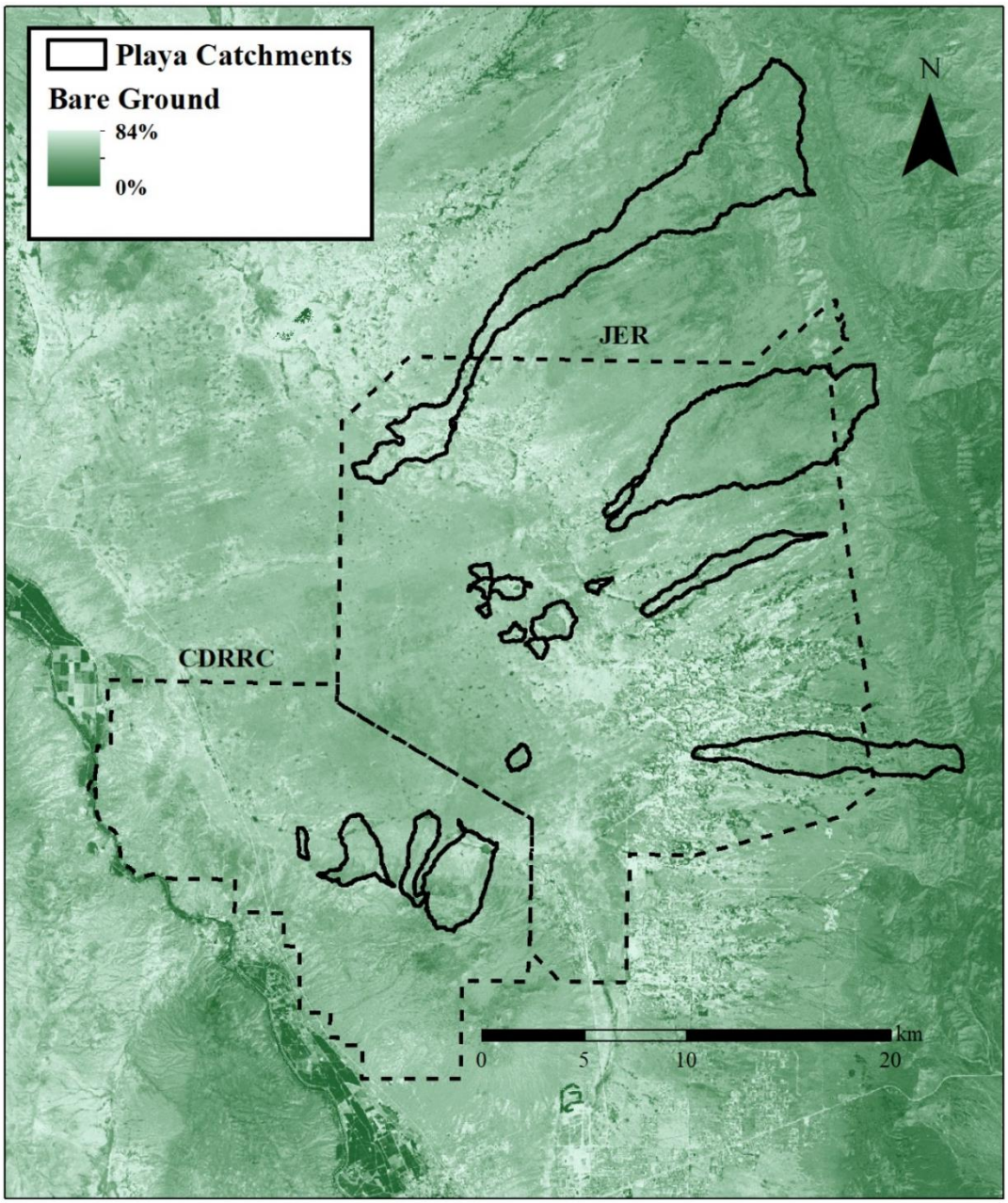

Figure 6. Percentage of bare ground over the study site, shown with playa catchment boundaries.

resolution. They are radiometrically, sensor, and geometrically corrected by Planet Labs and are projected in the UTM projection using the WGS84 datum (Planet Labs, 2023).

Gauge and Radar Precipitation Data

The precipitation data used in this study were obtained from rain gauges and weather radar estimates. The JER and CDRRC have numerous tipping-bucket rain gauges within the sites that are valuable for providing extensive ground precipitation data (details provided in Appendix C). Fifteen of these sites are part of the JER's Net Primary Productivity (NPP) study, 13 are part of the Cross-Scale Interactions Study (CSIS), 35 are part of the JER automated rain gauge network, and 6 are part of the Tromble Weir Watershed, which is managed by ASU (see Anderson 2023a-bb in Appendix C). Although these rain gauges cover a large spatial extent of the Jornada Basin, they are not located in enough of the playa catchments to rely on them for accurate rainfall rates, especially considering the high spatial variability of rainfall in the region. To account for this, this work uses the Multi-Radar Multi-Sensor (MRMS) quantitative precipitation estimation product (https://mtarchive.geol.iastate. edu/). This product is based on radar, gauge, and atmospheric environmental and climatological data and covers the continental U.S. at a 1 km spatial resolution and 2-minute temporal resolution (Zhang et al., 2016). For this study, a 1-hour gauge-corrected product was clipped to the study area. This product fills in the gaps between rain gauges, thus better capturing the spatial variability in precipitation that is so common in the southwestern U.S. (Figure 7). The MRMS gauge correction did not include gauges within the study area, since the data are not all easily available, so a bias correction was performed using the 69 gauges mentioned above.

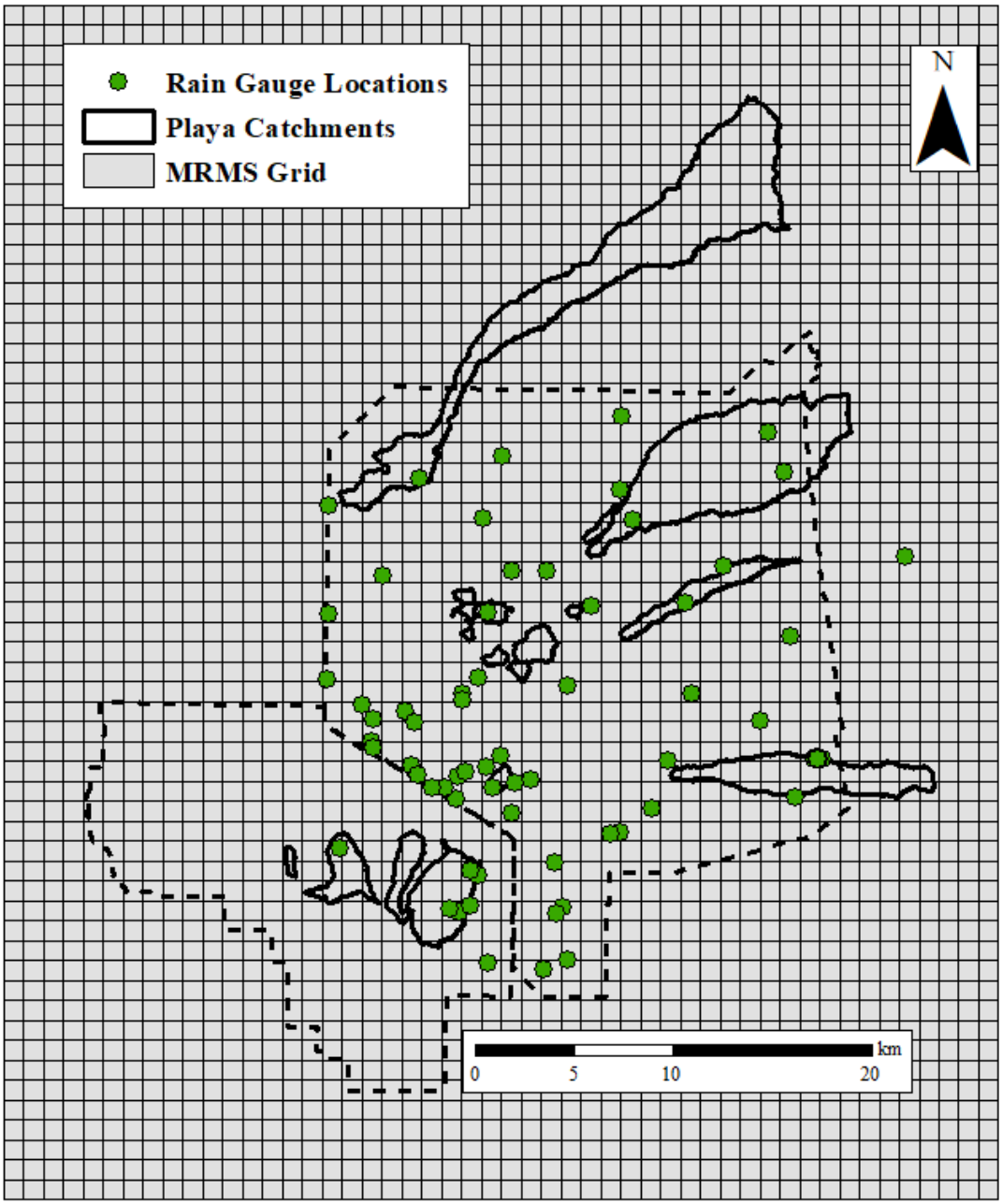

Figure 7. Tipping bucket rain gauge locations in relation to playa catchments and MRMS grid cells.

Playa Water Level Data

To record the hydrologic activity of playas, which is an essential dataset for this work, a network of sensors was deployed in June 2016 at 18 playas within the JER and CDRRC. An Onset U20L-04 HOBO water level sensor designed for depths shallower than 13 ft was installed in a dry stilling well at the lowest point in each playa to measure water depth above the surface. The water level sensor has a typical error of ±0.03 cm and a maximum error of ±0.6 cm. To correct for barometric pressure, an additional water level sensor was placed above-ground at Playa 21 so that it is never underwater. An Onset U23-002 HOBO Pro v2 external temperature/RH sensor was installed on the fringe of each playa to measure air temperature and relative humidity (RH) and fill in gaps in temperature data around the basin to aid vegetation variability studies. The temperature/RH sensor has an error of ±0.1 °C for temperature measurements and an error ranging from ±2.5% to ±5.0% for RH measurements. All instruments record instantaneous measurements every 15 minutes, and data download occurs each year in March, June, and November.

Data Processing

Defining Playa Catchments

Catchment delineation was performed using the Hydrology tools in ArcMap Version 10.7.1 (Appendix D). The first step in this process is to use the "Fill" tool, which is meant to eliminate small sinks that could disrupt the calculated accumulation of flow down the hillslope. However, due to the endorheic nature of playa catchments, the

LiDAR-derived DEM needed to be modified before applying the “Fill” tool. This process involved the creation of “holes” in the DEM, which were designated as ‘No Data’ pixels. The locations of these holes were identified based on playa perimeters surveyed by McKenna and Sala (2016) and depressions visible in the DEM that would result in an inaccurate catchment boundary if filled (Figure 8). The filled raster with holes was then processed using the “Flow Direction”, “Flow Accumulation”, and “Watershed” tools to determine playa catchment boundaries. The “Flow Direction” tool uses a single flow direction algorithm (D8) that directs flow from each grid cell to one of its eight adjacent grid cells (O’Callaghan and Mark, 1984). This is a simple method that has been widely adopted, although some studies have found that it doesn’t always determine the true path of flow (Li et al., 2020). All methods have both advantages and drawbacks, however, and the 1 m resolution of the DEM used for this delineation may help reduce some of the error associated with the D8 method. Based on the flow direction raster, flow accumulation is calculated based on the number of cells that ultimately contribute flow to each given cell, which is higher in stream channels and close to the catchment outlet, or playa. Finally, the watershed is delineated based on the flow direction raster and the cells that contribute flow to the specified pour point, which in this case is the playa. The resulting boundaries were checked against the DEM and satellite imagery to verify any questionable edges, and holes were added or removed as needed to generate the most probable catchment boundaries, which were used for all subsequent analyses.

Catchment characteristics were analyzed in ArcMap using the DEM and other spatial data about the land surface and are summarized in Table 1. From the DEM and catchment delineation process, the playa catchment area (m^2) and average slope (%) were

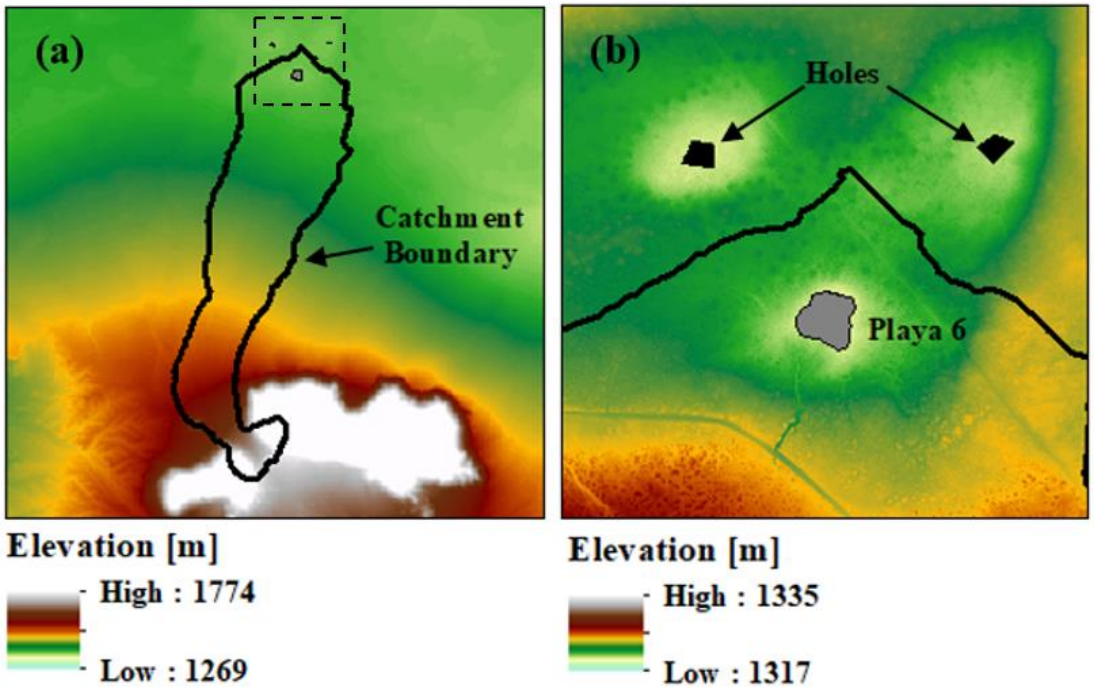

Figure 8. Example of catchment delineation process for Playa 6 showing (a) the resulting catchment and (b) a zoomed-in view of the catchment boundary near the playa and holes in the DEM that were added to avoid filling important local depressions that would otherwise have been included in the Playa 6 catchment.

derived. Sand fraction from gSSURGO and bare ground from LandCART were calculated by taking a spatial average throughout each catchment computed in ArcMap based on the data of interest and the playa catchment boundaries.

Precipitation Corrections and Aggregations

Before use in data analyses, the Multi-Radar Multi-Sensor (MRMS) data were bias-corrected using tipping bucket rain gauge data and a mean field bias correction method at hourly and daily timesteps, meaning a single correction factor was determined and applied to the entire grid for each hour and day. The 69 rain gauges were located in 50 different MRMS pixels, and gauge values within the same pixel were averaged to

Table 1. Playa catchment characteristics obtained from spatial datasets.

Playa No.	Catchment Area (m^2)	Average Slope of Catchment (%)	Average Percent Sand (%)	Bare Ground (%)
3	530,575	4.65	73.80	59.80
5	5,626,063	7.39	76.77	55.37
6	3,936,394	9.69	75.50	55.05
7	11,445,044	18.04	74.61	55.34
9	914,678	4.91	77.20	52.07
11	17,973,711	10.73	45.87	46.08
12	6,526,011	8.54	75.82	55.11
14	429,497	5.82	48.10	58.11
17	2,831,550	4.19	51.94	57.83
18	633,065	8.38	80.00	63.03
21	666,704	9.97	80.78	60.76
22	236,210	11.27	81.20	61.82
23	1,394,212	8.68	78.22	61.66
24	560,528	11.32	81.20	59.50
25	577,972	11.71	81.20	57.95
28	63,872,558	11.12	74.41	49.83
29	1,075,957	11.95	76.08	58.53
30	49,992,399	12.37	88.95	47.94

obtain a single value for the pixel. The correction was performed for each individual hour and day to adequately correct the radar bias, which can vary over time. The correction utilized the linear regression line forced through the origin, with the rain gauge values as the independent variable and radar values as the dependent variable to avoid compounding the radar uncertainty (Yoo et al., 2014). The slope of this regression (β), the inverse of which was used as the correction factor, is:

$$\beta = \sum_{i=1}^{n} x_i y_i \Big/ \sum_{i=1}^{n} x_i^2 , \tag{2.1}$$

where *n* is the total number of positive gauge-radar pairs in a given hour, x_i is the precipitation value from the rain gauge and y_i is the precipitation value from the radar for a given gauge-radar pair.

Data pairs in which the radar value was zero and the gauge value was positive were excluded since they disproportionately increased the denominator in some cases and led to unreasonable corrected rainfall values. The distributions of hourly and daily correction factors ($1/\beta$) obtained through this method are shown in Figure 9. There was a total of 55,920 hours (2,330 days) in the study period of June 15, 2016 to October 31, 2022. There were 94 hours of missing radar data, but the longest stretch of consecutive missing hours was only 11. Since only grids with positive rainfall values were corrected, there were 2,783 hourly correction factors and 585 daily factors. At the hourly scale, 1,108 correction factors were less than one, and 1,655 were greater than one. At the daily scale, the numbers of correction factors less than and greater than one were 272 and 312, respectively. Figure 10 shows a raw and corrected rainfall grid over Playa 7 and its

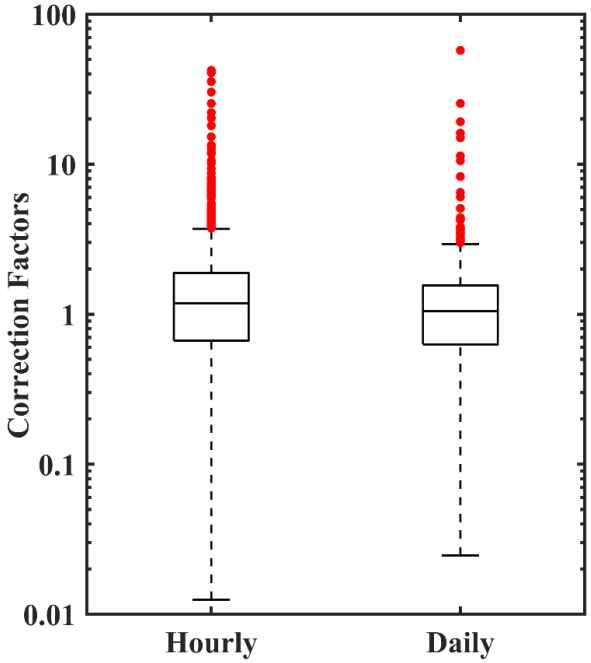

Figure 9. Box and whisker plot of the correction factors obtained through the mean field bias correction at hourly and daily timesteps.

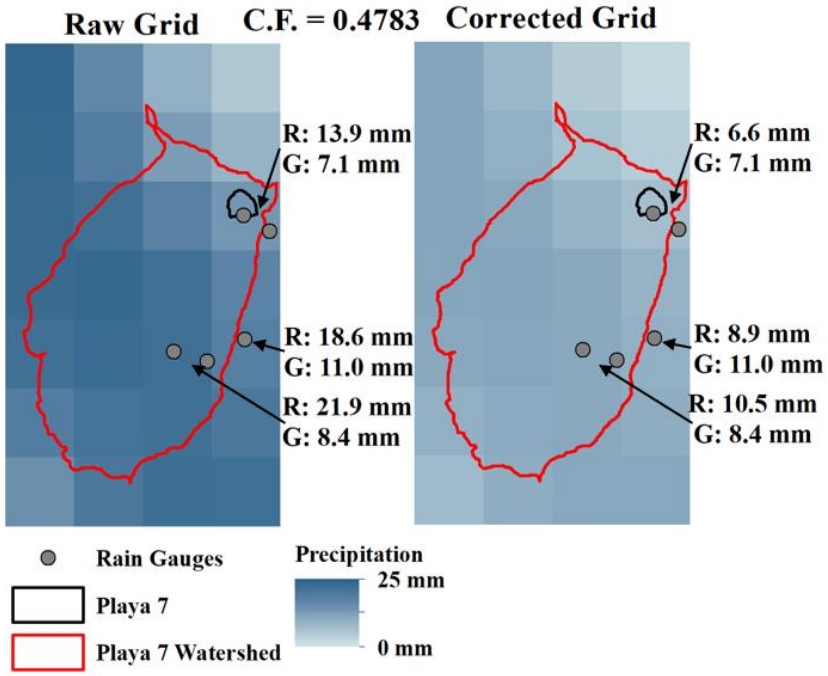

Figure 10. Example of a raw rainfall grid (left) and a corrected grid (right) over the catchment of Playa 7. Radar values (R) are compared to the average gauge values (G) for the three pixels with gauges. This grid is from July 17, 2021 at 16:00. Pixel size is 1 km^2.

catchment for July 17, 2021 at 16:00. The correction factor of 0.4783 brings the radar estimates closer to the rain gauge measurements, although it doesn't make them equal since a single correction factor was determined for the entire 50 km x 50 km grid and the bias may vary spatially to some degree. For the pixels with multiple rain gauges, the average of their measurements is compared to the MRMS value.

The corrected radar grids were then used to calculate hourly and daily rainfall depth, volume, maximum 60-minute intensity (I_{60}), mean I_{60}, and storm distance to the playa for each catchment, examples of which are shown in Figure 11. Spatially averaged hourly rainfall depth was calculated by multiplying the proportion of the area of the catchment within each pixel by the corresponding pixel's value, including zero values, and adding all of these products together. Rainfall volume was calculated by multiplying each grid cell's value by the fraction of its area within the catchment and the area of the pixel (1 km^2), then adding the pixel volumes together to get the volume for the watershed. Maximum intensity was obtained as the maximum pixel value within the catchment in each hour. For the daily scale, maximum intensity was defined as the maximum hourly pixel value within the catchment for that day. Mean I_{60} was calculated as the average of the pixel values within the catchment for each hour, including zero values. For mean I_{60} at the daily scale, the maximum mean I_{60} value for that day was used. Storm distance from the playa was calculated by finding the distance from the weighted centroid of the pixels with rainfall to the center of the playa. This metric allows quantifying the spatial variability across storms and to identify its effect on playa inundation.

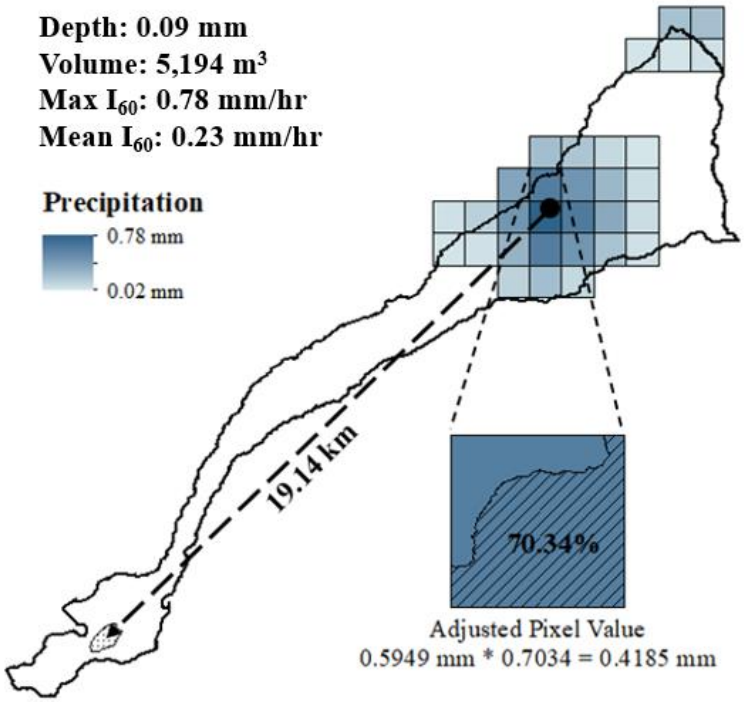

Figure 11. Example of an hourly rainfall grid over the catchment of Playa 28 from which rainfall metrics were calculated.

Water Level Data Quality Assurance and Event Definition

Water level data were processed to remove erroneous values and identify inundation events. A key part of this processing was a comparison to the MRMS catchment-averaged precipitation data to determine whether each recorded inundation event was accompanied by a precipitation event. Spikes in water level readings that were not associated with precipitation were related either to fluctuations when detaching and attaching the datalogger for data download or to periods with extraordinary background noise due to sensor error. Once the valid water level readings were identified and isolated, the data was broken down into individual events, the process of which is described below and illustrated in Figure 12. In most cases, the events could be clearly defined based on a single rise and fall in water level, but in some cases, multiple peaks

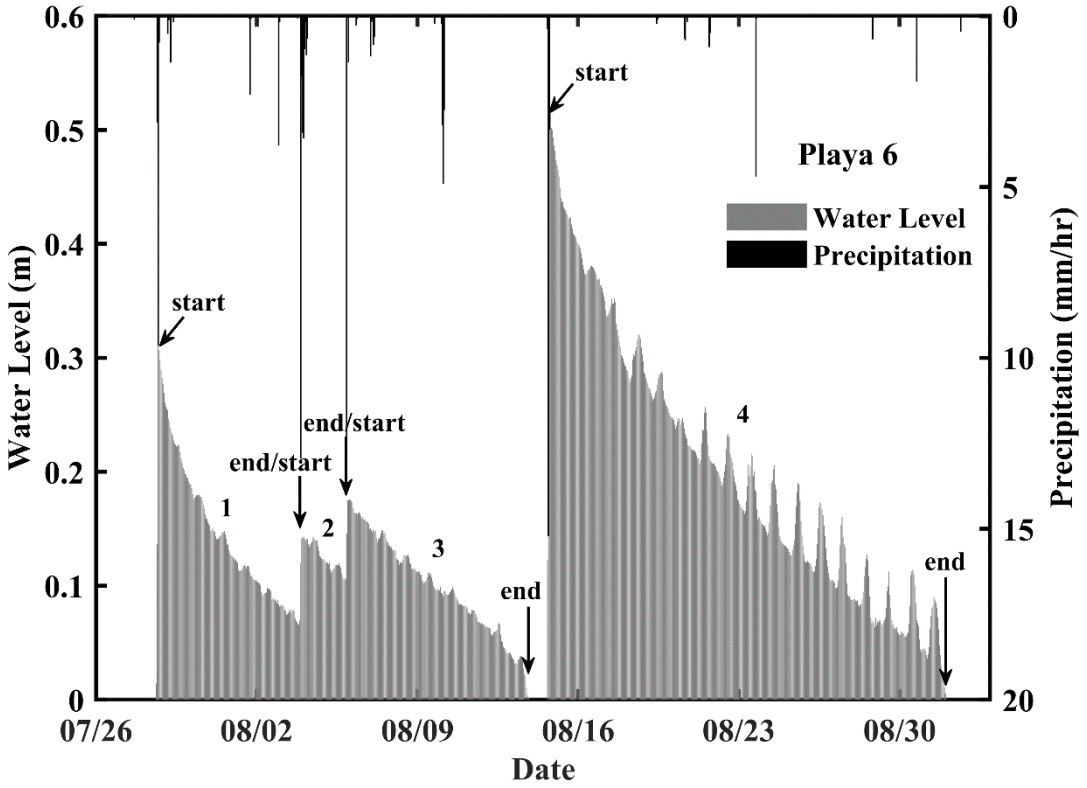

Figure 12. Definition of four inundation events at Playa 6 in the summer of 2019.

were reached before the water level returned to zero. In all cases, the start of an event was defined as an increase in water level of at least 3 cm over the course of one hour accompanied by a rainfall pulse. These criteria distinguished actual inundation responses from background noise and sensor fluctuations. The end of an event was defined as the time at which the water level returned to zero, or if the water level did not return to zero, it was defined by the start time of the next event. If an event started before a previous event reached a water level of zero, this event had to meet the starting criteria mentioned above and begin at least 12 hours after the start of the previous event in order to be considered a new, distinct event. To find the water level associated with this type of event, the initial water level at the start of the event was subtracted from the maximum water level reached in the new event.

Calculation of Water Volume in Playas

For better comparison of inundation data among playas and to precipitation data, the water volume of each inundation event was determined using the bathymetry of each playa determined from the LiDAR-derived DEM. First, the DEM was used in ArcMap to obtain the elevation of each playa's water level sensor and an elevation raster for each playa catchment. The rest of the process was done in MATLAB, where inundated areas and volumes were calculated for water depths at 1 cm increments ranging from 1 to 100 cm, since very few events exceeded a depth of 100 cm. For each depth, the elevation of the water surface was calculated by adding the water depth to the elevation of the water level sensor. It was assumed that all pixels in the playa catchment's elevation raster with an elevation lower than the elevation of the water surface would be inundated. The total inundated area was based on the number of inundated pixels and the total water volume was determined by multiplying each 1 m^2 pixel by its water depth and taking the sum of all these values. This information was used to plot inundated area and volume against the water depth for each playa, which were then normalized for graphical comparison and plotted in Figure 13. The inundated area and water volume values for each water depth at each playa are available in Appendix E. These plots demonstrate the effect of the shape of the playas and surrounding topography. The playas that inundate higher fractions of their area and storage capacity at shallower depths would be expected to have flatter surfaces. Flatter topography would lead to a few centimeters of water depth being spread over a large area as opposed to being concentrated in a small low point. This appears to be the case with the Barrier Dune, Island Chain, and Piedmont Slope playas, which are all less topographically defined than others, such as the Karst Depression playas. Their

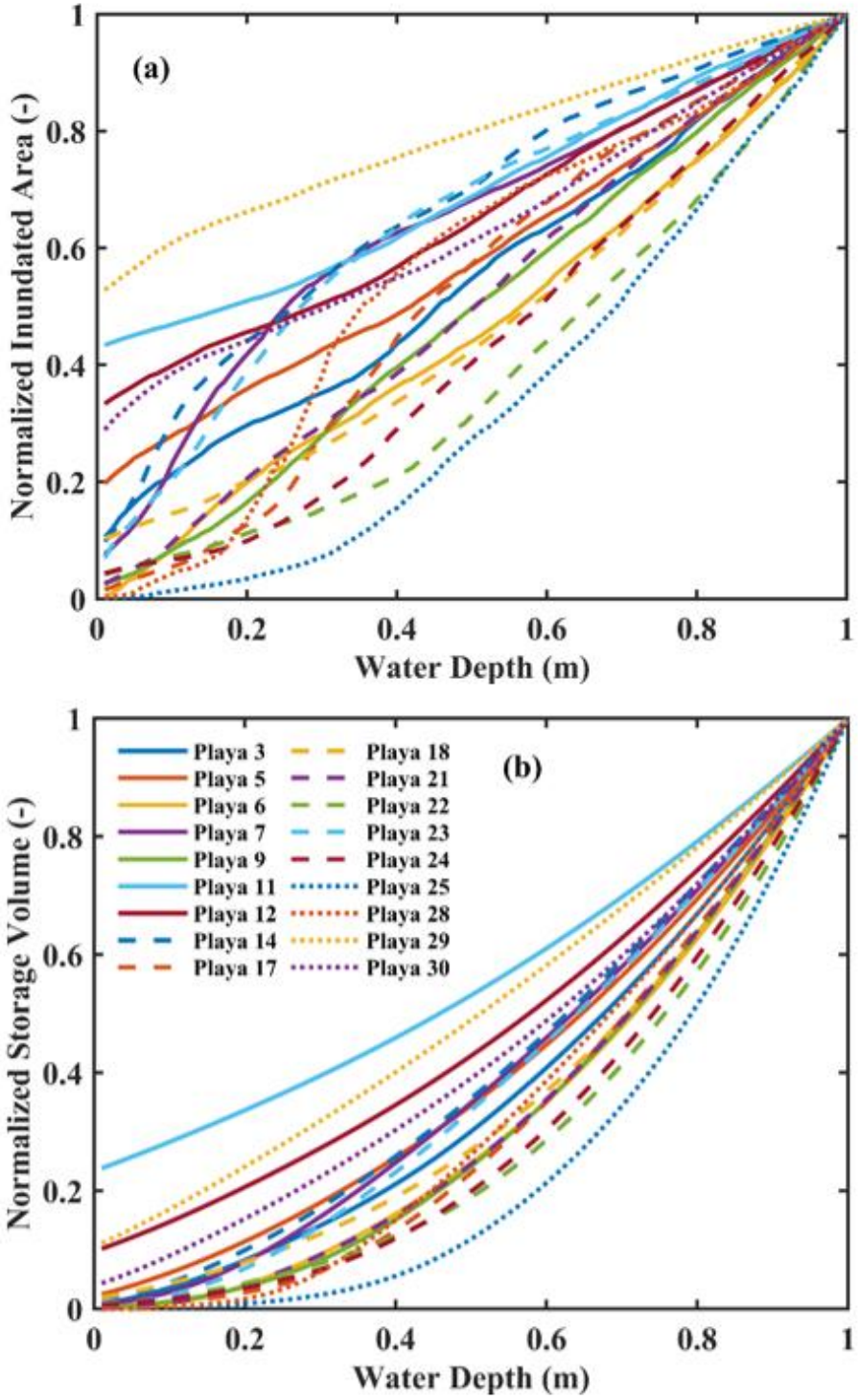

Figure 13. (a) DEM-derived inundated area versus water depth and (b) DEM-derived water volume versus water depth for all 18 playas. Normalization by maximum values was done to facilitate plotting of all values, since there was a large range of areas and storage volumes.

position on or near the eastern piedmont slope makes their surrounding topography more complex and does not allow for the same type of depressions to form as on the basin floor. It is also likely that determining inundated area and volume for these three playa groupings has errors associated with uncertainty in the definition of the playa boundaries, placement of the water level sensor, and the assumption that any point in the playa catchments with an elevation lower than the water surface is inundated.

Analysis of Planet imagery was performed to view inundated area from another perspective. This analysis followed a water-detection method used by Wang and Vivoni (2022) that is based on differences in surface reflectance between wet and dry areas in an image. To make this distinction in vegetated playas, the Normalized Difference Water Index (NDWI) was determined to be the most suitable metric. NDWI is based on the green and NIR spectral bands and is defined as:

$$\mathrm{NDWI} = \frac{\mathrm{G} - \mathrm{NIR}}{\mathrm{G} + \mathrm{NIR}}. \tag{2.2}$$

The method to identify inundated areas consists of calculating the difference in NDWI between an image with playa inundation and a dry image. This results in an image that represents the change in NDWI between those two images, which is expected to be greatest inside the playa. An example of this process is shown for Playa 6 in Figure 14. The playa is clearly visible in the center of Figure 14c as having a higher ΔNDWI. Unfortunately, not all playas have Planet imagery available for times when they were inundated, due to both cloud cover and sometimes very rapid inundations. Also, the value of ΔNDWI that distinguishes the inundated from the dry area is currently subjective and needs to be verified with ground observations. Nonetheless, it is still useful to compare the potential inundated area from Planet imagery and that derived from the DEM.

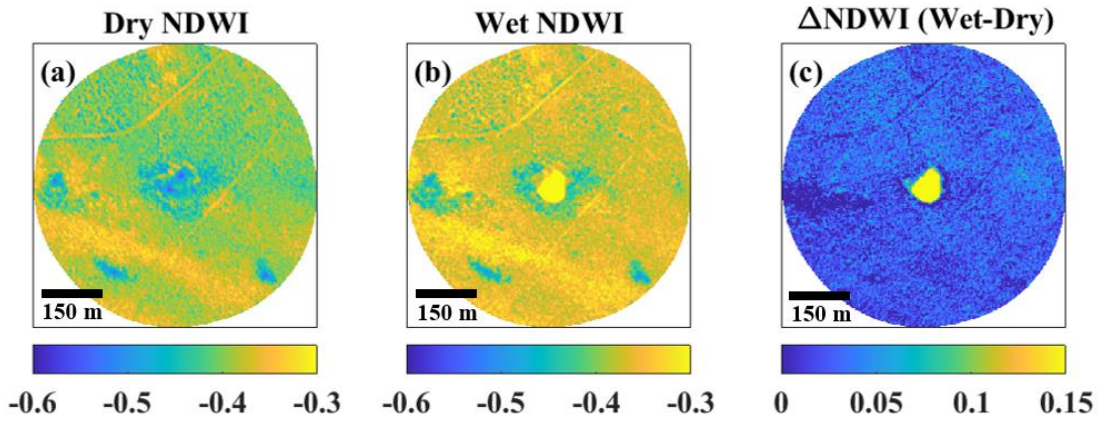

Figure 14. Examples of NDWI at Playa 6 during (a) dry conditions on September 28, 2019 and (b) wet conditions on October 7, 2019 and (c) the difference between wet and dry NDWI.

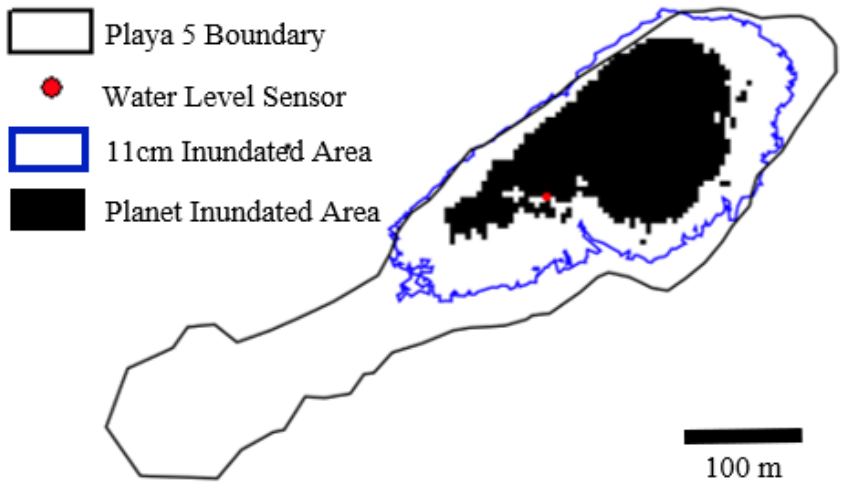

Figure 15. Comparison between the Playa 5 boundary from McKenna and Sala (2016), inundated area derived from the DEM, and inundated area derived from Planet imagery based on a ΔNDWI threshold of 0.05 for a water level of 11 cm on October 5, 2019 at 10:30 AM.

When Planet imagery is available for times of inundation, correlating the image to the corresponding water level and DEM-derived inundated area is a good way to compare the two. Figure 15 shows an example of the inundated area derived from a Planet image for October 5, 2019 at 10:30 AM, when the water level sensor was reading 11 cm, and the expected inundated area based on the DEM for an 11 cm inundation. The difference between the two areas suggests that there could be uncertainty in either or both methods, perhaps related to difficulty viewing shallow water in grassy areas using satellite imagery, but the estimates are still very useful. Planet imagery could be combined with the DEM as well to estimate water level based on the playa bathymetry and the Planet-derived inundated area to compare to in situ water level measurements.

Data Analyses

The heart of the results comes from the analysis of the data described above, with the playa water level data being the key dataset. The analyses were selected to achieve the three main objectives of the study and fall into three general categories. The first analyses performed were related to the drivers of playa inundation, focused on playa behavior and thresholds for inundation. Subsequent analyses were aimed at characterizing the spatial controls on playa inundation and included logistic and linear regressions that synthesized among the playas. Finally, analysis of the trends and characteristics of the historical precipitation data and playa inundation observations was performed to understand playa inundation through time.

Playa Behaviors and Drivers of Inundation

Preliminary analysis of playa water level data was performed by calculating basic statistics, such as the number of inundation events, the mean and standard deviation of the maximum water depths, and the mean and standard deviation of inundation durations for all inundation events at each playa. Seasonality of inundation was examined in terms of the warm season (April through September) and the cool season (October through March), as well as monthly. Some analyses were also performed based on the monsoon season (July through September). Rainfall characteristics from bias-corrected radar precipitation data for the playa catchments were also averaged seasonally. The percentage of days with inundation was calculated for each month at individual playas and averaged over the approximately 6-year study period to understand seasonal trends in inundation.

Runoff ratios were calculated for each playa based on the inundation volumes determined from water depth to volume relationships and rainfall volumes for the catchments based on the bias-corrected MRMS data. Total inundation volume based on the peak water depths of inundation events in a given year or monsoon season were divided by the total volume of precipitation for each year or monsoon season, and the ratios were averaged across years. The mean annual ratios only include the years 2017-2021 since data is not available for the whole calendar years of 2016 and 2022. The mean monsoon season runoff ratio included only the months of July, August, and September for the years 2016-2022.

Threshold determination was performed individually for the variables of precipitation depth (P) or maximum hourly intensity (I_{60}) at each playa to identify precipitation events that cause inundation. Precipitation events were defined using a

minimum interevent time of 6 hours, and the precipitation events with start times most recently before the start of inundation events were associated with those inundations. Thresholds from 0 to 100 mm or mm/hr were iterated through at increments of 0.1, and several metrics were calculated for each threshold to identify the one that produced the best agreement between the predicted and actual outcomes. This is quantified by the kappa agreement statistic, κ, which is computed as:

$$\kappa = \frac{p_o - p_e}{1 - p_e}, \tag{2.3}$$

where p_o is the observed agreement, or the number of responses correctly predicted by the threshold divided by the total number of precipitation events. The expected agreement due to chance alone is represented by p_e, which is calculated as:

$$p_e = \left[p_{obs}(inun.) \times p_{pred.}(inun.)\right] + \left[p_{obs}(no\ inun.) \times p_{pred.}(no\ inun)\right], \tag{2.4}$$

where p_{obs} is the fraction of actual observations of either inundation or no inundation and $p_{pred.}$ is the fraction of predictions of inundation or no inundation based on the threshold. The value of κ can range from 0 to 1, with 1 representing perfect agreement (Viera and Garrett, 2005). The fraction of correct predictions, or p_o, was also recorded for each threshold. Kampf et al. (2018) optimized p_o for threshold selection, but for this work there are too many precipitation events and not enough playa inundations for this to select an adequate threshold. In some cases, the highest p_o is where all precipitation is predicted to not cause inundation, which is why was κ optimized for threshold selection. The percentage of events that were predicted to cause inundation but did not actually cause inundation was considered the percentage of false positives (FP), and the percentage of events that were predicted to not cause inundation but actually did was considered the percentage of false negatives (FN). All of these metrics are useful to assess the

applicability of determined thresholds. The thresholds could then be used to characterize the types of precipitation events commonly associated with playa inundation, as well as the outliers.

Spatial Controls on Inundation

Preliminary spatial analysis of playa behaviors was done based on large scale groupings developed above as well as local features that affect certain playas. These helped put the playa behaviors into context and explain some of the general variation.

The relative importance of catchment factors on the occurrence of playa inundation was evaluated using a multiple logistic regression. All of the logistic regression analysis was performed in the statistical software JMP Pro version 16.0.0, and all independent variables were log-transformed and standardized to account for skewness and the different scales among them. The parameters for the logistic regression are estimated by maximizing the likelihood function, which is as follows:

$$L(b) = \sum_{i=1}^{n} \{y_i(b_0 + b_1x_1 + \ldots + b_kx_k) - ln[1 + exp(b_0 + b_1x_1 + \ldots + b_kx_k)]\}, \quad (2.5)$$

where *y* represents the binary dependent variable, *x* represents the independent variables, *k* is the number of independent variables, *b* represents the coefficients, and *n* is the sample size. The dependent variable in this regression was the binary inundation response (1 = inundation, 0 = no inundation) to all precipitation events greater than 1 mm across all playas. Other studies of runoff generation in ephemeral systems have also favored binary response variables since the number of flow events is so low (Kampf et al., 2018; Serrano-Notivoli et al., 2022). The independent variables included in the regression

analysis were P (mm), I_{60} (mm/hr), catchment area (A, in km^2), average slope (S, in %), average sand fraction (SF, in %), and the average proportion of bare ground (BG, in %). Bare ground was used as a proxy for vegetation cover in the catchments. These catchment properties were determined to capture most of the variability among playas, and they have been examined and deemed important by other studies (Kampf et al., 2018; McKenna and Sala, 2018). The precipitation variables, P and I_{60}, were tested individually and also separately with the catchment variables to determine the effect of the catchment variables in improving the regression and compare the performance of the regressions using P to those using I_{60}. This resulted in the testing of 4 regressions in total: One with just P; one with P, A, S, SF, and BG; one with just I_{60}; and one with I_{60}, A, S, SF, and BG. The regressions with multiple variables were analyzed using a stepwise regression and forward selection to determine the combination of variables that resulted in the best fitting model based on the lowest corrected Akaike's Information Criterion (AICc) (Akaike, 1974). The data was randomly split into training (60%), validation (20%), and test (20%) categories to asses the performance of the regression model. The statistics p_o, κ, FP, and FN were calculated based on the results of the model on the test data once the optimal variables were chosen. The same procedure was repeated only for rainfall during the monsoon season (July, August, and September) to help understand the effect of seasonality.

Mulitlinear regressions were also performed using inundation volume as the dependent variable, as opposed to binary inundation data, to provide insight into the factors that influence inundation magnitude. These were also done in JMP Pro version

16.0.0, and all the variables were log transformed and standardized. The general equation for the multilinear regression is:

$$\hat{y} = b_0 + b_1 x_1 + b_2 x_2 + \ldots + b_k x_k \,, \tag{2.6}$$

where *y* represents the dependent variable, *x* represents the independent variables, *k* is the number of independent variables, and *b* represents the coefficients. The method of least squares was used to calculate the coefficients. The same stepwise regression method used above was applied to select the variables that resulted in the lowest AICc, so 2 regressions were tested in total: One with P, A, S, SF, and BG; and one with I_{60}, A, S, SF, and BG. The parameter values, and standard errors, as well as the model R^2, AICc, and Root Mean Square Error (RMSE) were obtained for each model.

Historical Application

Historical daily precipitation data from the JER Headquarters rain gauge (NOAA, 2023) was used to identify trends in precipitation and playa inundation over the period of 1916 to 2015, which represent the 100 calendar years prior to the beginning of the June 2016 to October 2022 study period. Inundation volumes were calculated based on linear relationships established between daily rainfall depth and inundation volume at each playa. Each playa's daily precipitation threshold for inundation was applied to the rainfall record, and the exceedances were assumed to have caused inundation. The mean annual inundation volume was calculated based on these estimates and compared to the mean annual inundation volumes for the current period.

To identify long-term trends in precipitation, the Mann-Kendall trend test was used. The Mann-Kendall trend test can be used to see if there is a significant trend in a

timeseries. It is based on the differences between each value and its preceding values, which is captured in the test statistic S, shown in Equation 2.6. In this equation, x_j represents a value in the dataset while x_k represents the value before it. The sign of this difference is calculated and summed to determine whether there is a general increasing or decreasing trend in the data.

$$S = \sum_{k=1}^{n-1} \sum_{j=k+1}^{n} sgn(x_j - x_k) \,. \tag{2.6}$$

In order to come to a conclusion, a comparison must be made to the null distribution, which represents the null hypothesis that there is no trend in the data. The null distribution of S is a Gaussian distribution with a mean of zero and a variance represented by Equation 2.7, which shows the case of a sample size (n) greater than ten and the presence of repeated values. In this equation, J represents the number of groups of tied values and t_j is the number of values in a given tied group.

$$Var(S) = \frac{n(n-1)(2n+5) \; - \sum_{j=1}^{J} t_j(t_j-1)(2t_j+5)}{18} . \tag{2.7}$$

Based on the S value and the variance of S, the z-value can be calculated using Equation 2.8, which is the equation used when S is greater than zero.

$$\mathrm{z} = \frac{S-1}{[Var(S)]^{1/2}} \,. \tag{2.8}$$

These values can be compared to the standard Gaussian distribution as a two-sided test to evaluate the significance of the trends. For a significance level of 0.1, the z-value should be outside the range of -1.64 and 1.64, and for 0.05, this range is from -1.96 to 1.96.

Basic comparisons were also made to historical observations of playa inundation over the period of 1970-1989 at Playa 7 compiled by Van Vactor (1989). Playa 7 rainfall

threshold exceedances were calculated for this period using the threshold determined for the 2016-2022 period. Current responses to rainfall were compared to historical ones, and a linear relationship was obtained relating precipitation depth to inundation volume encompassing the data from both periods.

CHAPTER 3

RESULTS AND DISCUSSION

Playa Behaviors

Across the 18 instrumented playas, a variety of behaviors were observed regarding inundation frequency, magnitude, and duration. The most common events were shallow, rapid inundations, but some playas experienced deeper, longer inundation events. Table 2 presents information about the event counts, maximum inundation depths (H), and inundation durations (T) observed at each playa. Playa 14 had the most individual inundation events, with 59, while Playa 3 only had 4. Playa 6 had the longest and deepest inundations, with an average duration of 213 hours and an average depth of 0.32 m. Playa 18 had the shortest inundation events, with an average of only 5 hours. The playa with the shallowest inundation events was Playa 17, with an average depth of 0.04 m. These metrics reveal four main types of playa responses: (A) long (≥100 hr), deep (≥0.10 m) events, (B) rapid (<100 hr), shallow (<0.10 m), relatively frequent events, (C) rapid, deep events, and (D) rapid, shallow, relatively infrequent events. Figure 16 shows water level timeseries at four playas over the study period that are representative of the different types of behaviors. When determining the behavior types of these playas, inundation duration and frequency took precedence over depth due to some key outliers in those two statistics. Frequency was determined to be high if there were more than 50 events in the study period, which is an average of about 8 per year.

It is useful to take a closer look at typical playa responses to rainfall events to develop an understanding of playa inundation dynamics. One of the signature

Table 2. Inundation characteristics of the 18 instrumented playas during the study period June 15, 2016 through October 31, 2022.

Playa No.	Number of Events	Mean H [m]	STD H [m]	Mean T [hr]	STD T [hr]	Response Type
3	4	0.11	± 0.08	18	± 10	C
5	12	0.18	± 0.23	24	± 37	C
6	34	0.32	± 0.29	213	± 146	A
7	9	0.14	± 0.15	103	± 112	A
9	22	0.14	± 0.12	12	± 12	C
11	19	0.10	± 0.04	25	± 37	C
12	58	0.12	± 0.06	12	± 6	B
14	59	0.09	± 0.06	16	± 24	B
17	24	0.04	± 0.03	9	± 10	D
18	16	0.14	± 0.10	5	± 4	C
21	12	0.14	± 0.09	12	± 9	C
22	31	0.26	± 0.17	16	± 17	C
23	13	0.07	± 0.06	17	± 17	D
24	22	0.21	± 0.16	21	± 23	C
25	29	0.25	± 0.18	19	± 21	C
28	9	0.09	± 0.08	72	± 119	A
29	28	0.09	± 0.05	19	± 15	D
30	20	0.09	± 0.05	10	± 8	D

characteristics of playa inundation hydrographs among the instrumented playas is a rapid rise to the peak water level relative to the recession of water level. The average lag times to peak water level ranged among the playas from 0.56 hr to 7.67 hr, with an overall average of 2.18 hours across all instrumented playas. The playas with longer lag times tended to have bigger catchment areas or longer lasting inundation events on average,

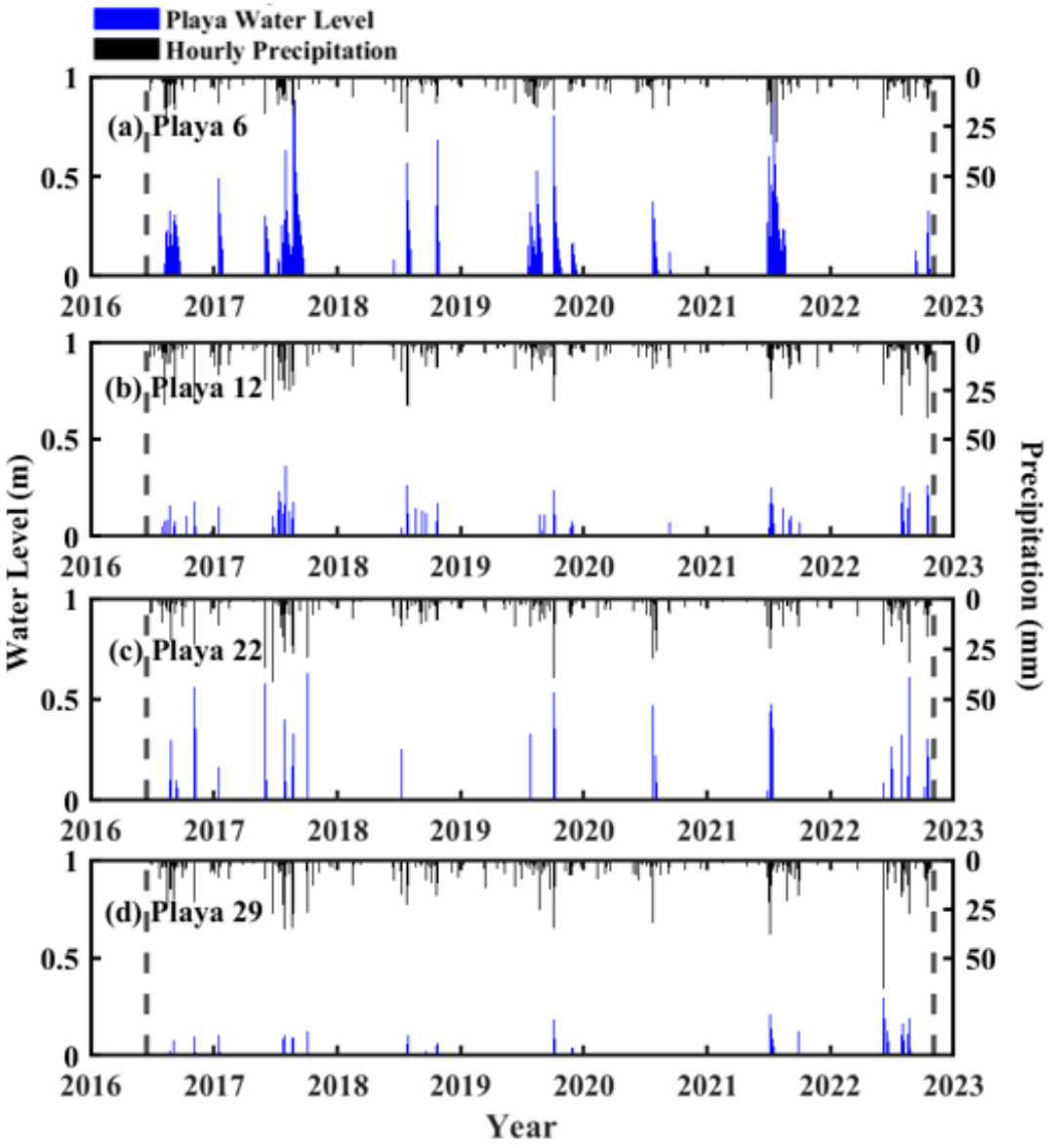

Figure 16. Playa water level plotted over the study period (bounded by dashed lines) for (a) Playa 6, representing long, deep events; (b) Playa 12, representing rapid, shallow, frequent events; (c) Playa 22, representing rapid, deep events; and (d) Playa 29, representing rapid, shallow, infrequent events.

meaning the distance water has to travel to reach the playa and the infiltration capacity of the playa soil likely affect the lag times. Examples of individual events at Playas 6 and 22 are shown in Figure 17 with their respective precipitation data. It is evident that Playa 6, which has a larger catchment area and likely more clay-rich soil, experiences a slightly

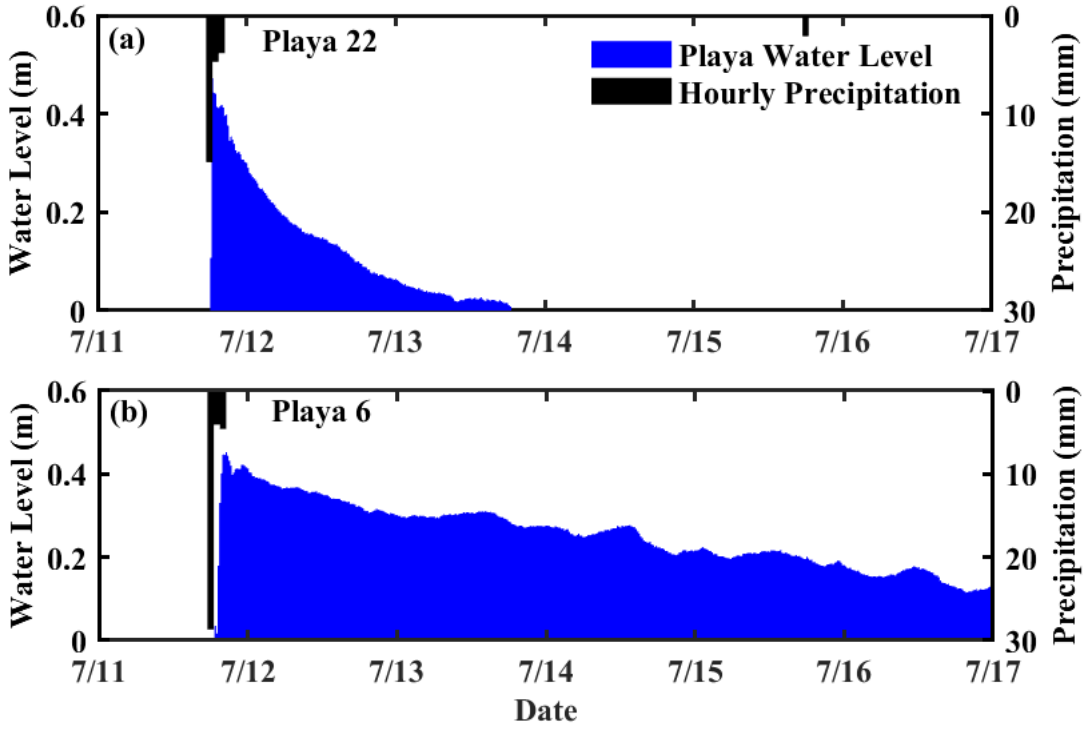

Figure 17. Inundation responses to precipitation during July of 2021 at (a) Playa 22 and (b) Playa 6, showing the rapid rise and more gradual recession in water level.

longer lag time and a much longer-lasting inundation, while the whole process at Playa 22 is more rapid. These examples highlight that although playas respond differently to rainfall, they reach their maximum water levels rapidly in comparison to the several hours, days, or even weeks it could take them to dry up again as the water infiltrates and evaporates.

Seasonality of Rainfall and Inundation

The playa water level time series display a distinct seasonal signal, with most inundation events occurring during the summer months. This pattern in playa inundation follows the seasonal precipitation trends. Over the study period, 66.95% of the total precipitation in the playa catchments fell during the warm season (April-September),

while 33.05% fell during the cool season (October-March). The seasonal trends are seen more clearly in Figure 18, which shows the percentage of days with inundation in each month averaged over the study period at the four playas that represent the different types of behaviors.

Across all 18 playas, there were 318 inundation events during the warm season and 103 cool season events throughout the study period. The precipitation events that caused these inundations were different between the two seasons as well. The warm season inundation-causing precipitation events had an average depth of 30.6 mm, an average I_{60} of 23.6 mm/hr, and an average duration of 7.4 hours, based on the bias-corrected radar precipitation for the playa catchments. The cool season inundation-causing precipitation events had an average depth of 54.4 mm, an average I_{60} of 21.3 mm/hr, and an average duration of 13.8 hours. These precipitation characteristics reflect the generally shorter, high intensity storms that occur in the warm season and the longer, less intense storms in the cool season (Wainwright, 2006). The average intensity of inundation-causing precipitation events in the winter, however, is relatively high and exceeds intensity thresholds for hillslope runoff observed by Keller (2021). This is partially related to differences in scale between the hillslope and the playa catchments, which will be discussed later in more detail, but it suggests that even in the cool season, the dominant mechanism for runoff generation and playa inundation is infiltration excess. This could be due to the North American monsoon from July to September reducing hillslope infiltration rates, which in turn could allow infiltration excess runoff to occur in the winter even though rainfall intensity is generally lower (Etheredge et al., 2004).

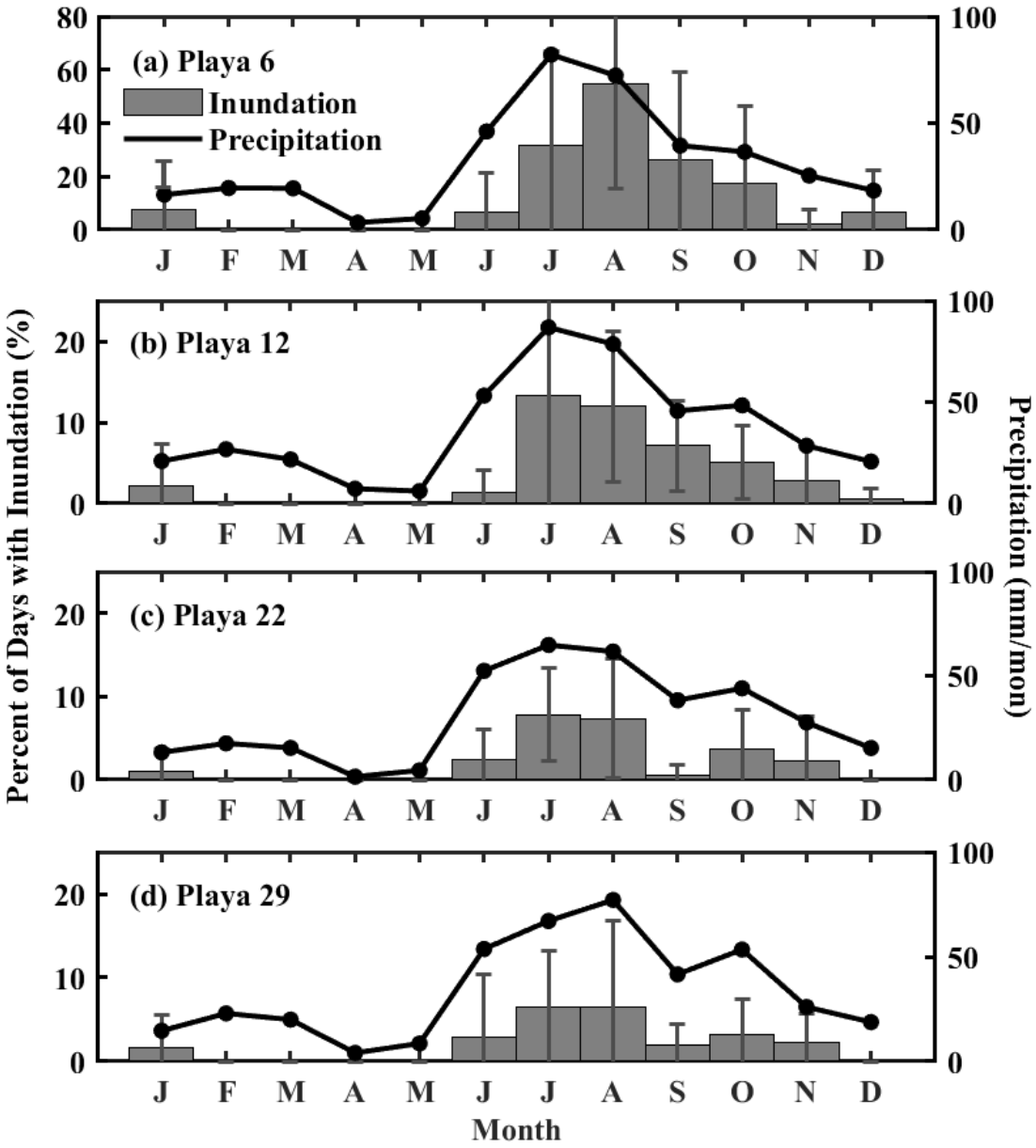

Figure 18. Seasonal trends based on the calendar year in monthly mean precipitation and inundation frequency shown as the average percentage of days in a month with inundation at (a) Playa 6, (b) Playa 12, (c) Playa 22, and (d) Playa 29. Error bars extend one standard deviation above and below the average percentages. Note the different scale on the y-axis in subplot (a).

Drivers of Inundation

Clearly, the key factor leading to playa inundation is precipitation. There were no inundation events at any playas that did not have a corresponding rainfall event associated with them, which is consistent with these being recharge playas. Across all the playas and their catchments, only about 8% of rainfall events resulted in playa inundation, meaning that substantial ponding of water in the playa and generation of lasting runoff in the catchment are not common occurrences. Another way to look at this is through runoff ratios, which can be calculated for each playa catchment using the available water level and precipitation data. Mean annual runoff ratios were calculated for the period of 2017-2021 by dividing the total volume of inundation by the total volume of rainfall in the playa catchment each year and averaging across years. Similarly, mean runoff ratios for just the monsoon season (July, August, and September) for 2016-2022 were also calculated. The resulting values are reported in Table 3, with the mean annual ratios ranging from 0.01% to 9.28% and the mean monsoon ratios ranging from 0.01% to 12.15%. Documentation of runoff ratios in this region is sparse, but the Tromble Weir experimental watershed, located on the eastern bajada of the Jornada Basin, shows a ratio of about 3.16% when mean annual discharge at the watershed outlet is divided by mean annual precipitation over the period of 2011-2019 (Vivoni et al., 2021). This is higher than most of the playa catchment runoff ratios, which can be explained by differences in scale (Figure 19). Some of the highest values may be misleading due to overestimations of inundation volume, especially at the playas in the eastern part of the basin that are less topographically defined.

Table 3. Mean annual and mean monsoon season runoff ratios for playa catchments reported as percentages.

Playa No.	Mean Annual Runoff Ratio (%)	Mean Monsoon Runoff Ratio (%)
3	1.06	0.60
5	0.63	0.63
6	0.87	0.80
7	0.24	0.29
9	0.43	0.43
11	1.48	1.63
12	1.58	2.63
14	9.28	12.15
17	0.65	0.64
18	0.63	0.78
21	0.36	0.41
22	2.83	3.68
23	0.58	0.27
24	1.53	1.54
25	1.15	1.02
28	0.01	0.01
29	6.42	9.06
30	0.02	0.02

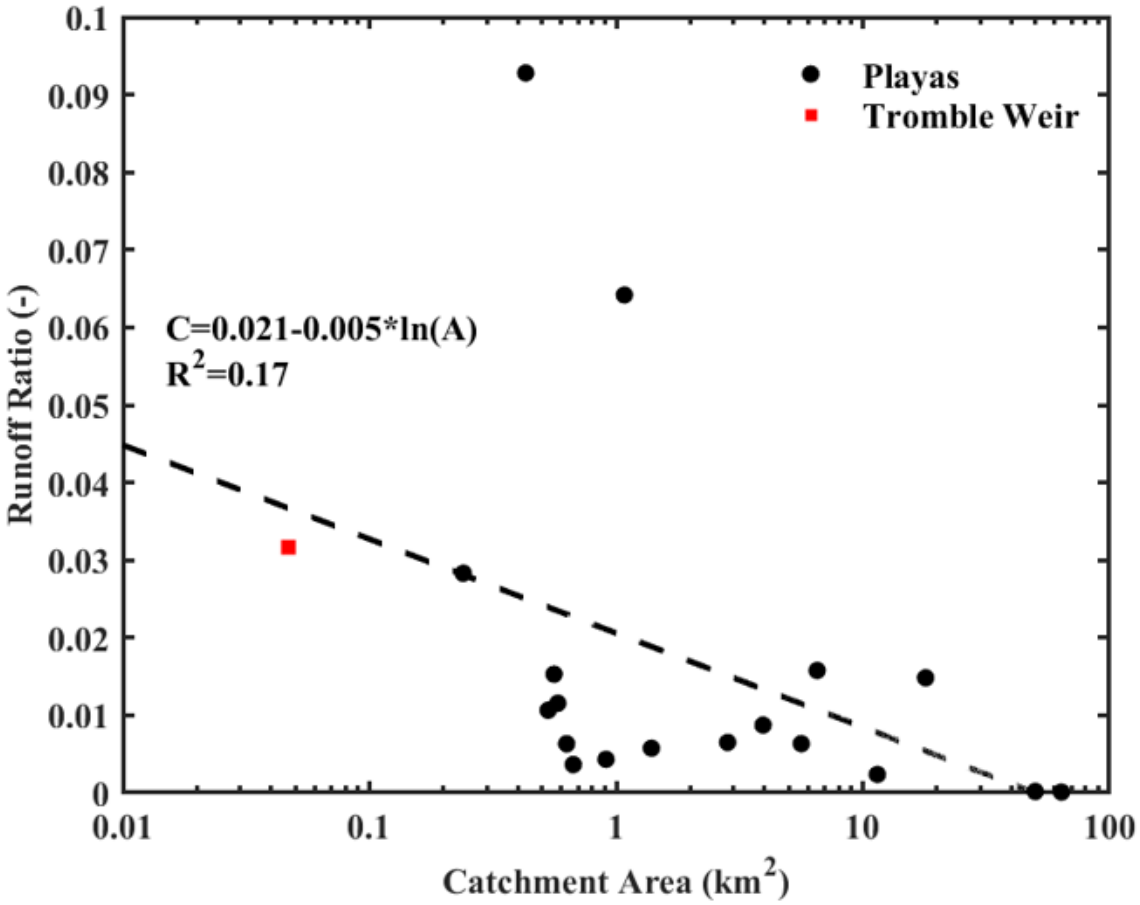

Figure 19. Runoff ratios for playa catchments and the Tromble Weir watershed plotted against catchment area.

Since clearly not all rainfall events result in playa inundation, it is important to understand which ones do and why. One way to understand this is to identify thresholds for playa inundation based on rainfall metrics like precipitation depth and maximum hourly intensity. Precipitation depth, P (mm), is the spatially averaged rainfall depth over the entire playa catchment, including zero values, for a given day or event based on the gauge-corrected, hourly radar product. Maximum hourly intensity, I_{60} (mm/hr), is the maximum rainfall intensity experienced by a pixel within the playa catchment for a given hour during an event. Thresholds were determined for these metrics at an event-scale to

adequately account for the water associated with each inundation and at a daily scale to facilitate comparison with previous studies and application to historical data.

The event-based P and I_{60} thresholds determined for each playa are reported in Table 4, along with their performance metrics. The daily P and I_{60} thresholds with their performance metrics are presented in Table 5. The thresholds from these four metrics are compared in a box-and-whisker plot in Figure 20. On average, the I_{60} thresholds were lower and performed slightly better than the P thresholds. For the event-scale, the average P threshold was 31.6 mm/event, with an average p_o of 0.93, κ of 0.52, 4.62% false positives, and 2.55% false negatives. The average I_{60} threshold was 20.0 mm/hr, with an average p_o of 0.94, κ of 0.55, 4.38% false positives, and 2.06% false negatives Due to the optimization of κ instead of p_o, there were more false positives than false negatives in most cases.

The optimal event-based P thresholds for playa inundation ranged from 16.1 mm at Playa 12 to 71.3 mm at Playa 28. The optimal event-based I_{60} thresholds for playa inundation ranged from 8.8 mm/hr at Playa 14 to 40.5 mm/hr at Playa 28. The optimal daily P thresholds ranged from 14.5 mm at Playa 22 to 48.2 mm at Playa 7, with a median of 22.7 mm.

Event-based P and I_{60} thresholds were also determined for the cool season (October to March) and warm season (April to September) and are plotted in Figure 21. It is clear that cool season P thresholds are generally higher than warm season P thresholds, but cool season I_{60} thresholds are generally lower than warm season I_{60} thresholds. This is an interesting behavior that likely relates to the characteristics of the storms that occur in these two seasons. Since cool season rainfall events are generally less intense than warm

Table 4. Event-based rainfall thresholds for playa inundation and their performance metrics. p_o is the fraction of correct predictions, κ is the kappa agreement statistic, FP is the percentage of false positives, and FN is the percentage of false negatives.

Playa No.	P (mm)	p_o	κ	FP	FN	I_{60} (mm/hr)	p_o	κ	FP	FN
3	61.3	0.98	0.49	0.87	0.87	25.2	0.98	0.59	1.35	0.45
5	33.6	0.95	0.53	3.75	1.12	21.7	0.96	0.52	2.76	1.38
6	21.3	0.90	0.54	4.92	5.30	10.1	0.89	0.59	10.27	1.03
7	25.3	0.92	0.37	7.22	0.76	27.6	0.96	0.38	2.28	1.63
9	23.4	0.91	0.54	7.06	1.86	16.7	0.94	0.57	2.94	3.31
11	35.9	0.93	0.48	4.09	2.52	27.3	0.93	0.42	4.68	2.08
12	16.1	0.86	0.54	8.07	5.90	17.3	0.91	0.64	4.45	4.71
14	19.1	0.92	0.74	3.15	4.90	8.8	0.86	0.62	8.82	4.78
17	30.5	0.92	0.49	5.52	2.76	16.9	0.92	0.50	6.08	2.36
18	31.0	0.94	0.57	4.38	1.46	22.0	0.96	0.69	2.14	1.42
21	28.7	0.93	0.48	6.29	0.35	22.2	0.96	0.63	2.81	0.70
22	25.6	0.92	0.61	4.00	3.64	12.3	0.95	0.73	3.30	2.20
23	33.9	0.96	0.60	3.16	1.05	24.5	0.98	0.68	0.69	1.73
24	28.2	0.93	0.56	4.21	2.46	14.2	0.94	0.62	3.60	2.16
25	31.3	0.91	0.43	3.51	5.61	14.2	0.93	0.60	3.64	3.64
28	71.3	0.97	0.25	1.09	1.91	40.5	0.95	0.17	4.00	1.20
29	22.7	0.92	0.60	6.06	1.68	17.4	0.94	0.65	4.14	1.91
30	28.7	0.92	0.46	5.87	1.76	20.8	0.89	0.37	10.90	0.46
Avg.	**31.6**	**0.93**	**0.52**	**4.62**	**2.55**	**20.0**	**0.94**	**0.55**	**4.38**	**2.06**

Table 5. Daily rainfall thresholds for playa inundation and their performance metrics.

Playa No.	P (mm)	p_o	κ	FP	FN	I_{60} (mm/hr)	p_o	κ	FP	FN
3	39.4	0.98	0.59	1.14	0.38	25.8	0.97	0.52	2.83	0.00
5	33.0	0.95	0.48	3.07	1.71	26.7	0.96	0.46	1.29	2.26
6	16.8	0.90	0.60	5.65	4.24	12.5	0.89	0.55	5.96	4.64
7	48.2	0.98	0.45	0.70	1.75	33.4	0.98	0.45	0.63	1.58
9	15.1	0.86	0.45	13.09	0.73	14.3	0.93	0.54	4.49	3.00
11	33.0	0.94	0.48	3.30	2.40	30.3	0.94	0.41	3.55	2.28
12	15.3	0.88	0.60	8.38	3.89	22.2	0.91	0.58	1.35	7.57
14	15.2	0.90	0.70	4.96	4.96	8.0	0.84	0.57	9.69	6.20
17	20.4	0.89	0.41	9.03	2.34	14.7	0.91	0.47	6.16	2.74
18	22.3	0.90	0.43	8.19	1.42	13.7	0.93	0.58	6.57	0.36
21	23.0	0.92	0.48	8.04	0.00	21.6	0.95	0.46	2.52	2.16
22	14.5	0.90	0.61	9.63	0.74	11.2	0.94	0.71	3.92	2.35
23	29.9	0.95	0.53	4.08	1.36	28.6	0.97	0.53	0.68	2.74
24	18.9	0.91	0.51	7.61	1.73	14.0	0.95	0.70	2.97	1.86
25	23.4	0.92	0.58	4.51	3.82	12.7	0.93	0.67	3.38	3.38
28	29.9	0.94	0.21	4.85	1.53	51.3	0.97	0.12	0.79	1.78
29	22.3	0.92	0.55	5.14	3.22	16.5	0.92	0.54	3.90	3.90
30	34.9	0.94	0.38	3.31	3.04	20.5	0.89	0.34	10.11	0.92
Avg.	**25.3**	**0.92**	**0.50**	**5.82**	**2.18**	**21.0**	**0.93**	**0.51**	**3.93**	**2.76**

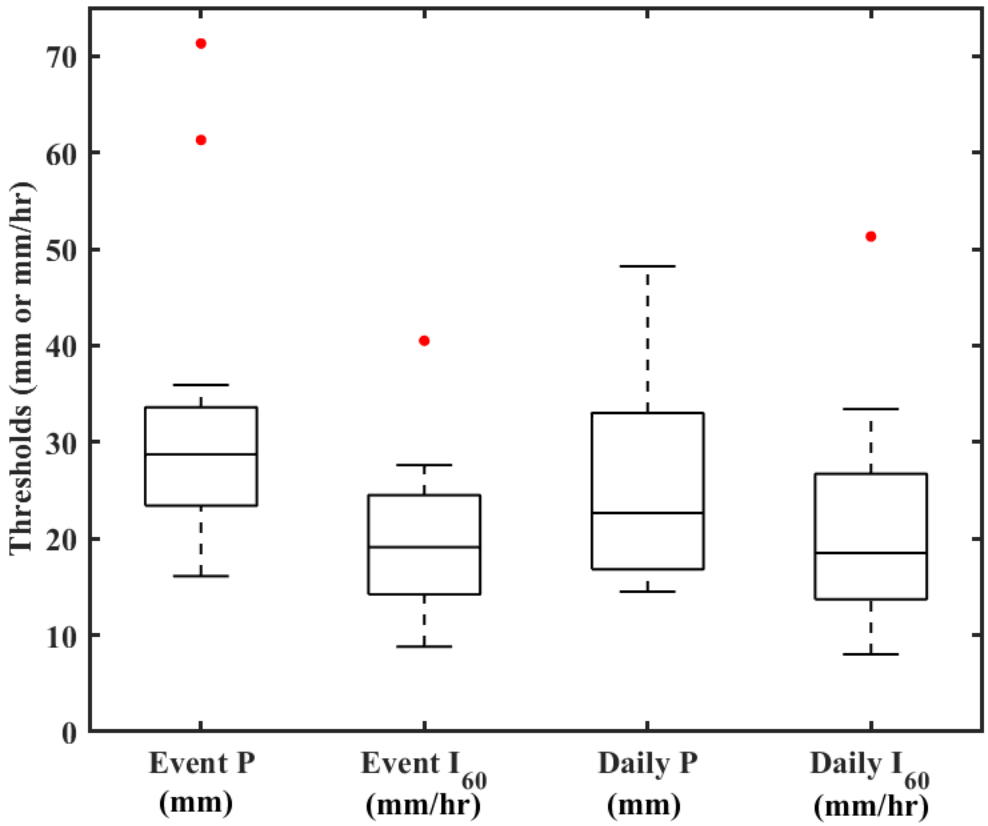

Figure 20. Box and whisker plot of the P and I_{60} thresholds obtained for all playas.

season events, the total amount of rainfall needs to be higher in order to inundate the playa. This can be seen in Figure 22, where some of the largest rainfall events are seen during the cool season. Lower intensity thresholds in the cool season could be related to the large magnitudes of the storms that cause inundation or to a decrease in infiltration capacity of the soil that allows less intense rainfall to generate overland flow (Etheredge et al., 2004). Although the rainfall intensity that leads to cool season inundation is lower, they are often the significantly more intense than other cool season storms, as seen in Figure 23 below, where very few intense cool season storms did not lead to inundation. This suggests that intensity is still important in the cool season, not just the rainfall depth.

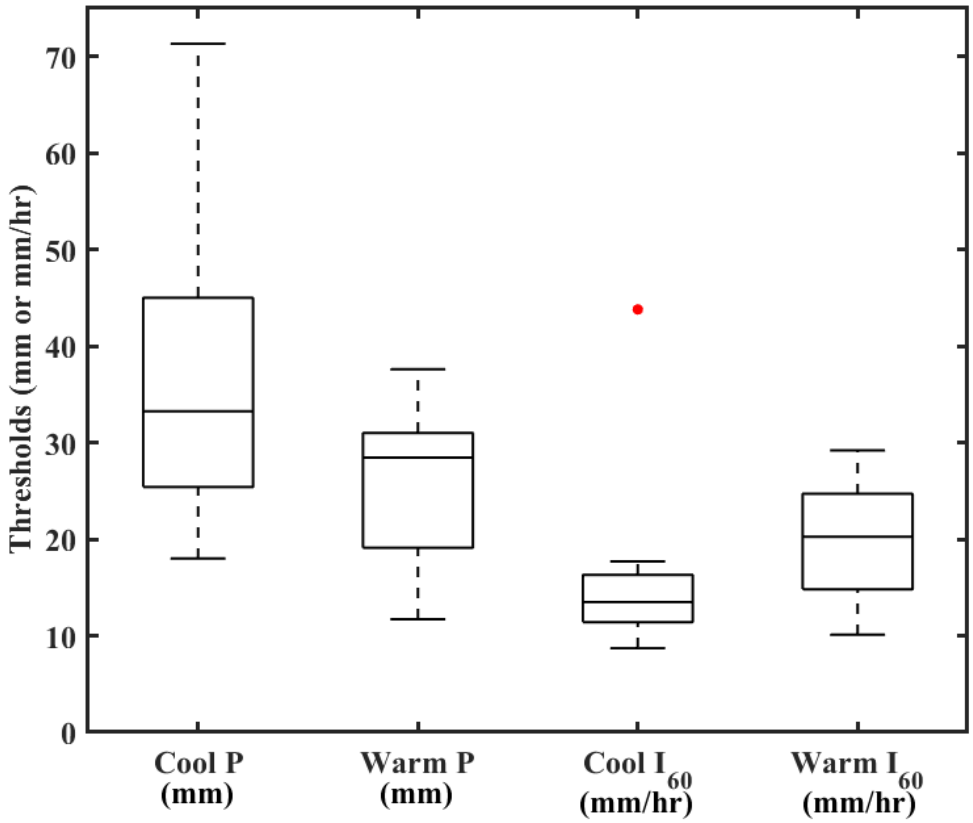

Figure 21. Box and whisker plot of the P and I60 thresholds obtained for the cool and warm seasons.

It is important to recognize that no threshold is perfect, but it can provide an idea of a value above which inundation is more probable. McKenna and Sala (2018) proposed a daily P threshold of 20 mm, which falls within the range of plausible thresholds for inundation, although most daily P thresholds determined through the optimization of κ are greater than 20 mm. Figures 22 and 23 show scatterplots of playa inundation volume, V, against event P and I_{60} for Playas 6, 12, 22, and 29, plotted with their respective thresholds and color-coded for the cool and warm seasons. It should be noted that the thresholds are not placed at the lowest rainfall value that caused inundation, since they were chosen based on which threshold value produced the highest kappa agreement

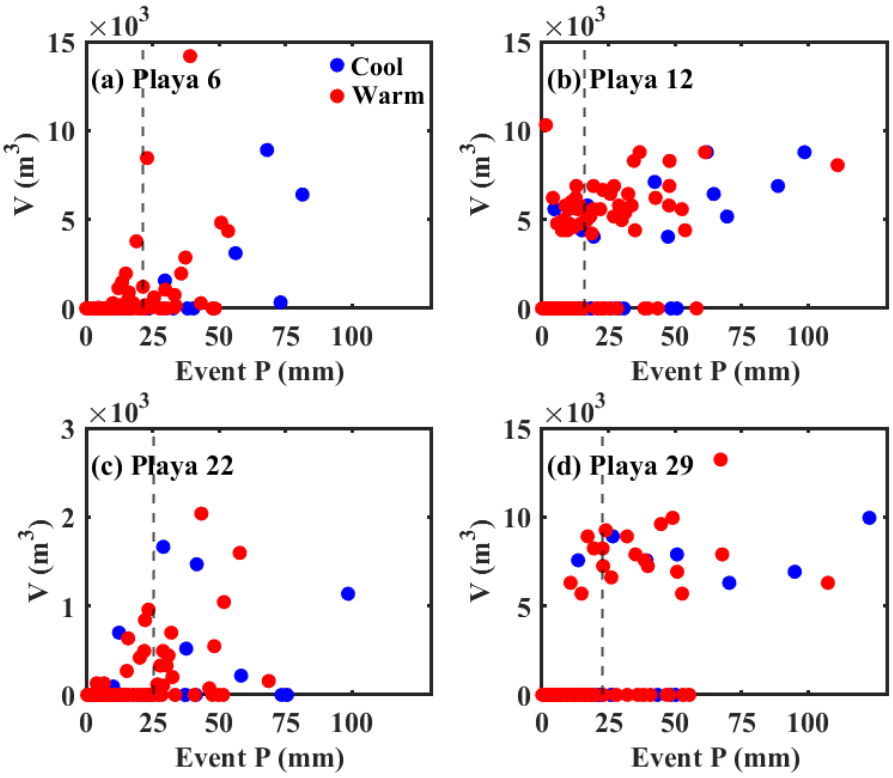

Figure 22. Playa inundation volumes versus event P at (a) Playa 6, (b) Playa 12, (c) Playa 22, and (d) Playa 29, plotted with their respective thresholds as vertical dashed lines. Colors show which events occurred during the cool and warm seasons. Note the different scale for subplot (c) to accommodate lower inundation volumes.

statistic, κ (Equation 2.3). These plots show the data that were used to select the threshold for these playas by optimizing κ, and all points greater than the threshold are assumed to represent inundation, while all points lower than the threshold are assumed to not be inundation. The plots make it apparent that large and intense rainfall events are the most likely to cause inundation. These events are able to initiate ponding and runoff generation that rapidly inundate the playa. Larger rainfall values are also associated with larger inundation volumes, and a linear relationship was derived at each playa between these two variables at the daily scale, with the regressions reported in Table 6 and an example shown for Playa 6 in Figure 24. These relationships were calculated for

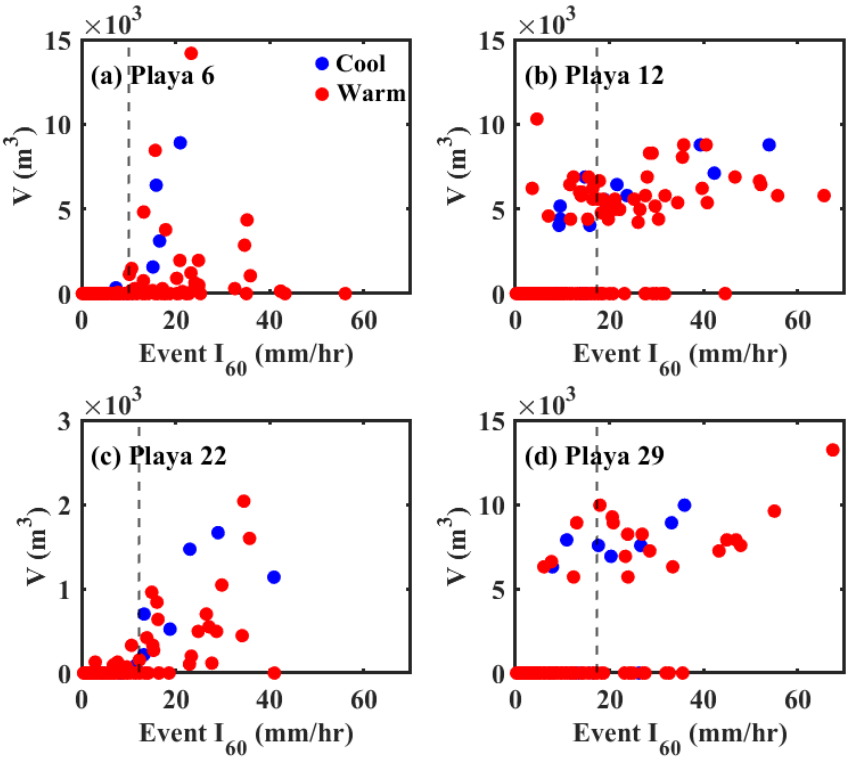

Figure 23. Playa inundation volumes versus event I_{60} at (a) Playa 6, (b) Playa 12, (c) Playa 22, and (d) Playa 29, plotted with their respective thresholds as vertical dashed lines. Note the different scale for subplot (c) to accommodate lower inundation volumes.

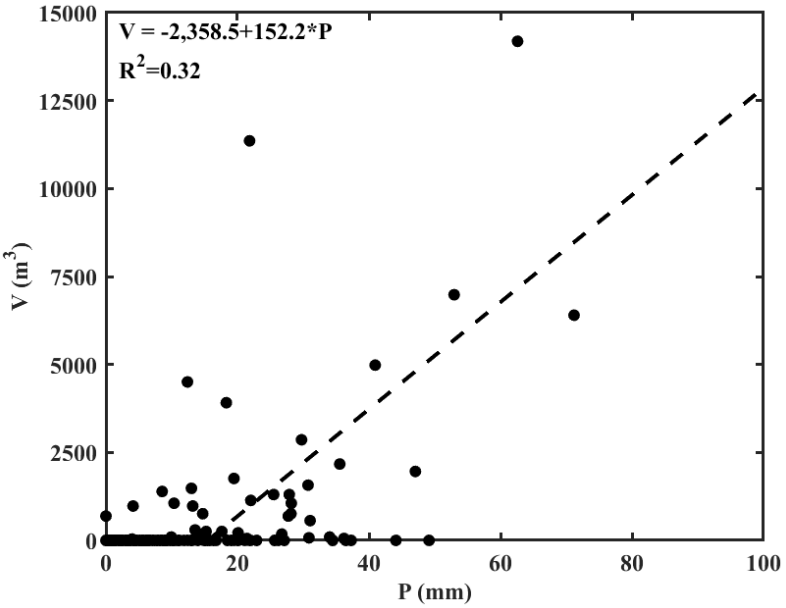

Figure 24. Relationship between daily P and inundation volume at Playa 6.

Table 6. Details for the linear regressions between daily precipitation and water volume for each playa.

Playa No.	Slope (m^3/mm)	Intercept (m^3)	R^2
3	57.3	-376.5	0.49
5	323.2	-6354.7	0.27
6	152.2	-2358.5	0.32
7	3061.5	-145035.7	1.00
9	10.7	88.1	0.11
11	25.7	44879.2	0.10
12	38.5	5259.8	0.16
14	15.3	1282.2	0.05
17	6.9	1847.2	0.02
18	8.0	282.9	0.17
21	-3.4	622.0	0.02
22	19.6	50.5	0.28
23	-1.3	1840.6	0.00
24	51.2	-677.6	0.34
25	28.3	-346.2	0.12
28	258.7	-7508.4	0.70
29	37.0	6938.8	0.07
30	-10.1	2701.7	0.09

inundation events that were above the daily precipitation threshold and were used later to estimate playa inundation from historical rainfall records.

To help understand the drivers of inundation, it is useful to examine specific inundation events that behave as expected, as well as those that do not. A sequence of inundation events at Playa 12 in July and August 2017 provides great examples of both of

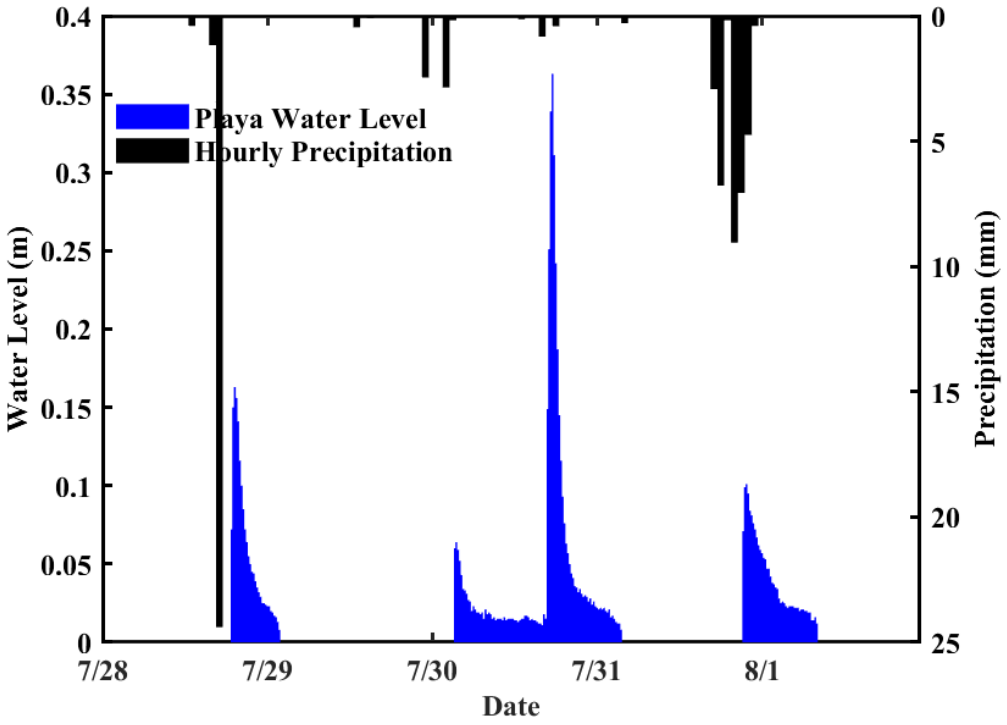

Figure 25. Timeseries of water level and precipitation at Playa 12 during a sequence of inundation events in July-August 2017.

these cases and is shown in Figure 25. The first inundation event was quite typical and was associated with 25.97 mm of rainfall on July 28. This is greater than Playa 12's threshold for inundation, so it is no surprise that inundation occurred. The subsequent events, however, were associated with surprisingly low rainfall amounts. For example, the inundation event early in the morning on July 30 was caused by only 5.64 mm of precipitation that fell late in the day on July 29. This event's I_{60} of 18.27 mm/hr and the fact that it occurred only 1 day after another inundation very likely played a role in allowing the playa to inundate. Later in the day on July 30, an event of only 1.47 mm occurred while the playa was still inundated from the previous rainfall, leading to a substantial increase in water level. The next day, another inundation event occurred, although this one was associated with a greater rainfall depth.

The causes of this behavior are related to both rainfall characteristics and the physical setting of this playa. The first event demonstrates the most common way that a playa inundates, which is after a large rainfall event. The second, third, and fourth events in the sequence mentioned above occurred within a day of the inundation preceding them. This suggests that precipitation falling on a wet playa soil is more likely to inundate it. In the case of the 1.47 mm precipitation event, this water fell directly onto a ponded area, increasing the water level through this and whatever runoff came from the catchment. The magnitude of the increase is slightly suspicious, however, and could be related to error in the water level sensor.

As part of the Island Chain playas, Playa 12 is located within a rather lush depression along a fault, and connectivity among low points in this feature could effectively increase the contributing area of the playa. Figure 26 shows a DEM of the area surrounding Playa 12, and it is clear that the area directly west and northwest of the water level sensor is lower than the terminus of the catchment. The potential inundation of these lower areas and connectivity across the playa catchment boundary makes it challenging to define the boundary of Playa 12 and its catchment and should be taken into account when analyzing the rainfall-inundation processes at this location.

Usually, inundation-causing rainfall events have high intensities as well as rainfall depths. A good example of this is a 57.79 mm event that led to inundation on June 1, 2017 at Playa 22. This storm's maximum intensity was 35.73 mm/hr, and it had a duration of 5 hours, both characteristic of summer monsoon storms. Large rainfall events with low intensities are not always able to inundate playas. A 73.48 mm event on November 27, 2019 did not cause inundation at Playa 22. The maximum intensity of this

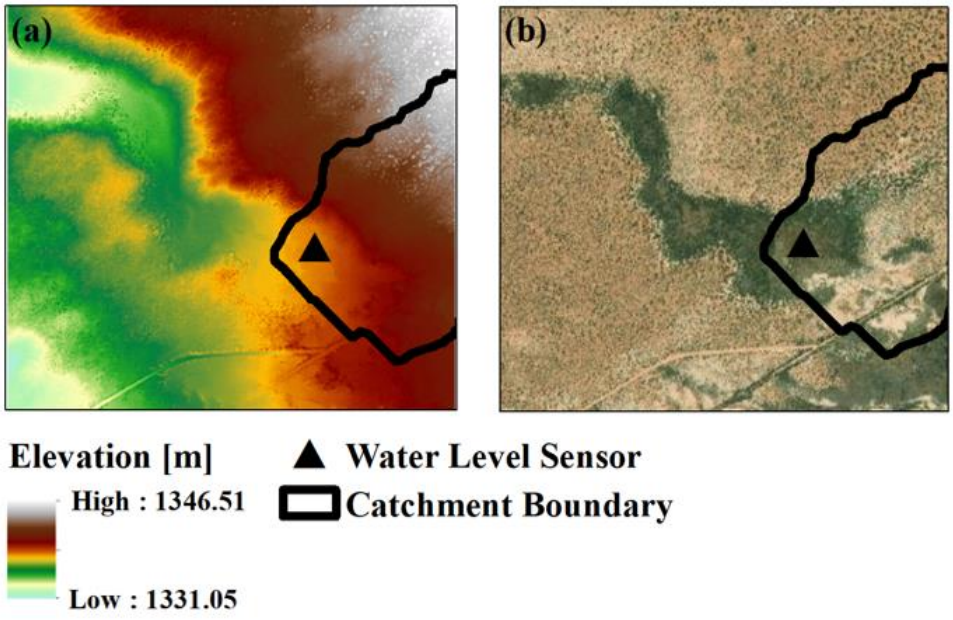

Figure 26. The downstream end of Playa 12's catchment and its water level sensor shown in the context of the southeast to northwest trending verdant depression associated with normal faulting, visualized with (a) a DEM and (b) aerial imagery.

event was only 8.23 mm/hr and the event lasted 30 hours, which is typical behavior for a winter storm. This goes back to the reason why a large majority of playa inundation occurs during the summer months. Winter storms are often not intense enough to produce runoff by infiltration excess. These examples are shown graphically in Figure 27, highlighting that while both the winter and summer rainfall events at Playa 22 were large, the shorter and more intense summer storm was the one that caused inundation.

In larger catchments, the distance of the storm from the playa can be important for determining whether the playa inundates. At Playa 30, which is adjacent to Playa 29, a 13.84 mm rainfall event on August 19, 2017 with a maximum I_{60} of 47.90 mm/hr resulted in inundation. The catchment average depth was lower than the threshold for inundation, but the intensity was high, the storm was located right over the playa (Figure 28b), and the playa itself saw a total of 49.46 mm of precipitation during this storm. Figure 28a

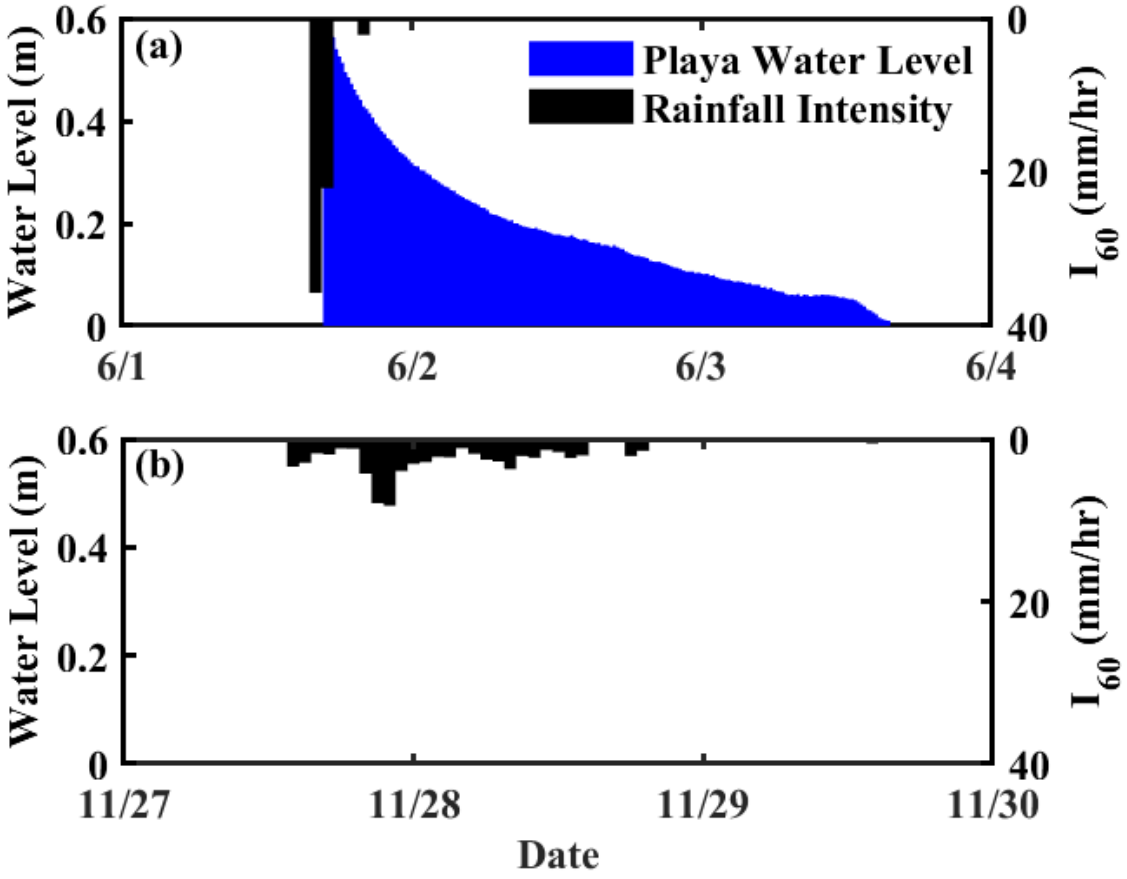

Figure 27. Comparison of (a) a high intensity rainfall event in 2017 that resulted in inundation and (b) a large, but less intense rainfall event in 2019 that did not result in inundation at Playa 22.

shows a 22.16 mm rainfall event on September 30, 2017 with a maximum intensity of 55.55 mm/hr did not lead to inundation, despite exceeding the I_{60} threshold of 20.8 mm/hr. A closer look at this event reveals that the storm centroid was 8.05 km away from the playa, giving any generated runoff ample opportunity to infiltrate before reaching the playa. Over the playa itself, only 3.23 mm of rain fell. It is evident that storm's distance from the playa can be important when dealing with intense localized storms. Van Vactor (1989) made a similar observation at the College Playa on the CDRRC (known as Playa 7 in this study). He found that all inundation events at the playa were associated with

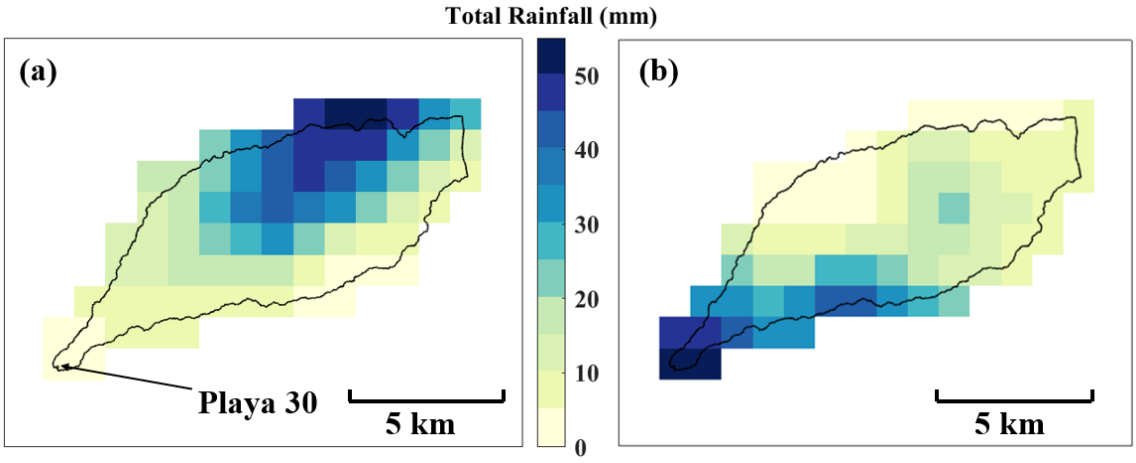

Figure 28. Spatial map of (a) September 30, 2017 storm event that did not cause inundation in Playa 30 and (b) August 19, 2017 storm event that did cause inundation in Playa 30.

precipitation at the playa's rain gauge, but there wasn't always precipitation in the upstream catchment associated with these inundations. The example at Playa 30 and the results of Van Vactor (1989) suggest that playa inundation typically requires precipitation at the playa itself and does not always require contribution from upstream areas.

Spatial Controls on Inundation

Given the variety of playa types and playa catchment characteristics across the 18 sites, it is important to understand how these properties affect playa inundation behaviors and search for relevant patterns. Some of these patterns can be explained simply by the groupings of playas based on location and origin. Figure 29 shows the typical playa behavior types mapped with the geological playa groupings. Of course, there are exceptions that exhibit behaviors slightly different than playas with similar origins, but the groupings do help understand some of the spatiotemporal variability.

The Island Chain playas, 12 and 14, both demonstrate uniquely frequent and rapid inundations. The Karst Depression playas located on the basin floor tend to behave similarly to each other, with rapid events that are deeper on average than other playas. Variation in inundation response within Karst Depression playas can partially be explained by the varying amounts of sand that have been blown onto them by the prevailing winds from the southwest. Although their origin is different, the Piedmont Slope playas have similar behaviors to some of the Karst Depression playas, but with generally shallower inundations.

The Uplifted Plain playas on the CDRRC exhibit similar behavior to each other, but they too have differences among them. Playa 6 and especially Playa 7 show signs of vertisol formation, where large cracks form in the soil as a result of expansion and contraction associated with wetting and drying (Wondzell et al., 1990). This is an indicator of high clay content, which may contribute to these playas' longer inundation durations. Another consideration that this grouping exemplifies is the effect of roads on runoff and playa inundation. Playa 6 is located near a curve in the road coming from the CDRRC Headquarters, and the playa has a large arroyo leading to it that starts at this road. Figure 30 illustrates how this road, which is visible on the DEM of the area, can act as a significant conduit for water heading to the playa. Many of the playas have roads within their catchments that may affect to varying degrees how runoff reaches the playa. Ramos-Scharrón and LaFevor (2018) studied the effect of unpaved roads on runoff generation in ephemeral catchments in a tropical dry climate on the U.S. Virgin Islands and found that roads generally increased the frequency of runoff and allowed smaller storms to generate runoff. The same concept can be applied to the JER and CDRRC,

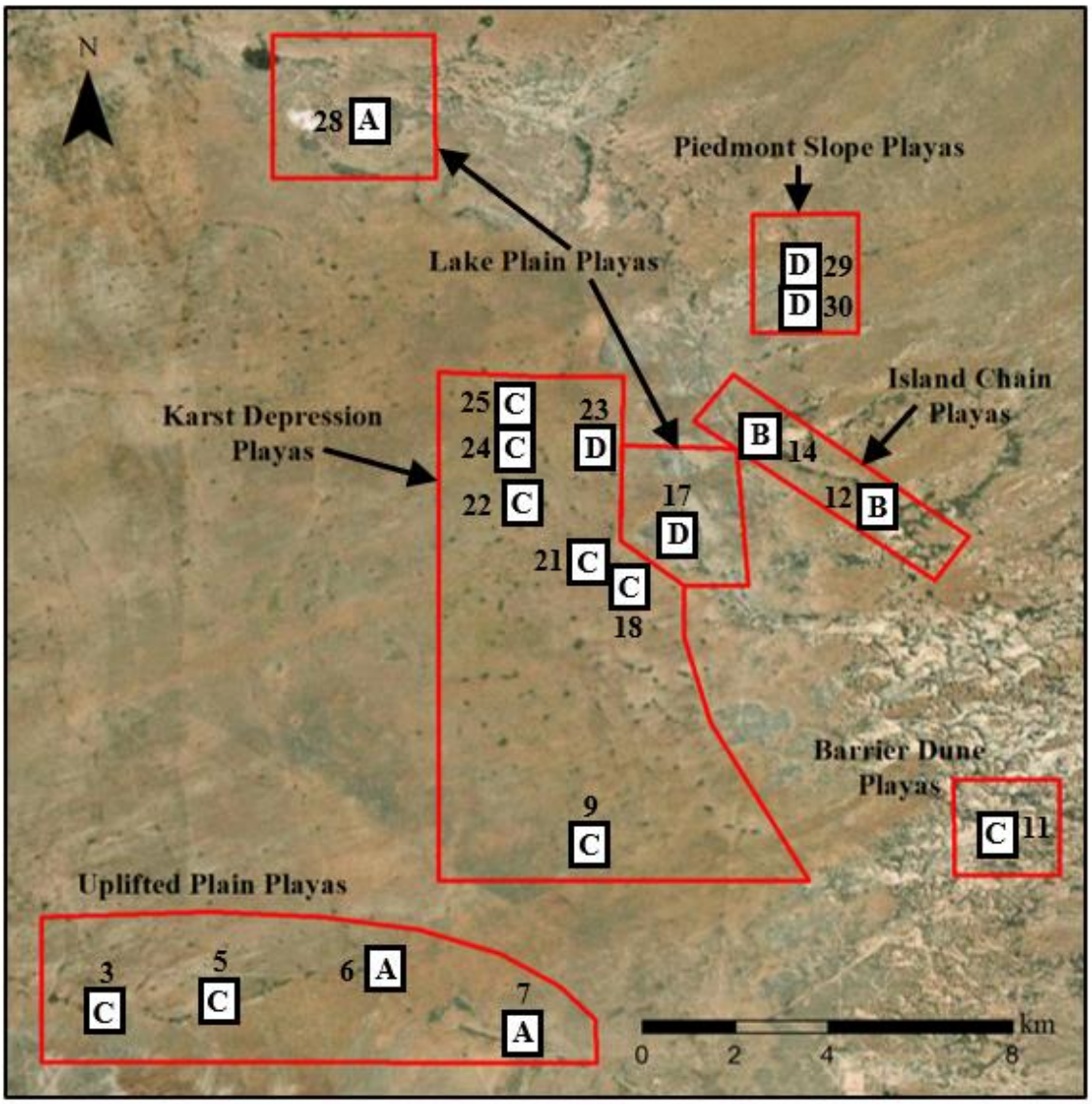

Figure 29. Map of playa behavior types with playa groupings based on origin and geology. “A” represents long, deep events; “B” rapid, shallow, and frequent events; “C” rapid, deep events; and “D” rapid, shallow, and infrequent events.

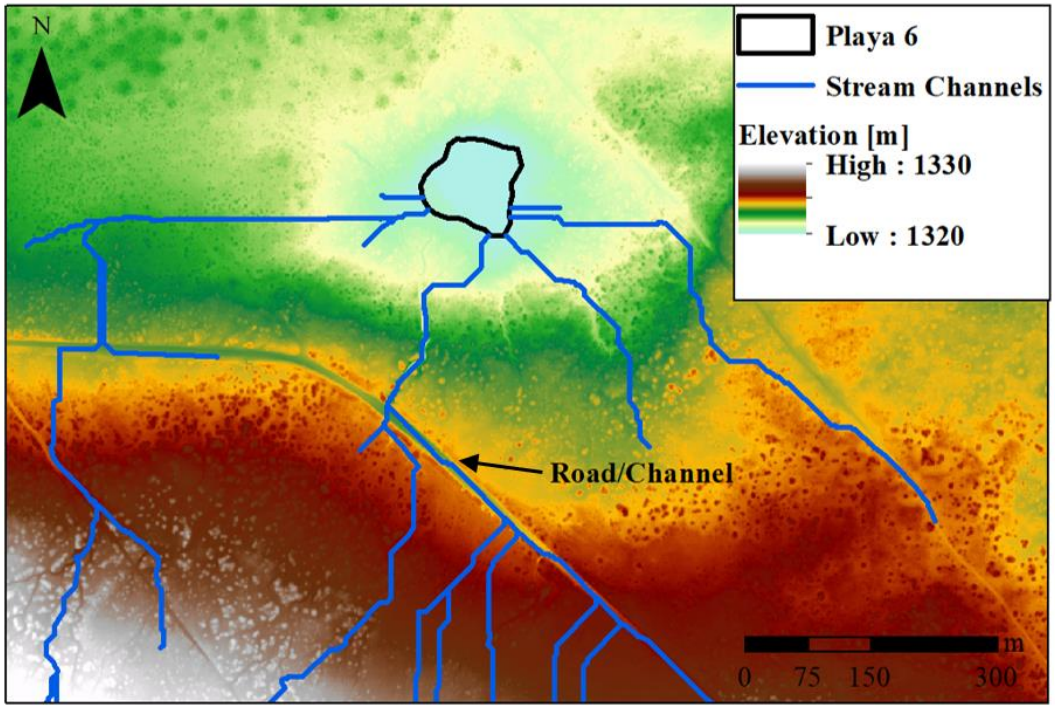

Figure 30. Map of drainage network flowing into Playa 6, showing where a road and stream channel coincide just upstream of the playa.

where many unpaved roads exist to aid in cattle ranching and research activities, while also altering the flow of water across the landscape.

Playas 17 and 28, the Lake Plain playas, both see infrequent, shallow events. These are by far the largest playas examined in this study, which means they have more surface area for water to spread out. The cause for Playa 17's very shallow inundations (0.04 m on average) may not be entirely natural, however, since the playa contains a dirt stock tank within it that captures some of the water that would otherwise be recorded by the water level sensor. Russell et al. (2020) examined the effects of modification on playas and found that playas in the Great Basin with dugouts (dirt stock tanks) were more likely to hold water than unmodified playas. It could be that at Playa 17 the stock tank inundates more frequently than the playa would have otherwise, but the undisturbed

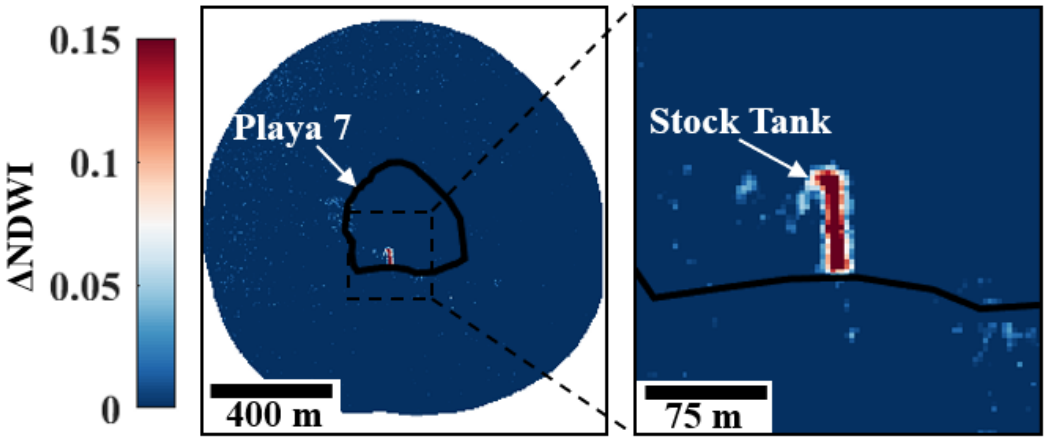

Figure 31. Planet imagery showing that Playa 7 was dry, but the stock tank inside of it was inundated on October 7, 2019.

playa surface where the water level sensor is located does not see much inundation. Other playas may be affected by stock tanks as well. Playa 7 has a stock tank within it (Figure 31), but it has not been known to be a detriment to its inundation behavior or ecological function. Playa 11 has a stock tank upstream of it that may be intercepting water that would otherwise end up in the playa. Land managers in the Great Basin have considered filling in dugouts to restore the ecological function of the playas in areas where cattle grazing no longer occurs (Russell et al., 2020). In the Jornada Basin, since the area is still used for grazing, stock tanks within the playas are useful and strategic locations for capturing water despite their potential effects on playa hydrology.

Important Catchment Characteristics for Inundation

While the groupings based on geological origin are useful to understand playa behaviors, other factors like catchment area, slope, soil properties, and ground cover are important physical attributes to consider that have been examined in other studies (Kampf et al., 2018; McKenna and Sala, 2018). Even within the geological groupings, these

catchment characteristics can vary. To understand the relative importance of these factors for causing playa inundation, regressions were performed in JMP Pro version 16.0.0. Prior to this, the predictor variables were tested for collinearity by performing linear regressions between each of them. The catchment variables tested were the natural log of catchment area (A), average slope (S), average bare ground (BG), and average sand fraction (SF) within each catchment. Bare ground was used as a proxy for vegetation cover in the catchments. Similar combinations of factors have been examined and deemed important in other studies that have characterized their effects on runoff generation (Kampf et al., 2018) and playa groundwater recharge (McKenna and Sala, 2018). Figure 32 is a scatterplot matrix showing the relationships between each variable, and it is apparent that there is a strong linear correlation between the natural log of catchment area and bare ground. This relationship has a coefficient of determination, R^2, equal to 0.68, meaning that the natural log of catchment area explains 68% of the variation in vegetation fraction. This correlation is important to keep in mind when interpreting the effect of bare ground on playa inundation. The likely explanation for this correlation is that larger catchments tend to include areas on the piedmont slope and mountain block that have less bare ground, thus decreasing the percentage of bare ground in the catchments. Other variables, such as slope and the log of catchment area, show some collinearity (R^2 of 0.12) but not as much as bare ground and the log of catchment area.

Variable selection for the multiple logistic regression was performed through a stepwise regression, which used forward selection to determine the combination of variables that resulted in the lowest corrected Akaike's Information Criterion (AICc) and

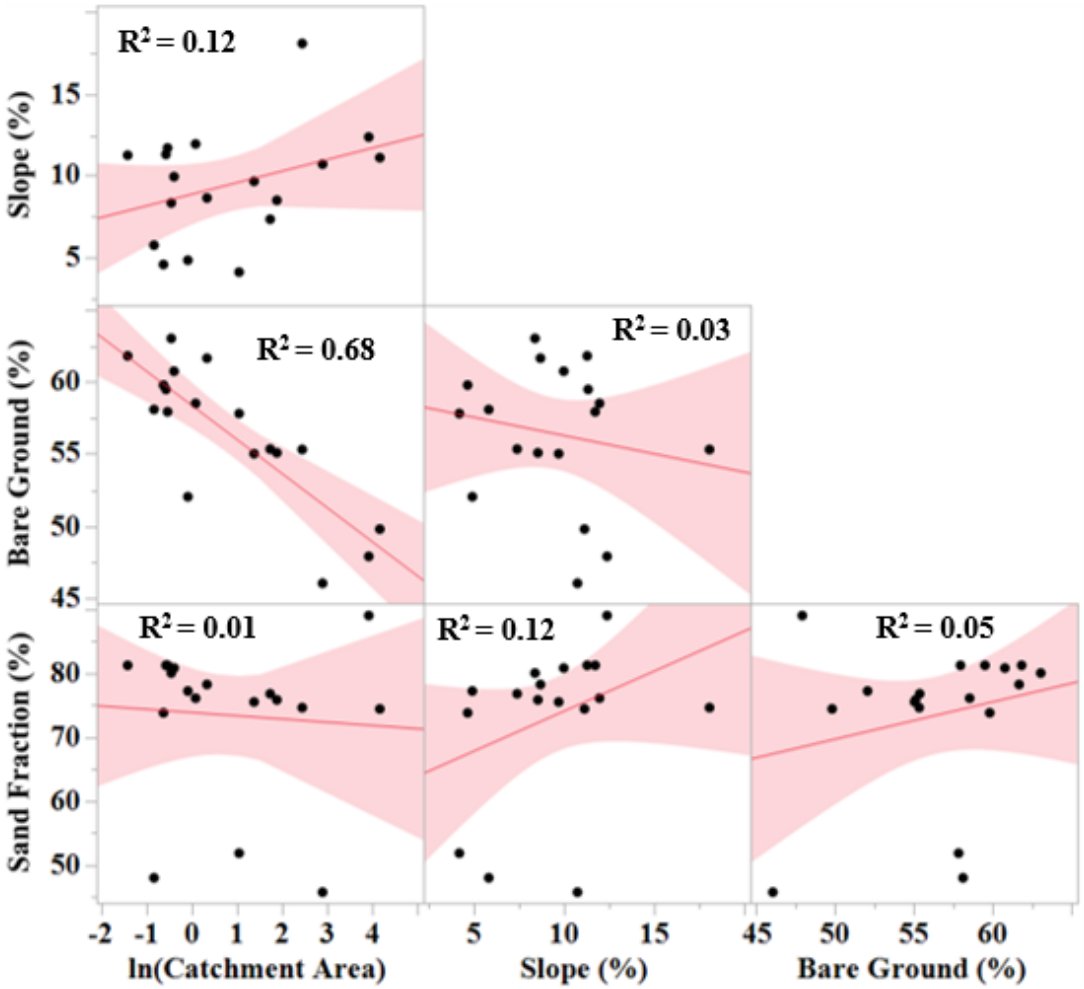

Figure 32. Scatterplot matrix of catchment variables examined in the regression analysis, shown with lines of best fit, 95% confidence intervals, and R^2 values.

the best fitting model. In addition to the catchment variables mentioned above, precipitation data was also included as an independent variable since it is a known driver of inundation, and the response variable was binary inundation data from all playas. The precipitation data, as event P and I_{60}, were each included separately with the catchment variables and were used individually in simple logistic regressions to see how adding the catchment variables affected the accuracy of the model predictions. All predictor variables were log-transformed and standardized to account for skewness and the

different scales among the variables. The variable selection process removed catchment slope and bare ground from the regression, with the best fitting model including just precipitation, catchment area, and sand fraction. The coefficients and performance of the individual P and I_{60} models, as well as the best fitting models with catchment characteristics, are summarized in Table 7. For P, adding catchment characteristics to the regression only marginally improved the fit and accuracy. For I_{60}, adding catchment characteristics improved the model more noticeably. These results suggest that the occurrence of playa inundation can be predicted using precipitation alone nearly as well as considering catchment factors in addition to precipitation, an observation that was also made in Kampf et al. (2018). The same procedure was also applied to data just from the monsoon season months of July, August, and September, and the results were similar (Table 8). The most notable difference was that the AICc values were lower, indicating that the model does a better job of predicting playa inundation when only the monsoon season is considered.

The coefficients of these regressions suggest that catchment area is the most influential catchment property, followed by sand fraction. McKenna and Sala (2018) used a model to determine that larger, steeper, and less sandy catchments led to more groundwater recharge in playas, with vegetation cover not being important. The logistic regression here has a negative coefficient for catchment area, implying that larger catchments are associated with a lower likelihood of playa inundation. This does not represent the effect of area on total runoff volume, however, which could be different. The negative coefficient for sand fraction also indicates that sandier catchments are

Table 7. Coefficients and performance of logistic regressions applied to precipitation and catchment variables. Values of *b* are the coefficients of the respective variables, with their standard error in parentheses and significance level represented with asterisks (* is significant at the 0.01 level).

Coefficient	P	All	I_{60}	All
b_1 (P/I_{60})	1.93 (0.11)*	1.95 (0.11)*	1.80 (0.10)*	2.20 (0.12)*
b_2 (Area)	-	-0.29 (0.08)*	-	-0.85 (0.09)*
b_3 (Sand)	-	-0.20 (0.07)*	-	-0.21 (0.07)*
R^2	0.33	0.34	0.28	0.35
AICc	1178	1163	1262	1149
p_o	0.94	0.94	0.92	0.93
κ	0.31	0.35	0.14	0.32
FP	0.48	0.58	1.06	0.96
FN	5.76	5.48	6.53	5.57

Table 8. Coefficients and performance of logistic regressions applied to precipitation and catchment variables for only the monsoon season. Values of b are the coefficients of the respective variables, with their standard error in parentheses and significance level represented with asterisks (* is significant at the 0.01 level).

Coefficient	P	All	I_{60}	All
b_1 (P/I_{60})	2.02 (0.14)*	2.02 (0.14)*	1.67 (0.13)*	2.11 (0.15)*
b_2 (Area)	-	-0.22 (0.10)	-	-0.87 (0.11)*
b_3 (Sand)	-	-0.25 (0.09)*	-	-0.25 (0.09)*
R^2	0.33	0.34	0.24	0.31
AICc	786	778	889	807
p_o	0.92	0.92	0.91	0.91
κ	0.37	0.34	0.15	0.29
FP	1.85	2.18	1.34	2.18
FN	5.89	6.06	7.58	6.39

associated with a lower likelihood of playa inundation, which agrees with McKenna and Sala (2018). The apparently insignificant effect of slope on the occurrence of playa inundation is contrary to expected based on Kampf et al. (2018) and McKenna and Sala (2018). This could be due to slight correlation between slope and catchment area, which would be caused by the larger catchments including areas farther up the piedmont slope and mountains that are steeper. It is also possible that not all the catchment averages accurately represent the slopes of the areas that most frequently contribute runoff to the playas.

In addition to the logistic regressions, multilinear regressions were also performed to test the role of catchment properties in determining inundation volume. The same variable selection process as was used for the logistic regressions was applied to the multilinear regressions, and all variables were selected. The variables included in the regressions therefore consisted of P or I_{60}, catchment area, sand fraction, bare ground fraction, and slope, all of which were log transformed and standardized. The dependent variable, inundation volume, was also log transformed and standardized. The results of these regressions are summarized in Table 9. Based on the magnitudes of the coefficients, catchment area is the catchment factor with the largest effect on inundation volume, followed by sand fraction, bare ground fraction, and slope. The signs of the coefficients show that sandier catchments are associated with lower inundation volumes, and larger, barer, and steeper catchments are associated with higher inundation volumes. These results generally align with those seen by researchers like McKenna and Sala (2018), and greater inundation volume can also be understood to mean greater groundwater recharge.

Table 9. Coefficients and performance of multilinear regressions applied to precipitation and catchment variables to predict inundation magnitude.

Coefficient	P	I_{60}
b_1 **(P/I_{60})**	0.19 (0.04)*	0.22 (0.04)*
b_2 **(Area)**	0.62 (0.07)*	0.56 (0.07)*
b_3 **(Sand)**	-0.56 (0.05)*	-0.58 (0.05)*
b_2 **(Bare Ground)**	0.26 (0.07)*	0.25 (0.07)*
b_3 **(Slope)**	0.24 (0.05)*	0.23 (0.05)*
R^2	0.40	0.40
RMSE	0.78	0.78

Spatial Patterns in Thresholds

Just as the inundation responses vary among the playas, so do their thresholds for inundation. Threshold values were examined in terms of each of the four catchment variables included in the above analysis to characterize the effect of these variables. The logistic regression above determined that catchment area and sand fraction were significant for playa inundation, but bare ground and slope were not. Since the thresholds for inundation are related to binary inundation occurrence, the results were similar when comparing catchment properties and thresholds. Figure 33 shows scatterplots of event P and I_{60} thresholds against catchment sand fraction and bare ground. Sand fraction did not have a clear relationship with P and I_{60} thresholds. One would expect this to be a positive correlation, since a higher infiltration capacity would mean a higher rainfall intensity is needed to generate runoff, but there appears a broad range of threshold values for even among similar sand fractions. This is somewhat surprising given the result of the logistic regression, but some difference is reasonable since precipitation thresholds are not

exactly the same as flow occurrence. There could also be some uncertainty in these results related to the reliability of the soil data and the coarse resolution. There is an apparent negative correlation between event P and I_{60} thresholds and bare ground, which is most likely a result of its correlation with catchment area as described above. This makes it complicated to characterize the effect of vegetation on this scale. Additionally, the percentage of bare ground far upstream in the catchment is likely not as important as the bare ground closer to the playa, which could make the catchment average value misleading. A negative trend like this would be logical, however, since more bare ground and less vegetation would lead to greater runoff production and cause the playa to inundate. The effect of vegetation on runoff was demonstrated by Schlesinger et al. (1999), who performed rainfall simulation experiments at runoff plots at the CDRRC and found that plots on bare intershrub areas produced more runoff than grassland and shrubland plots.

Slope appears to behave differently for P and I_{60} thresholds, as shown in Figure 34. The decreasing trend associated with the precipitation thresholds makes sense, since steeper catchments should produce runoff and therefore inundation more easily. The increasing trends associated with I_{60} is contrary to what is expected. The correlation has a low value of R^2, but it suggests that higher slopes have higher thresholds. This is counter-intuitive since higher slopes should facilitate runoff production and thus lower thresholds, as mentioned above. Kampf et al. (2018) observed decreases in thresholds as slope increased. The cause of this unexpected result for I_{60} thresholds and slope could be related to correlation with catchment area, since larger catchments at this site tend to have higher average slopes because they include more mountainous areas.

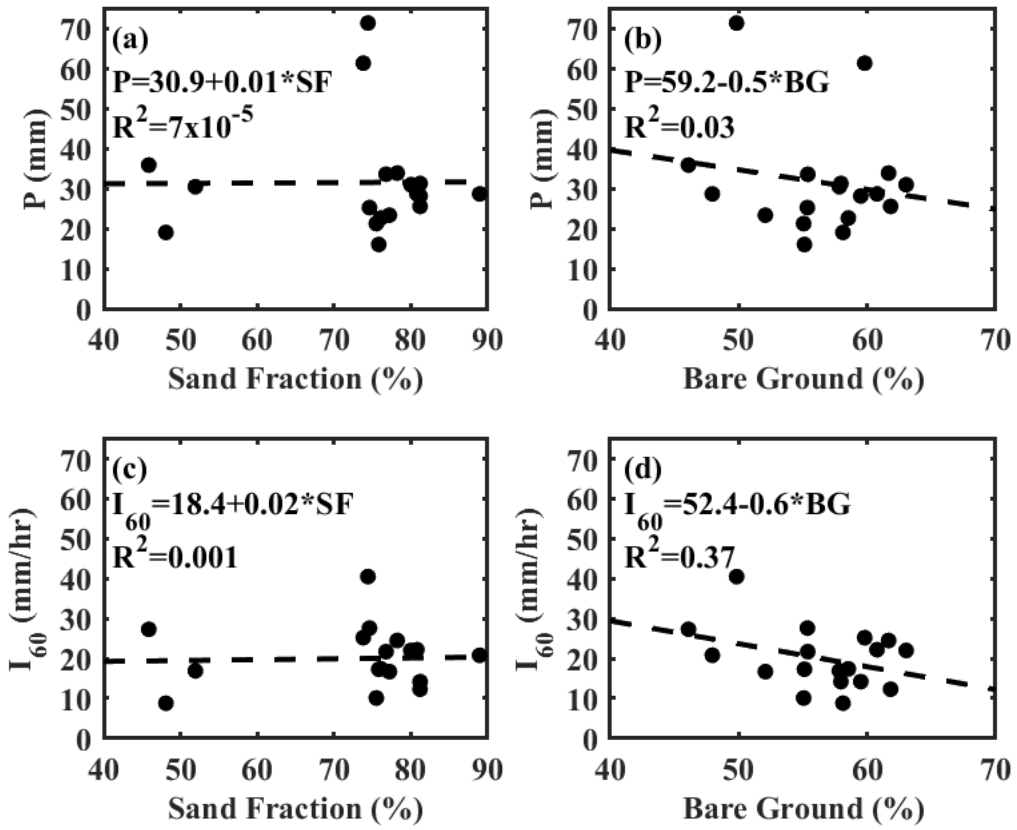

Figure 33. Scatterplots showing the relationship between event P thresholds and (a) sand fraction and (b) bare ground and the relationship between event I60 thresholds and (c) sand fraction and (d) bare ground.

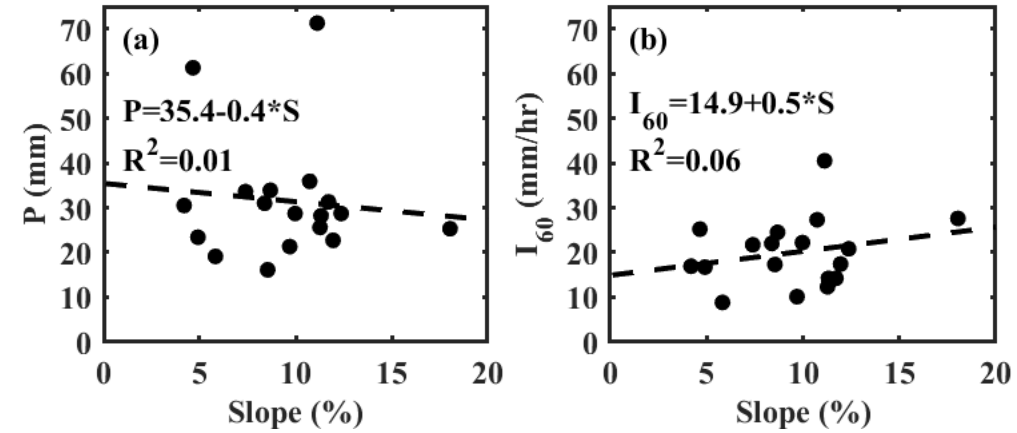

Figure 34. Scatterplot of (a) event P thresholds versus catchment slope and (b) event I60 thresholds versus catchment slope.

Similar to the result of the logistic regression, catchment area was found to be an important factor. For both the event P and I_{60} thresholds, larger catchments tended to have higher thresholds for inundation. This is demonstrated in Figure 35, which shows the event P and I_{60} thresholds plotted against catchment area, as well as their kappa agreement statistics versus catchment area, with catchment area on a logarithmic scale. These plots suggest that larger playa catchments generally need greater amounts of rainfall and higher rainfall intensities in order for the playa to inundate. They also show that larger catchments have lower values of κ and are possibly less reliable. When examined in light of the playa groupings and response types developed previously, it is apparent that the relationship between I_{60} thresholds and catchment area can be different for these different categories (Figure 36). For example, the relationship between I_{60} thresholds and catchment area for the Karst Depression playas appears to still follow a trend similar to the overall line of best fit, while the relationship for the Uplifted Plain playas is less clear due to an outlier. The relationships for the different response types in Figure 36b appear to be clearer, and the relationships for response types A and D appear to have different slopes than the overall trend.

The correlation between thresholds for inundation and catchment area is somewhat expected, since runoff generation studies have seen similar trends in scaling of catchment behavior and have attributed this to partial storm coverage and channel transmission losses (Kampf et al., 2018; Goodrich et al., 1997; Kirkby et al., 2005; Simanton and Osborn, 1983). Larger catchments experience a greater number of rainfall events than smaller catchments simply due to their size, and those large events that occur

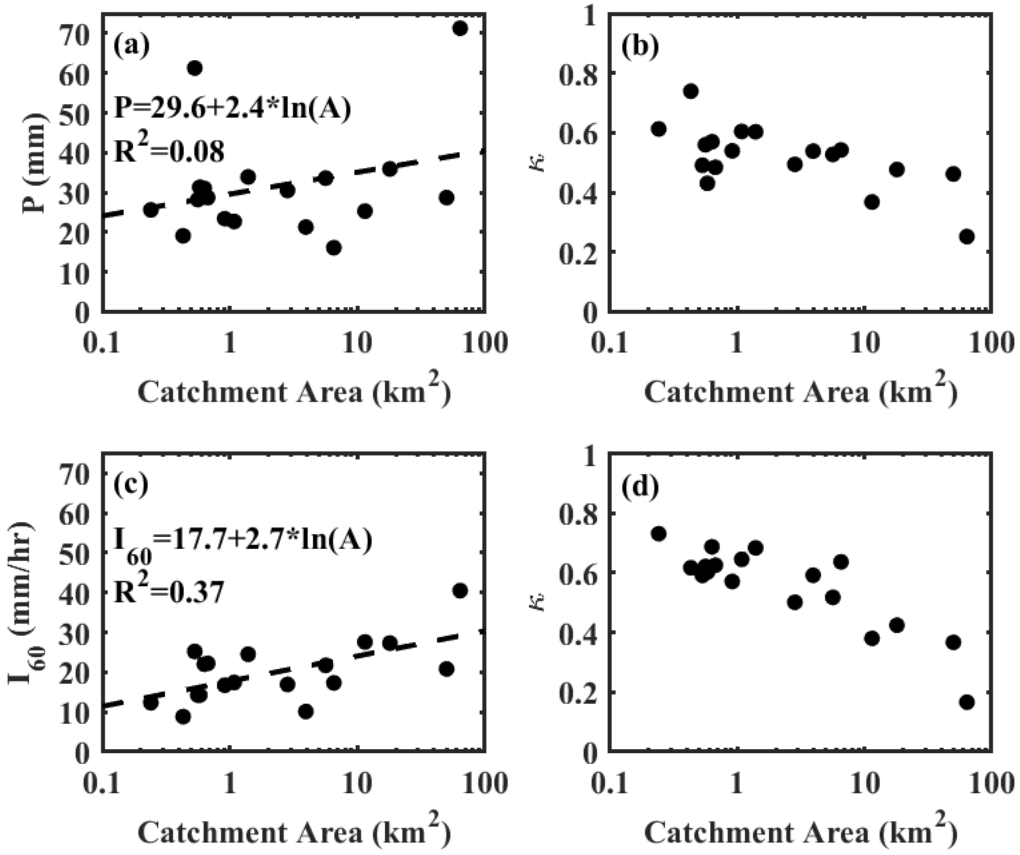

Figure 35. Scatterplots showing (a) event P thresholds versus playa catchment area, (b) kappa agreement statistics for P thresholds against catchment area, (c) event I_{60} thresholds versus catchment area, and (d) kappa agreement statistics for I_{60} thresholds against catchment area.

far from the playa and don't produce runoff cause the threshold for inundation to increase. To reduce the effect of partial storm coverage on thresholds for runoff generation, Kampf et al. (2018) utilized watershed mean rainfall intensity as opposed to the maximum pixel intensity and saw lower thresholds for watersheds over 1 km^2 and little correlation between mean intensity thresholds and catchment area. Applying this technique to playa inundation, mean I_{60} thresholds do not appear to be correlated with area as maximum I_{60} is, and calculating the mean had a much larger effect on larger

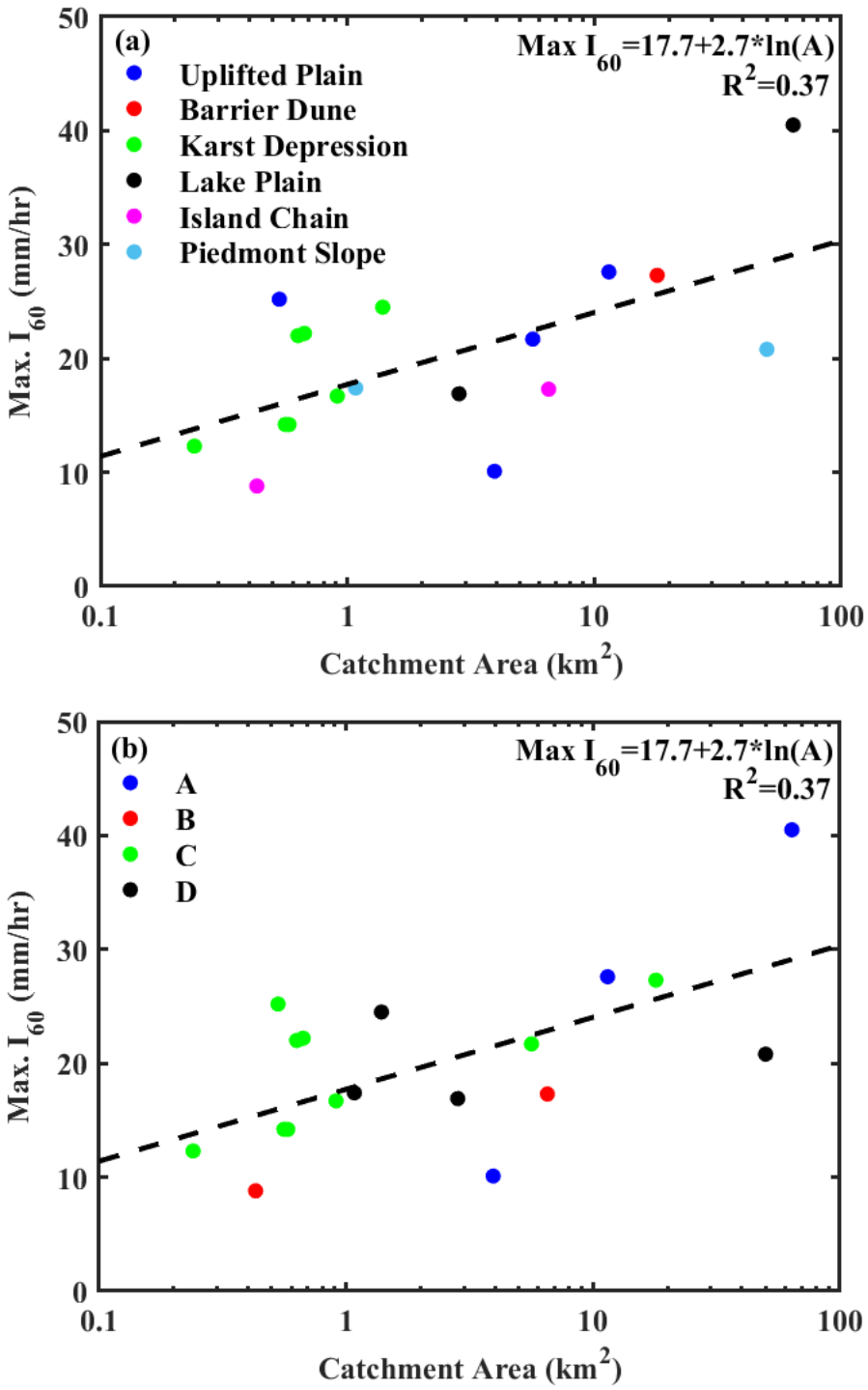

Figure 36. Scatterplots showing maximum I60 thresolds plotted against catchment area, colorred based on (a) playa grouping and (b) response type. For the response types, "A" represents long, deep events; "B" rapid, shallow, and frequent events; "C" rapid, deep events; and "D" rapid, shallow, and infrequent events.

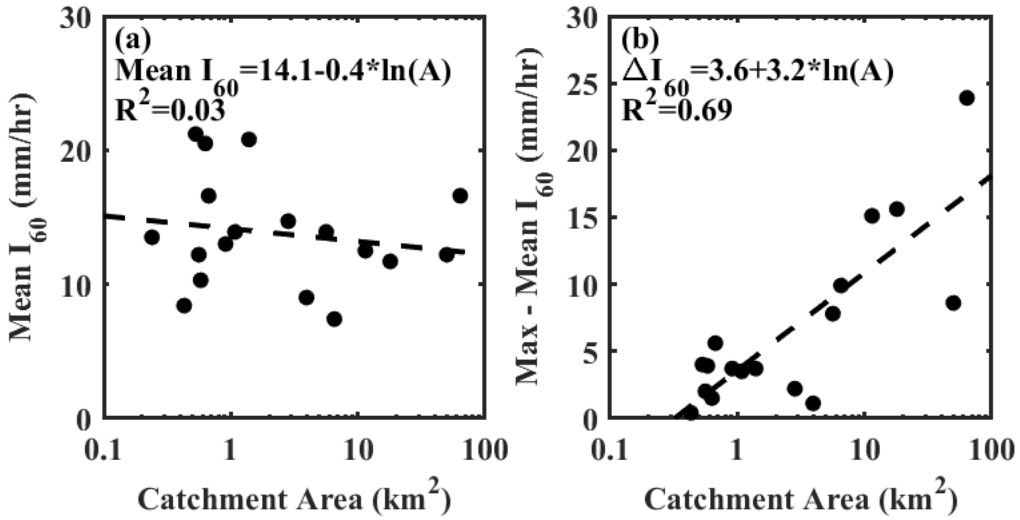

Figure 37. Scatterplots showing (a) mean I60 thresholds versus catchment area and (b) the difference between max and mean I60 thresholds versus catchment area.

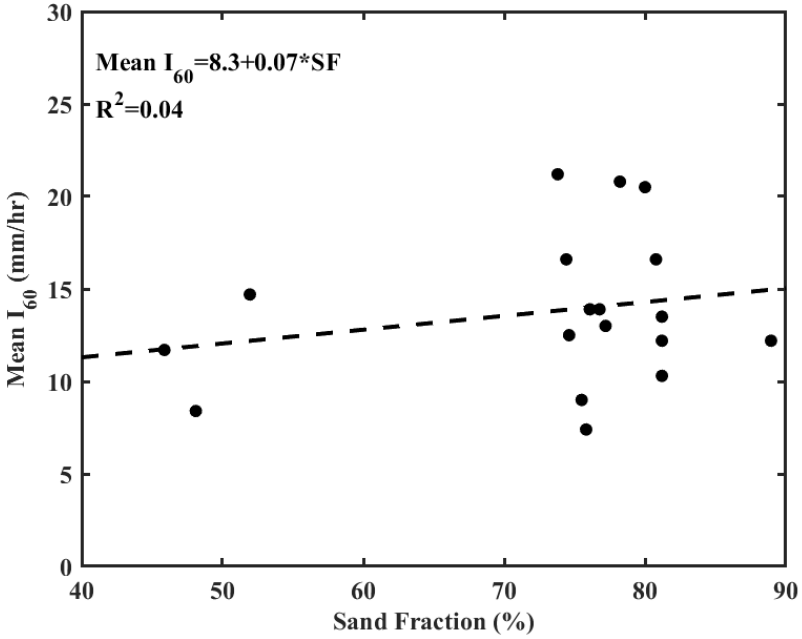

Figure 38. Mean I_{60} thresholds plotted against catchment sand fraction.

catchments (Figure 37). Since partial storm coverage is accounted for, perhaps the effect of channel transmission losses is more visible. A simple linear regression between mean I_{60} thresholds and sand fraction shown in Figure 38 reveals a slightly steeper positive correlation than with the maximum I_{60} thresholds, but the thresholds of catchments with

similar sand fractions are still somewhat spread out. This does not mean channel transmission losses do not play a role, however, since there could be other data or metrics that better represent it.

Application to Historical Data

The water level data from 2016-2022 allowed for new insights into how playas behave across the Jornada Basin. The understanding of rainfall-inundation relationships obtained through this analysis can be applied to the rich historical record at the JER and CDRRC to characterize how playas may have behaved in the past. Using a daily rainfall record from the JER headquarters for the 100 calendar years preceding the study period (January 1, 1916 - December 31, 2015), a calculation of estimated playa inundation volumes was performed, as well as an analysis of large rainfall events based on the thresholds obtained in the previous sections. Additionally, observations of flooding at Playa 7 from 1970-1989 can be taken advantage of to gauge the applicability of the thresholds to historical data and compare playa behavior between this period and the current period.

Analysis of Rainfall Record

The historical record analyzed in this study spans the 100 years prior to the beginning of the playa water level data. The daily timeseries is mostly complete and is shown in Figure 39. To place this rainfall record into the context of playa inundation, the daily rainfall thresholds determined above were applied to estimate the number of

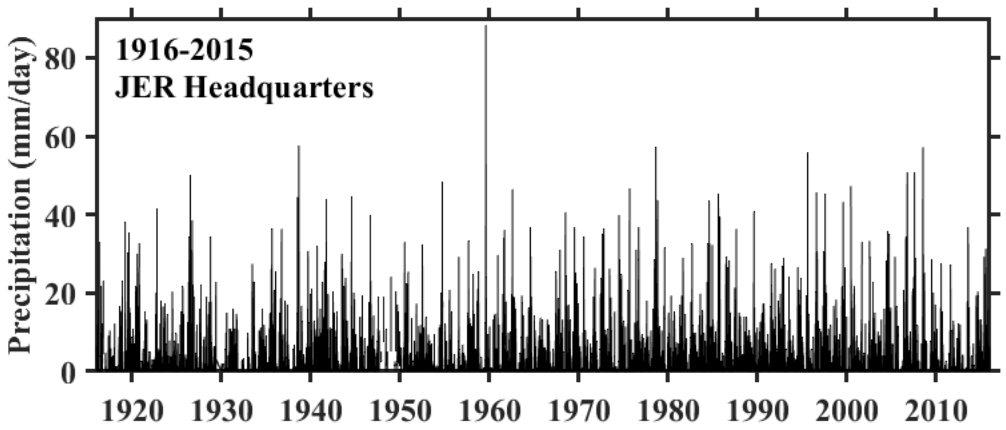

Figure 39. Daily precipitation timeseries of historical data at JER Headquarters from 1916-2015.

inundation-causing precipitation events that could have occurred at each playa. All threshold exceedances were assumed to cause inundation, and inundation volumes were calculated based on relationships between rainfall depth and inundation volume developed for the current study period. The results of this application are shown in Table 10. Threshold exceedances ranged from 9 to 391, and the mean annual inundation volumes ranged from about 550 to about 25,740 m^3. The mean annual inundation volumes determined for the period of 1916-2015 were slightly lower on average than those observed for the years of 2017-2021 (Figure 40). This suggests that the thresholds tend to underestimate the occurrence of playa inundation events, which is understandable considering they never have 100% accuracy. This could also be due to the poor linear fit between daily rainfall and inundation volume at some playas. A more process-based reason could be that the period of 2017-2021 simply saw more playa inundation than the average over the previous 100-year period.

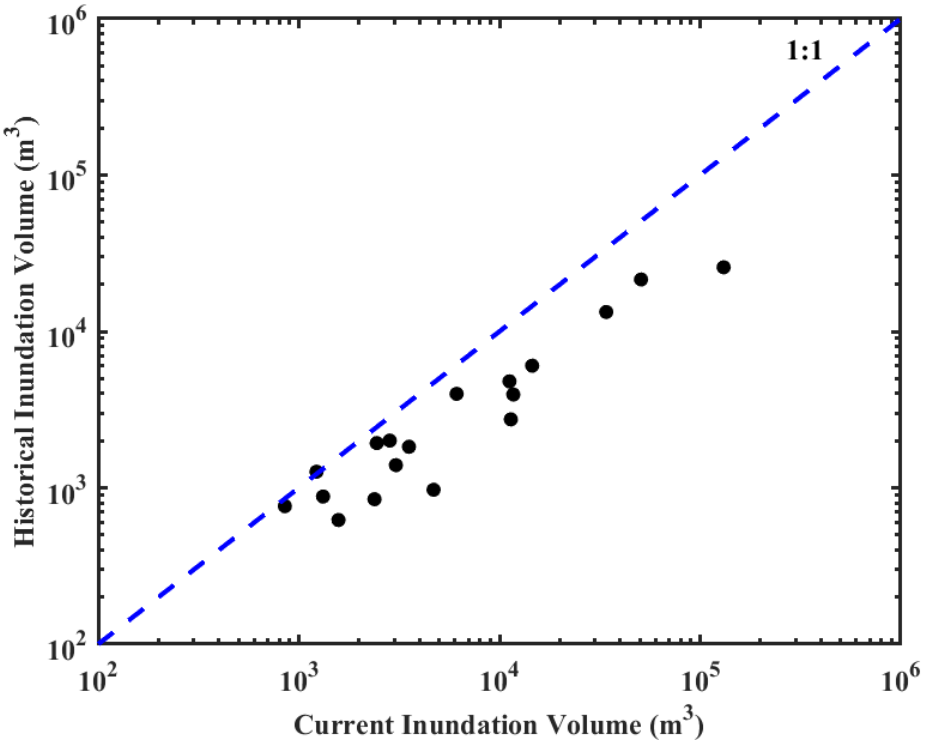

Figure 40. Comparison of the average annual inundation volumes at each playa for the historical period (1916-2015) and the current period (2016-2021).

The median daily rainfall threshold for playa inundation across the 18 playas was 22.7 mm. When applied to the daily rainfall record, there were 44 exceedances of this threshold over the 100-year period. A time series of the number or count of these events each year is shown in Figure 41. A Mann-Kendall test was performed to determine if there was a significant trend in the number of large events over this period. The test statistic S was calculated to be 776, indicating an increasing trend. The variance of the null distribution of S was calculated to be 106,131. Based on the value and variance of S, the z-value was calculated to be 2.38, which is statistically significant at the 5% level. Looking at the warm and cool seasons separately revealed an increasing trend in large events during the warm season (z=3.08, significant at the 1% level), while there was a

Table 10. Estimated playa inundation metrics for the historical period of 1916-2015.

Playa No.	Daily P Threshold [mm]	Number of Exceedances	Mean Annual Inundation Volume [10^3 m^3]	STD. Volume [10^3 m^3]
3	39.4	26	0.62	±1.20
5	33.0	56	3.95	±5.72
6	16.8	291	4.79	±4.45
7	48.2	9	2.74	±13.76
9	15.1	365	1.27	±0.94
11	33.0	56	25.73	±34.75
12	15.3	346	21.49	±15.76
14	15.2	365	6.04	±4.36
17	20.4	194	3.99	±3.61
18	22.3	164	0.88	±0.84
21	23.0	149	0.76	±0.73
22	14.5	391	2.00	±1.44
23	29.9	78	1.40	±1.77
24	18.9	240	1.83	±1.71
25	23.4	143	0.85	±0.86
28	29.9	78	1.93	±3.02
29	22.3	164	13.31	±12.66
30	34.9	43	0.97	±1.45

statistically insignificant decreasing trend in large events during the cool season ($z = -1.04$). This could mean that the warmer months are more susceptible to changes in climate and rainfall patterns than the cooler months in the historical period and perhaps in the future as well. To further characterize the rainfall trends, the Mann-Kendall test was also performed on the total annual precipitation and the number of days with nonzero

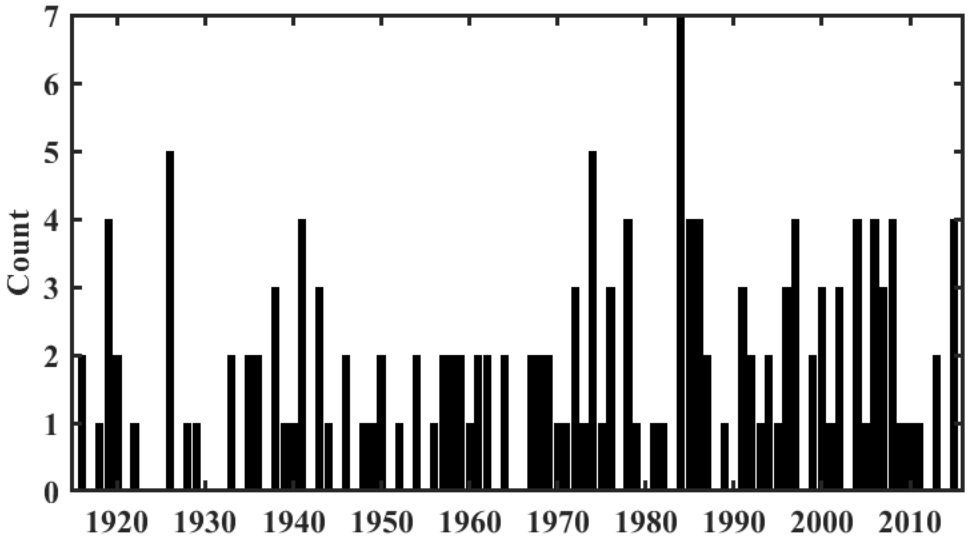

Figure 41. Number of days with greater than 22.7 mm of precipitation each year from 1916-2015.

precipitation each year. The results of these five tests are summarized in Table 11. Total annual precipitation shows an increasing trend that is significant only at the 10% level, and the number of days with nonzero precipitation shows a decreasing trend that is not statistically significant. Wainwright (2006) also observed an increasing trend in annual precipitation at the JER Headquarters gauge using data from 1914 to 1996 using a regression and autocorrelation analysis.

The increasing frequency of large rainfall events through the historical period suggests that playa inundation may have increased over this period. A similar trend in the frequency of large rainfall events has been predicted for the future as well and linked to climate change (Sun et al., 2007), meaning the frequency of playa inundation may also increase in the future (McKenna and Sala, 2018). Thus, changes in climate from 1916 to 2016 and in the future likely have impacted and will impact playa inundation dynamics.

Table 11. Results of Mann-Kendall tests for large rainfall events, annual precipitation, and the number of days with nonzero precipitation.

Test	S	Var(S)	z	Significance Level
Large Events	776	106,131	2.38	0.05
Large Events Warm Season	993	103,213	3.08	0.01
Large Events Cool Season	-269	66,811	-1.04	-
Annual Precipitation	587	116,150	1.72	0.1
Days with Precipitation	-33	115,948	-0.10	-

To adequately characterize the long-term trends in playa inundation, it is important to mention other factors that have changed in the Jornada Basin over the past century. The most notable and documented of these changes is that of woody plant encroachment (Figure 42). This phenomenon has converted grasslands into shrublands and has increased the amount of bare space on the ground through xerification (Schreiner-McGraw et al., 2020). While the direct effects of woody plant encroachment on playa grasslands have been limited to their periphery, an increase in bare space in playa catchments may have altered and may continue to alter the rainfall-runoff transformation that results in playa inundation (McAuliffe, 1994). Another change in the landscape is related to the aeolian transport of sand across the basin floor and up the piedmont slope. This has the effects of increased infiltration where sand is deposited (Okin et al., 2006) and the formation of mesquite coppice and vegetation-barrier dunes (Gillette and Monger, 2006; Weems and Monger, 2012). Weems and Monger (2012) used historical photographs to study the formation of vegetation-barrier dunes on the

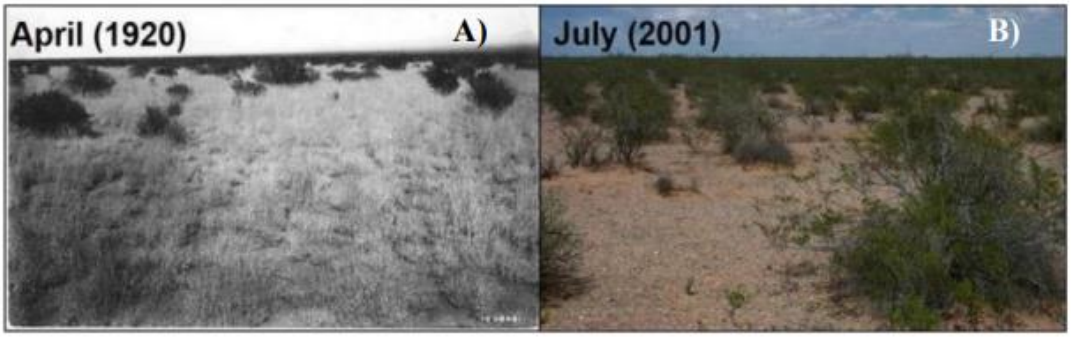

Figure 42. Historical photographs from the JER showing (A) robust grass cover in 1920 and (B) an increase in bare space and woody plants in 2001 (Jornada Basin LTER).

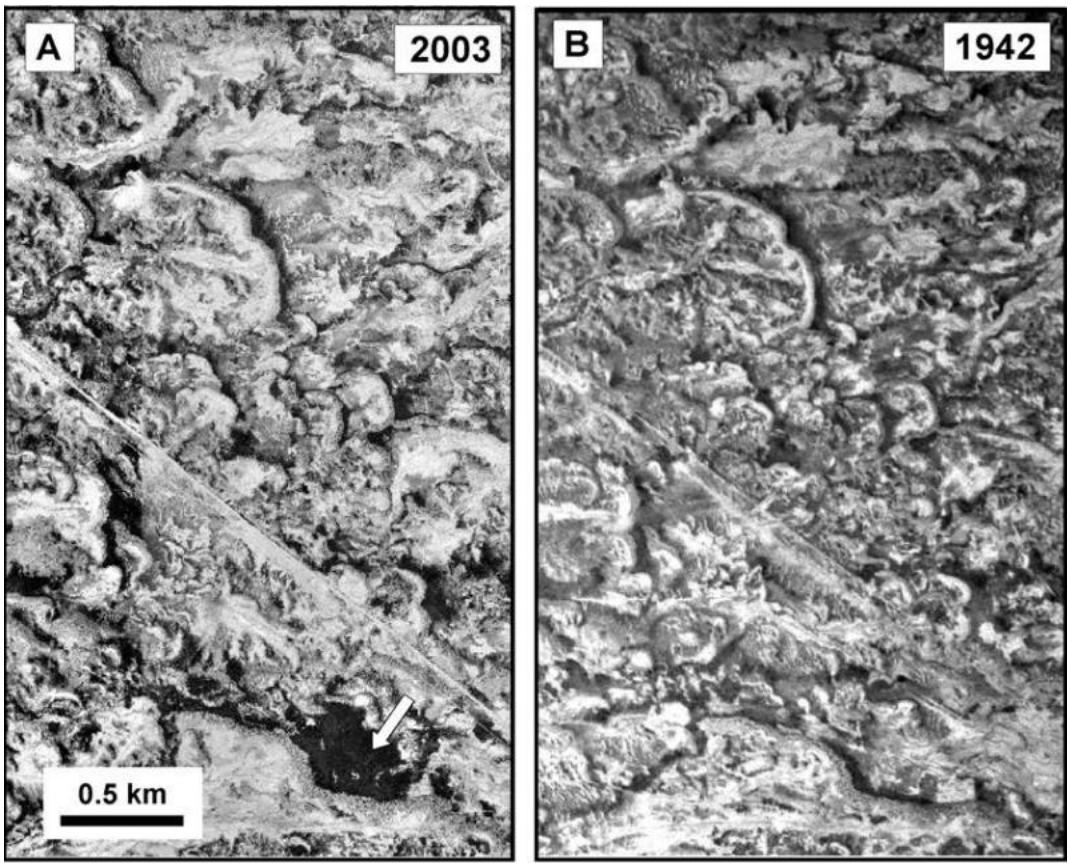

Figure 43. (A) Aerial photograph of a section of the eastern piedmont slope in 2003, with Playa 11 indicated by the white arrow. (B) Aerial photograph of the same location in 1942, before Playa 11 formed upslope of a banded-vegetation dune (from Weems and Monger, (2012).

eastern piedmont slope and noted that the feature known in this study as Playa 11 did not exist as late as 1942 (Figure 43). These dunes act as dams to water flow down the piedmont slope and over time have affected the landscape in such a way as to create new playas. It is crucial to remember that this is a continuously evolving basin that experiences changes in vegetation cover and sediment transport that interact with each other and can both compound and mitigate the hydrologic effects of the changing climate.

Historical Playa Observations

The rainfall thresholds for playa inundation were tested against historical observations of inundation documented in Van Vactor (1989). Van Vactor noted that from the years 1970 to 1989, there were 15 inundation events observed at College Playa, known in this study as Playa 7. Dates are known for 11 of these events, and the other 4 are only known by month and year, or just year. Using the daily rainfall threshold for Playa 7 of 48.2 mm, only one exceedance occurred during the period of 1970-1989 on August 20, 1978. There was no inundation observed at Playa 7 on this date, which is not that surprising since the rain gauge is located at the JER Headquarters. If the event-based threshold of 25.3 is applied to this period, there are 32 exceedances. Five of these exceedances occur within 1 day of an inundation event with a known date at Playa 7. This reveals that there are limitations when trying to identify dates of inundation and frequency of inundation through applying a single threshold to historical data from a single rain gauge.

Through his analysis, Van Vactor (1989) concluded that the Playa 7 can inundate with as little as 25 mm of rainfall if there is an intensity of 25 mm/hr for 30 minutes and

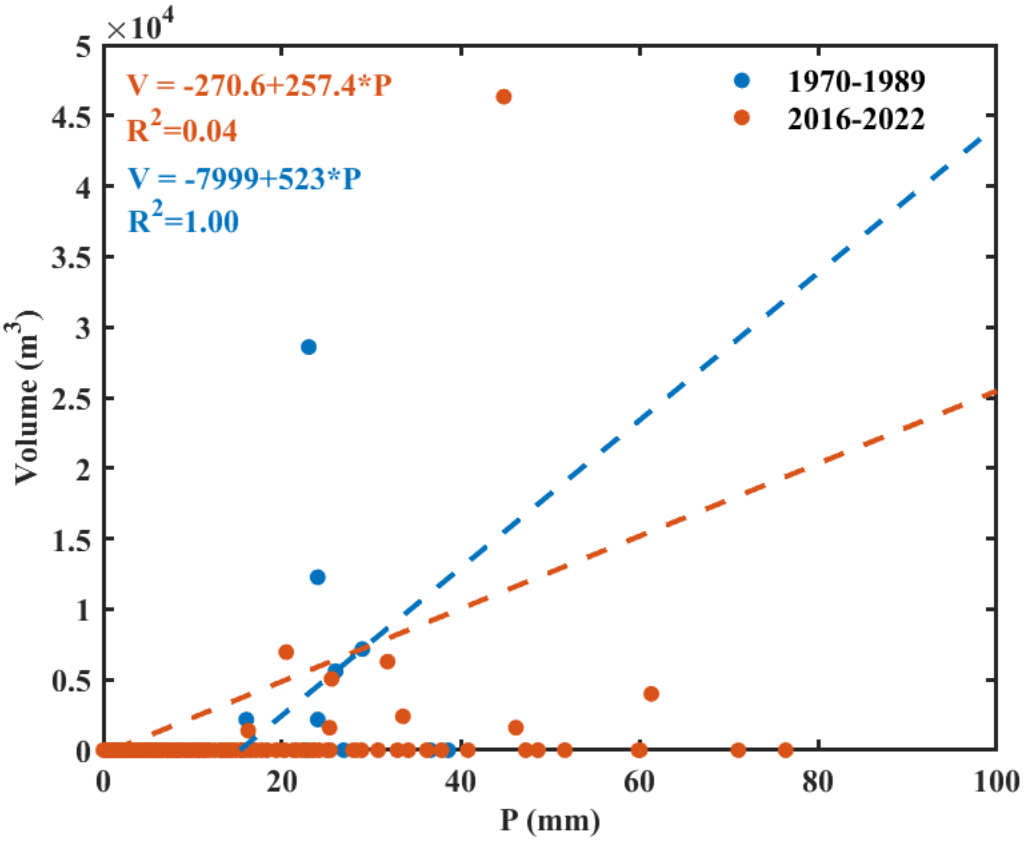

Figure 44. Inundation volume versus event precipitation at Playa 7 for events from 1970 1989 with known inundation volumes and events from 2016-2022 examined in this study.

the rainfall is centered at or near the playa itself. Although this is lower than the daily P threshold of 48.2 mm, it is much closer to the event-based threshold of 25.3 mm. The observations detailed in Van Vactor (1989) match up reasonably well with current data when events with known inundation volume are compared (Figure 44). The relationships between precipitation and inundation for inundation events over the 25 mm and 25.3 mm precipitation thresholds for the historical and current periods, respectively, are different, but this is likely due to a limited sample size. These comparisons suggest that the types of events that cause inundation at Playa 7 are similar in the current period as in 1970-1989. If the same types of rainfall events are inundating playas through time, the changing

climate will have a significant impact if the frequency of those events changes. If the frequency of large rainfall events increases and their intensity increases, this may lead to more runoff and therefore deeper, longer inundation events in the playas, assuming other factors stay the same. Thus, continued monitoring of the playas and their inundation dynamics will be critical as these changes occur.

CHAPTER 4

CONCLUSIONS AND FUTURE WORK

Summary

Playas are important features of dryland ecosystems as resilient grasslands and points of higher water availability. The reliance of most prior playa studies on remote sensing data or models to analyze playa function or the process of inundation has produced a need for studies using high-frequency, in-situ data. This study utilized novel datasets to characterize the hydrologic behavior of playas in the Chihuahuan Desert, with three main objectives: 1) Understand the conditions that cause playas to inundate, 2) Understand spatial controls on playa inundation, and 3) Compare current data with historical observations of rainfall and inundation to identify long-term trends.

This study focused on 18 playas located in the Jornada Basin, north of Las Cruces, New Mexico and instrumented with water level sensors. The playas have been instrumented since June 2016, and instantaneous measurements of surface water depth were recorded every 15 minutes over the study period of June 15, 2016 through October 31, 2022. These 18 playas are a subset of 30 that were studied and mapped by McKenna and Sala (2016). These 18 playas were placed into groupings based on the way they were formed and their geologic setting within the basin to help better explain their differences in behavior. The catchments for these playas were delineated in ArcMap using a LiDAR-derived 1 m resolution DEM and served as the key spatial reference for subsequent analyses. The MRMS quantitative precipitation estimation product was used for catchment precipitation metrics and was bias-corrected using a series of rain gauges

located across the study site. Properties like sand fraction and the percentage of bare ground were derived from publicly available products and averaged over each playa's catchment area. Remote sensing data from Planet CubeSats was used to visualize playa inundation from above and estimate inundated area as well as examine spatial patterns.

Preliminary observations on playa behaviors based on the inundation and rainfall data demonstrated that the two are correlated since there were no inundation events not associated with any rainfall. Inundation frequency generally followed seasonal trends in precipitation, with 76% of all inundation events occurring during the warm season. The data also allowed for the calculation of mean annual runoff ratios for the playa catchments, which ranged from 0.01% to 9.28%. The water level data revealed four main response types among the playas: (A) long, deep events, (B) rapid, shallow, relatively frequent events, (C) rapid, deep events, and (D) rapid, shallow, relatively infrequent events. Rainfall depth (P) and intensity (I_{60}) thresholds were determined for each playa by finding the threshold that maximized the kappa agreement statistic and ranged from 16.1 mm to 71.3 mm and 8.8 mm/hr to 40.5 mm/hr, respectively. It was clear that large, intense rainfall events were more likely to be associated with playa inundation. There were some notable exceptions to the thresholds that were found to be related to antecedent wetness of the playa from previous inundation events, low rainfall intensity despite high depth, and distance of the rainfall from the playa in larger catchments.

Playa behaviors and thresholds were also examined in a spatial context to better understand their variation. The inundation response types were observed to generally agree with the playa groupings established based on geology, with a few exceptions. Local factors such as the presence of roads and stock tanks at or near the playa were also

proposed as reasons for their different behaviors. A multiple logistic regression was used to characterize the relative importance of playa catchment variables for playa inundation. The results of the variable selection process and regression showed the significant role of catchment area and less significant role of catchment sand fraction. The thresholds for inundation also were influenced by catchment area, with larger catchments having larger thresholds for inundation. This was also observed in Kampf et al. (2018) and has been attributed to partial storm coverage and channel transmission losses. Other catchment properties, such as bare ground fraction, sand fraction, and slope, influenced the threshold to a lesser degree than catchment area. Mean intensity thresholds were also calculated and found to not be influenced by catchment area, which could allow for better insight into the influence of other factors.

Historical precipitation data from 1916 to 2016 was used to estimate historical playa inundation volumes and characterize long-term trends in large rainfall events as a proxy for how playa inundation may have changed over this period. Large events were identified based on the median daily rainfall threshold for playa inundation, and a Mann-Kendall test using the number of large events each year showed a significant increasing trend. This trend agrees with what has also been predicted for the future under climate change and suggests and increasing trend in playa inundation as a result of more frequent extreme rainfall events. Observations of inundation at one of the study playas, Playa 7, from 1970-1989 were also taken advantage of to see how inundation has changed between this historical period and the current period. Although the threshold exceedances didn’t exactly match up to the 15 inundations that were observed, the types of rainfall events causing inundation were found to be similar between the two periods.

Future Work

The observations and data analyses from this study advanced the understanding of how playas behave in the Jornada Basin, but there is still more that can be done. With the existing datasets, an analysis of the receding limbs of the playa hydrographs could be performed to quantify the water that infiltrates into the soil versus the water that evaporates. Maintaining a long-term record of playa inundation will be useful to increase the sample size of inundation events and see how playa inundation changes under changing future conditions. Additionally, improved or alternative catchment properties could be tested to see their effect on inundation, such as the vegetation in and immediately surrounding the playa that may significantly affect the runoff and infiltration processes. There is also more work that could be done related to using historical data to estimate playa inundation, such as looking at the effect of decadal variability in precipitation and the effects of factors like vegetation and soil texture, which have likely changed over the historical period.

Other instrumentation could complement the existing sensors nicely, such as a tipping bucket rain gauge at each playa as well as a profile of soil moisture sensors. This would allow for more reliable precipitation estimates at the playa, better characterization of antecedent moisture conditions, and monitoring of infiltration. The playa catchments would also benefit from more comprehensive instrumentation deployment, such as rain gauges, soil moisture sensors, and channel flumes or flow measurement devices. Rain gauges and soil moisture sensors would provide better precipitation estimates for the playa catchments and help characterize the role of antecedent moisture in the catchment. Channel flumes or other devices to measure runoff and streamflow would be a great

advancement by showing where runoff occurs and how frequently it occurs compared to playa inundation. This would provide data that could describe larger scale connectivity and in a larger catchment might help determine what parts of the catchment actually contribute runoff to the playa. Being able to exclude areas that seldom or never contribute runoff to the playa could allow for improved analysis of the role of other catchment properties, such as slope and vegetation.

Remote sensing of playas and stock tanks is another area that should continue to be developed in the future. Analyses and methods introduced in Wang and Vivoni (2022) and in this study have great potential for analyzing playa and stock tank inundation at a large scale where instrumentation is sparse. The high spatial and temporal resolution of PlanetScope imagery is a significant improvement over the products used in previous playa studies and allows for analysis of smaller playas and shorter inundation events. Thus, utilizing PlanetScope imagery improves understanding of playa systems and has implications for rangeland management.

REFERENCES

Adams, D. K., & Comrie, A. C. (1997). The North American Monsoon. Bulletin of the American Meteorological Society, 78(10), 2197–2213. https://doi.org/10.1175/1520-0477(1997)078%3C2197:TNAM%3E2.0.CO;2

Akaike, H. (1974). A new look at the statistical model identification. *IEEE Transactions on Automatic Control, 19*(6), 716-723. doi.org/10.1109/TAC.1974.1100705

Assouline, S. (2004). Rainfall-Induced Soil Surface Sealing: A Critical Review of Observations, Conceptual Models, and Solutions. *Vadose Zone Journal*, *3*, 570–591. https://doi.org/10.2136/vzj2004.0570

Bracken, L. J., & Croke, J. (2007). The concept of hydrological connectivity and its contribution to understanding runoff-dominated geomorphic systems. *Hydrological Processes*, *21*(13), 1749–1763. https://doi.org/10.1002/hyp.6313

Cayan, D. R., Das, T., Pierce, D. W., Barnett, T. P., Tyree, M., Gershunov, A., & Macdonald, G. M. (2010). Future dryness in the southwest US and the hydrology of the early 21st century drought. *PNAS*, *107*(50), 21271-21276. https://doi.org/10.1073/pnas.0912391107

Collins, S. D., Heintzman, L. J., Starr, S. M., Wright, C. K., Henebry, G. M., & McIntyre, N. E. (2014). Hydrological dynamics of temporary wetlands in the southern Great Plains as a function of surrounding land use. *Journal of Arid Environments*, *109*, 6–14. https://doi.org/10.1016/j.jaridenv.2014.05.006

Condie, K. C. (1982). Plate-tectonics model for Proterozoic continental accretion in the southwestern United States. *Geology*, *10*, 37–42. https://doi.org/10.1130/0091-7613(1982)10%3C37:PMFPCA%3E2.0.CO;2

Connell, S. D., Hawley, J. W., & Love, D. W. (2005). Late Cenozoic drainage development in the southeastern basin and range of New Mexico, southeasternmost Arizona, and western Texas. *New Mexico Museum of Natural History and Science Bulletin, 28*, 125-150. https://nmdigital.unm.edu/digital/collection/bulletins/id/485

Duniway, M. C., Herrick, J. E., & Monger, H. C. (2007). The High Water-Holding Capacity of Petrocalcic Horizons. *Soil Science Society of America Journal*, *71*(3), 812–819. https://doi.org/10.2136/sssaj2006.0267

Duniway, M. C., Herrick, J. E., & Monger, H. C. (2010). Spatial and temporal variability of plant-available water in calcium carbonate-cemented soils and consequences for arid ecosystem resilience. *Oecologia*, *163*(1), 215–226. https://doi.org/10.1007/s00442-009-1530-7

Evans, D. D., & Thames, J. L. (1981). *Water in Desert Ecosystems, US/IBP synthesis series no. 11* (D. D. Evans & J. L. Thames, Eds.). Dowden, Hutchinson, & Ross, Inc.

Gile, L. H., J. W. Hawley, and R. B. Grossman. 1981. Soils and geomorphology in the Basin and Range area of Southern New Mexico: Guidebook to the Desert Project (Memoir 39). New Mexico Bureau of Mines and Mineral Resources, Socorro, NM. https://geoinfo.nmt.edu/publications/monographs/memoirs/downloads/39/Memoir_39.pdf

Gillette, D. & Monger, H. C. (2006). Eolian Processes on the Jornada Basin. In K. M. Havstad, L. F. Huenneke, & W. H. Schlesinger (Eds.), *Structure and Function of Chihuahuan Desert Ecosystem: The Jornada Basin Long-Term Ecological Research Site* (pp. 189-210). Oxford University Press, New York.

Gitz, D., & Brauer, D. (2016). Trends in playa inundation and water storage in the Ogallala Aquifer on the Texas High plains. *Hydrology*, *3*(3). https://doi.org/10.3390/hydrology3030031

Goodrich, D. C., Lane, L. J., Shillito, R. M., Miller, S. N., Syed, K. H., & Woolhiser, D. A. (1997). Linearity of basin response as a function of scale in a semiarid watershed. *Water Resources Research*, *33*(12), 2951–2965. https://doi.org/10.1029/97WR01422

Hauser, V. L. (1966). *Hydrology, conservation, and management of runoff water in playas on the southern High Plains*. (Conservation Research Report No. 8). United States Department of Agriculture. https://ia903202.us.archive.org/15/items/hydrologyconserv08haus/hydrologyconserv08haus.pdf

Hawley, J. W., & Parsons, R. B. (1980). *Glossary of selected geomorphic and geologic terms*. West Technical Service Center, Soil Conservation Service. https://ia804605.us.archive.org/31/items/glossaryofselect00jwha/glossaryofselect00jwha.pdf

Huenneke, L. F., Anderson, J. P., Remmenga, M., & Schlesinger, W. H. (2002). Desertification alters patterns of aboveground net primary production in Chihuahuan ecosystems. *Global Change Biology*, *8*(3), 247–264. https://doi.org/10.1046/j.1365-2486.2002.00473.x

Huenneke, L. F., & Schlesinger, W.H. (2006). Patterns of Net Primary Production in Chihuahuan Desert Ecosystems. In K. M. Havstad, L. F. Huenneke, & W. H. Schlesinger (Eds.), *Structure and Function of Chihuahuan Desert Ecosystem: The Jornada Basin Long-Term Ecological Research Site* (pp. 232-246). Oxford University Press, New York.

Kambhammettu, B. P., Allena, P., & King, J. P. (2010). *Simulation of groundwater flow in the southern Jornada del Muerto Basin, Dõna Ana County, New Mexico*. (WRRI Technical Completion Report No. 352). New Mexico Water Resources Research Institute. https://nmwrri.nmsu.edu/wp-content/uploads/2015/technical-reports/tr352.pdf

Kampf, S. K., Faulconer, J., Shaw, J. R., Lefsky, M., Wagenbrenner, J. W., & Cooper, D. J. (2018). Rainfall Thresholds for Flow Generation in Desert Ephemeral Streams. *Water Resources Research*, *54*(12), 9935–9950. https://doi.org/10.1029/2018WR023714

Keller, Z. T. (2021). Runoff Connectivity, Controls, and Evolution During the North American Monsoon. [Masters Thesis] Arizona State University. https://hdl.handle.net/2286/R.2.N.168501

King, W. E., & Hawley, J. W. (1975). Geology and ground-water resources of the Las Cruces area, New Mexico. In W. R. Seager, R. E. Clemons, & J. F. Callender (Eds.), *New Mexico Geological Society 26th Annual Fall Field Conference Guidebook* (pp. 195–204).

Kirkby, M. J., Bracken, L. J., & Shannon, J. (2005). The influence of rainfall distribution and morphological factors on runoff delivery from dryland catchments in SE Spain. *Catena*, 62(2-3), 136–156. https://doi.org/10.1016/j.catena.2005.05.002

Li, Z., Yang, T., Xu, C. Y., Shi, P., Yong, B., Huang, C. sheng, & Wang, C. (2020). Evaluating the area and position accuracy of surface water paths obtained by flow direction algorithms. *Journal of Hydrology*, *583*. https://doi.org/10.1016/j.jhydrol.2020.124619

Loring, S. J., MacKay, W. P., & Whitford, W. G. (1988). Ecology of Small Desert Playas. In J. L. Thames & C. D. Ziebell (Eds.), *Small water impoundments in semi-arid regions* (pp. 89–113). University of New Mexico Press.

Magliano, P. N., Breshears, D. D., Murray, F., Niborski, M. J., Nosetto, M. D., Zou, C. B., & Jobbágy, E. G. (2022). South American Dry Chaco rangelands: Positive effects of cattle trampling and transit on ecohydrological functioning. *Ecological Applications* *33*(3), e2800. https://doi.org/10.1002/eap.2800

Mcauliffe, J. R. (1994). Landscape Evolution, Soil Formation, and Ecological Patterns and Processes in Sonoran Desert Bajadas. *Ecological Monographs*, *64*(2), 111-148. https://www.jstor.org/stable/2937038

McKenna, O. P., & Sala, O. E. (2016). Biophysical controls over concentration and depth distribution of soil organic carbon and nitrogen in desert playas. *Journal of Geophysical Research: Biogeosciences*, *121*(12), 3019–3029. https://doi.org/10.1002/2016JG003545

McKenna, O. P., & Sala, O. E. (2018). Groundwater recharge in desert playas: Current rates and future effects of climate change. *Environmental Research Letters*, *13*(1), 014025. https://doi.org/10.1088/1748-9326/aa9eb6

Michaud, J. D., Hirschboeck, K. K., & Winchell, M. (2001). Regional variations in small-basin floods in the United States. *Water Resources Research*, *37*(5), 1405–1416. https://doi.org/10.1029/2000WR900283

Monger, H. C. (2006). Soil development in the Jornada Basin. In K. M. Havstad, L. F. Huenneke, & W. H. Schlesinger (Eds.), *Structure and Function of Chihuahuan Desert Ecosystem: The Jornada Basin Long-Term Ecological Research Site* (pp. 81-106). Oxford University Press, New York.

Monger, H. C., Mack, G. H., Nolen, B. A., & Gile, L. H. (2006). Regional Setting of the Jornada Basin. In K. M. Havstad, L. F. Huenneke, & W. H. Schlesinger (Eds.), *Structure and Function of Chihuahuan Desert Ecosystem: The Jornada Basin Long-Term Ecological Research Site* (pp. 15-43). Oxford University Press, New York.

Motts, W. S. (1969). *Geology and hydrology of selected playas in Western United States*. (Report No. AFCRL-69-0214). Air Force Cambridge Research Laboratories. https://apps.dtic.mil/sti/pdfs/AD0709683.pdf

NHD. (2008). "National Hydrography Dataset." U.S. Geological Survey. http://nhd.usgs.gov/.

NOAA. (2023). Jornada Experimental Range Daily Summary, GHCND:USC00294426. National Oceanic and Atmospheric Administration. Retrieved May 25, 2023, from https://www.ncdc.noaa.gov/cdo-web/datasets/GHCND/stations/GHCND:USC00294426/detail

O'Callaghan, J. F., & Mark, D. M. (1984). The Extraction of Drainage Networks from Digital Elevation Data. *Computer Vision, Graphics, and Image Processing*, *28*, 323–344. https://doi.org/10.1016/S0734-189X(84)80011-0

Okin, G. S., Gillette, D. A., & Herrick, J. E. (2006). Multi-scale controls on and consequences of aeolian processes in landscape change in arid and semi-arid environments. *Journal of Arid Environments*, *65*(2), 253–275. https://doi.org/10.1016/J.JARIDENV.2005.06.029

Okin, G., Zhou, B., Duniway, M, Cole, C., Savage, S., Litschert, S., and Liddle, J. Landscape Cover Analysis and Reporting Tools V1.0. https://landcart.org. Published February 16, 2022. Accessed 29 May 2023.

Peters, D. P. C., & Gibbens, R. P. (2006). Plant Communities in the Jornada Basin: The Dynamic Landscape. In K. M. Havstad, L. F. Huenneke, & W. H. Schlesinger (Eds.), *Structure and Function of Chihuahuan Desert Ecosystem: The Jornada Basin Long-Term Ecological Research Site* (pp. 211–231). Oxford University Press, New York.

Peters, D. P. C. (2013). Appendix 1: Jornada (JRN) (USDA-ARS, LTER). In D. P. C. Peters, C. M. Laney, A. E. Lugo, S. L. Collins, C. T. Driscoll, P. M. Groffman, J. M. Grove, A. K. Knapp, T. Kratz, M. D. Ohman, R. B. Waide, and J. Yao, (Eds.), *Long-term trends in ecological systems: a basis for understanding responses to global change*. (pp. 269-272). United States Department of Agriculture (USDA), Washington, D.C., USA.

Peters, D. P. C., Savoy, H. M., Stillman, S., Huang, H., Hudson, A. R., Sala, O. E., & Vivoni, E. R. (2021). Plant species richness in multiyear wet and dry periods in the chihuahuan desert. *Climate*, *9*(8), 130. https://doi.org/10.3390/cli9080130

Peterson, F. F. (1981). *Landforms of the basin and range province defined for soil survey*. (Technical Bulletin 28). Nevada Agricultural Experiment Station. https://www.ars.usda.gov/ARSUserFiles/30501000/esd/pubs/Peterson_LandformsBasinRangeProvince.pdf

Planet Labs. (2023). *PSOrthoTile*. Retrieved from https://developers.planet.com/docs/data/psorthotile/.

Rachal, D. M., Monger, H. C., Okin, G. S., & Peters, D. C. (2012). Landform influences on the resistance of grasslands to shrub encroachment, northern Chihuahuan desert, USA. *Journal of Maps*, *8*(4), 507–513. https://doi.org/10.1080/17445647.2012.727593

Ramos-Scharrón, C. E., & LaFevor, M. C. (2018). Effects of Forest Roads on Runoff Initiation in Low-Order Ephemeral Streams. *Water Resources Research*, *54*(11), 8613–8631. https://doi.org/10.1029/2018WR023442

Rango, A., Tartowski, S. L., Laliberte, A., Wainwright, J., & Parsons, A. (2006). Islands of hydrologically enhanced biotic productivity in natural and managed arid ecosystems. *Journal of Arid Environments*, *65*(2), 235–252. https://doi.org/10.1016/j.jaridenv.2005.09.002

Reeves, C. C. (1970). Origin, Classification, and Geologic History of Caliche on the Southern High Plains, Texas and Eastern New Mexico. The Journal of Geology, 78(3), 352–362. https://doi.org/10.1086/627521

Richardson, L. G. (1971). A sampling study of the macroinvertebrate ecology of a desert playa lake in southwestern New Mexico. [Masters Thesis]. Texas Tech University.

Rosen, M. R. 1994. Paleoclimate and basin evolution of playa systems. *Geological Society of America Special Papers*, *289*, 1-18. https://doi.org/10.1130/SPE289

Russell, M. T., Cartwright, J. M., Collins, G. H., Long, R. A., & Eitel, J. H. (2020). Legacy Effects of Hydrologic Alteration in Playa Wetland Responses to Droughts. *Wetlands*, *40*(6), 2011–2024. https://doi.org/10.1007/s13157-020-01334-0

Schlesinger, W. H., Reynolds, J. F., Cunningham, G. L., Huenneke, L. F., Jarrell, W. M., Virginia, R. A., & Whitford, W. G. (1990). Biological feedbacks in global desertification. *Science*, *247*(4946), 1043–1048. https://doi.org/10.1126/science.247.4946.1043

Schlesinger, W. H., Abrahams, A. D., Parsons, A. J., & Wainwright, J. (1999). Nutrient Losses in Runoff from Grassland and Shrubland Habitats in Southern New Mexico: I. Rainfall Simulation Experiments. Biogeochemistry, 45(1), 21–34. https://doi.org/10.1007/BF00992871

Schreiner-McGraw, A. P., & Vivoni, E. R. (2017). Percolation observations in an arid piedmont watershed and linkages to historical conditions in the Chihuahuan Desert. *Ecosphere*, *8*(11), e02000. https://doi.org/10.1002/ecs2.2000

Schreiner-McGraw, A. P., Vivoni, E. R., Ajami, H., Sala, O. E., Throop, H. L., & Peters, D. P. C. (2020). Woody Plant Encroachment has a Larger Impact than Climate Change on Dryland Water Budgets. *Scientific Reports*, *10*(1), 8112. https://doi.org/10.1038/s41598-020-65094-x

Seager, W. R. (1975). Cenozoic tectonic evolution of the Las Cruces area, New Mexico. *26th Annual Field Conference Guidebook*, 241–250. https://doi.org/10.56577/FFC-26.241

Seager, W. (1981). *Geology of organ mountains and southern San Andres mountains, New Mexico*. (Memoir 36). New Mexico Bureau of Mines and Mineral Resources. https://geoinfo.nmt.edu/publications/monographs/memoirs/downloads/36/Memoir-36.pdf

Serrano-Notivoli, R., Martínez-Salvador, A., García-Lorenzo, R., Espín-Sánchez, D., & Conesa-García, C. (2022). Rainfall-runoff relationships at event scale in western Mediterranean ephemeral streams. *Hydrology and Earth System Sciences*, *26*(5), 1243–1260. https://doi.org/10.5194/hess-26-1243-2022

Shaw, P. A., and R. G. Bryant. 2011. Pans, playas and salt lakes. In D. S. G. Thomas, editor. *Arid zone geomorphology: process, form, and change in drylands* (pp. 293-317). Wiley, Chichester, UK. https://doi.org/10.1002/9780470710777.ch15

Simanton, J. R., & Osborn, H. B. (1983). Runoff estimates for thunderstorm rainfall on small rangeland watersheds. In *Hydrology and Water Resources in Arizona and the Southwest* (Vol. 13, pp. 9–15). Flagstaff, AZ: Arizona-Nevada Academy of Science. http://hdl.handle.net/10150/296083

Snyder, K. A., Mitchell, K. A., & Herrick, J. E. (2006). Patterns and Controls of Soil Water in the Jornada Basin. In K. M. Havstad, L. F. Huenneke, & W. H. Schlesinger (Eds.), *Structure and Function of Chihuahuan Desert Ecosystem: The Jornada Basin Long-Term Ecological Research Site* (pp. 107-132). Oxford University Press, New York.

Soil Survey Staff. (2022). Gridded National Soil Survey Geographic (gNATSGO) Database for Arizona [Database]. United States Department of Agriculture, Natural Resources Conservation Service. https://nrcs.app.box.com/v/soils

Solvik, K., Bartuszevige, A. M., Bogaerts, M., & Joseph, M. B. (2021). Predicting Playa Inundation Using a Long Short-Term Memory Neural Network. *Water Resources Research*, *57*(12), e2020WR029009. https://doi.org/10.1029/2020WR029009

Starr, S. M., & McIntyre, N. E. (2020). Land-cover changes and influences on playa wetland inundation on the Southern High Plains. *Journal of Arid Environments*, *175*, 104096. https://doi.org/10.1016/j.jaridenv.2019.104096

Sun, Y., Solomon, S., Dai, A., & Portmann, R. W. (2007). How often will it rain? *Journal of Climate*, *20*, 4801–4818. https://doi.org/10.1175/JCLI4263.1

USEPA (U.S. Environmental Protection Agency). (2015). *Connectivity of Streams and Wetlands to Downstream Waters: A Review and Synthesis of the Scientific Evidence*. http://cfpub.epa.gov/ncea/cfm/recordisplay.cfm?deid=296414

Van Vactor, S. S. (1989). Hydrologic and Edaphic Patterns and Processes Leading to Playa Flooding. [Masters Thesis]. New Mexico State University.

Viera, A. J., & Garrett, J. M. (2005). Understanding the Interobserver Agreement: The Kappa Statistic. *Family Medicine*, *37*(5), 360–363. https://pubmed.ncbi.nlm.nih.gov/15883903/

Vivoni, E. R., Pérez-Ruiz, E. R., Keller, Z. T., Escoto, E. A., Templeton, R. C., Templeton, N. P., Anderson, C. A., Schreiner-McGraw, A. P., Méndez-Barroso, L. A., Robles-Morua, A., Scott, R. L., Archer, S. R., & Peters, D. P. C. (2021). Long-term research catchments to investigate shrub encroachment in the Sonoran and Chihuahuan deserts: Santa Rita and Jornada experimental ranges. *Hydrological Processes*, *35*(2), e14031. https://doi.org/10.1002/hyp.14031

Wainwright, J. (2006). Climate and Climatological Variations in the Jornada Basin. In K. M. Havstad, L. F. Huenneke, & W. H. Schlesinger (Eds.), *Structure and Function of Chihuahuan Desert Ecosystem: The Jornada Basin Long-Term Ecological Research Site* (pp. 44-80). Oxford University Press, New York.

Wang, Z., & Vivoni, E. R. (2022). Detecting Streamflow in Dryland Rivers Using CubeSats. *Geophysical Research Letters*, *49*(15), e2022GL098729. https://doi.org/10.1029/2022GL098729

Weems, S. L., & Monger, H. C. (2012). Banded vegetation-dune development during the Medieval Warm Period and 20th century, Chihuahuan Desert, New Mexico, USA. *Ecosphere*, *3*(3), 21. https://doi.org/10.1890/es11-00194.1

Wondzell, S. M., Cornelius, J. M., & Cunningham, G. L. (1990). Vegetation Patterns, Microtopography, and Soils on a Chihuahuan Desert Playa. *Journal of Vegetation Science, 1*(3), 403-410. https://doi.org/10.2307/3235717

Yoo, C., Park, C., Yoon, J., & Kim, J. (2014). Interpretation of mean-field bias correction of radar rain rate using the concept of linear regression. *Hydrological Processes, 28*(19), 5081–5092. https://doi.org/10.1002/hyp.9972

Zhang, J., Howard, K., Langston, C., Kaney, B., Qi, Y., Tang, L., Grams, H., Wang, Y., Cockcks, S., Martinaitis, S., Arthur, A., Cooper, K., Brogden, J., & Kitzmillller, D. (2016). Multi-Radar Multi-Sensor (MRMS) quantitative precipitation estimation: Initial operating capabilities. *Bulletin of the American Meteorological Society*, *97*(4), 621–638. https://doi.org/10.1175/BAMS-D-14-00174.1

APPENDIX A

WATER LEVEL DATASETS

This appendix describes the water level datasets used in this thesis that are located in the shared Dropbox folder "KIMSAL_DIGITAL_APPENDIX" (https://www.dropbox.com/sh/ng5i08psqnr5yih/AADC9SfuTpGhKeR5aVJx5IX_a?dl=0) in the subfolder "APPENDIX A," which can be accessed through the following link: https://www.dropbox.com/sh/bs1kmk32wfrveqs/AAAPRnIk0aJ4pS1tptXe3uzaa?dl=0.

Within this folder are two subfolders: "playa_waterlevel" and "stocktank_waterlevel." The "playa_waterlevel" folder contains the water level data for the 18 instrumented playas included in this study, and the "stocktank_waterlevel" folder contains the water level data for the 5 instrumented stock tanks, which were not analyzed in this study. Within the "playa_waterlevel" folder, there are five subfolders: "HOBO_files," "CSVs," "mat_files," "event_info," and "QA_QC." The "HOBO_files" folder contains the original *.hobo files downloaded from the water level and temperature/RH dataloggers, and the data are organized into folders based on date and playa. The data are offloaded every March, June, and November, so the raw files correspond to these collection periods. The data have a 15-minute resolution and are available for the period of June 15, 2016 onward, with some gaps that are described below.

The "CSVs" folder contains the raw, original CSV files exported from the HOBOware Pro software organized by playa and year for the water level and temperature/RH data. The "CSVs" folder also contains the Level 0, Level 1, and Level 2 playa water level data that correspond to the QA/QC steps that are described below.

The “mat_files” folder contains *.mat files of the Level 2 water level data for each playa. The “QA_QC” folder contains the MATLAB scripts used to perform each step of the QA/QC, as well as a document that explains the workflow that was followed.

The “event_info” folder contains *.mat files that are MATLAB structures with the information for playa inundation events, including start and end times, durations, maximum water levels, and the time of the maximum water level.

There are two Word documents in the “playa_waterlevel” folder. One of these describes how to process the *.hobo files using the HOBOware software and export *.csv files. The other one explains the installation of the sensors and first data downloads.

The QA/QC process helps eliminate erroneous readings and makes the playa water level data more usable. The first step in this process is to create Level 0 CSVs from the raw CSVs exported from HOBOware. This involves adopting standard column names (‘site’, ‘timestamp’, ‘absolutePressure_kPa’, ‘temp_C’, and ‘waterLevel_m’) and keeping only these columns. Going from Level 0 to Level 1 involves flagging the data as either Invalid (I), Questionable (Q), or Flood (F) and adding ‘qflag’ and ‘comment’ columns. One way to flag the data is to flag all values over a certain threshold. This threshold can vary by playa and by collection period due to fluctuations in background noise. The automatically assigned flags can then be inspected manually, which is quite manageable if only one collection period is being quality controlled. It is very useful to compare the water level data to rainfall data to identify whether an inundation event actually occurred. Some common false inundations are around the time of data collection or related to high background noise. Inundation events that were not initially flagged

should be checked for as well. Inundations are usually easy to identify visually based on their sharp rise in water level, as opposed to background noise that is often more gradual and not correlated with rainfall. Going from Level 1 to Level 2 consists of taking only the flood values from the Level 1 CSV. For this thesis, both Q and F flags were included in Level 2, since many of the questionable events appeared more likely than not to be inundation. Temperature and relative humidity data has not yet been quality controlled.

It should be noted that all playas are missing data for the November 2020 – March 2021 collection period, and Playa 3 is also missing data for the June 2020 – November 2021 period. Also the data for the June – November 2021 period has incorrect timestamps in the *.hobo files that were corrected in the CSVs based on the collection times. More specific details on the missing data and the November 2021 collection times are included in *.txt files in the “playa_waterlevel” folder.

Within the “stocktank_waterlevel” folder are the stock tank water depths, which are available from January 2018 through December 2022 and have a 5-minute resolution. The data from the tipping bucket rain gauges located at each tank is also provided.

APPENDIX B

GIS DATASETS

This appendix describes the geospatial data used in this thesis, which are that are located in the shared Dropbox folder "KIMSAL_DIGITAL_APPENDIX" in the subfolder "APPENDIX_B," which can be accessed through the following link: https://www.dropbox.com/sh/i6c1krx06qyn3q9/AACcG59nPQT-hP4pUY1ABTHla?dl=0.

Note that all GIS data used for this work is in the UTM Zone 13N, WGS 1984 coordinate system. Within the "APPENDIX_B" folder, there are several subfolders that contain different GIS data. The folder "playa_polygons" contains the shapefiles for the 18 instrument playas, as well as the complete set of 30, the boundaries of which were surveyed by Owen McKenna (McKenna and Sala, 2016). These boundaries were determined mostly based on vegetation, with the assumption that there were no mesquite shrubs in the playas. This folder also contains a shapefile of the JER landform map, the playas and playettes from the landform map, and the playa groupings developed for this thesis. The folder called "stocktank_polygons" contains a shapefile of all the dirt stock tanks in the JER, as well as a shapefile for the instrumented stock tanks only.

The "playa_catchments" folder contains shapefiles for the 30 playa catchments delineated using the 1 m LiDAR DEM, as well as the 5 instrumented stock tanks. The catchments delineated by Owen McKenna based on 5 and 10 m resolution DEMs are also included in this folder.

The LiDAR folder contains the 1 m resolution LiDAR-derived DEM for the study area. This was received in two pieces, so there are multiple DEM files in a folder titled "jer_dem_full." The original DEM was sent in the UTM Zone 13N, North American

1983 datum coordinate system, so it was reprojected to UTM Zone 13N WGS 1984. Both of these files are stored here, and they cover an approximately 50 km x 50 km area over the JER and CDRRC. An extension was needed to cover the northern-most edge of Playa 28's catchment, which is saved in the "extension" folder. This piece should be used with caution, since it only has integer elevation values. The original and the extension were also mosaicked together, but the resulting file also has only integer elevation values. More details are found in the readme.txt files located in these folders. Also located in the LiDAR folder are the hillshade derived from the DEM, DEMs clipped to the playa catchments and buffer areas around the playas, and catchment slope rasters.

The folder titled "rain_gauges" contains the locations of all 69 rain gauges used for the bias correction. The folder titled "MRMS_grids" contains a MATLAB structure called 'MRMS_all_struct2.mat' that contains the dates and 60 x 50 cell grid for all hours that were downloaded, as well as the spatial reference information. It also contains a structure with the hourly corrected grids for the study period and *.mat files with the hourly, daily, and monthly correction factors that were used. There is also a shapefile of the blank MRMS grid located in this folder that was used to derive the pixels that rain gauges were located in and create figures. The derived rainfall metrics and rainfall event data for each playa catchment are also included in this folder.

The folder called "Jornada" contains the shapefiles and rasters that characterize and define the study area, such as the bare ground data, the sand fraction data, the JER and CDRRC boundaries, and the Chihuahuan Desert boundary.

APPENDIX C

RAIN GAUGE NETWORK

This appendix describes the information about the tipping bucket rain gauges and their data used in this thesis. The gauge information and rainfall data are stored in the shared Dropbox folder "KIMSAL_DIGITAL_APPENDIX" in the subfolder "APPENDIX_C," which can be accessed through the following link: https://www.dropbox.com/sh/o8qxwhgb9210676/AADL0gR1y0QmyNI6O5EaclQxa?dl=0.

This folder contains the data for each individual gauge as *.mat files as well as *.csv. Note that the CSV data for the automated gauges are located in three files that contain data for all the gauges, with the measurements in inches. The *.mat files contain the rainfall depths in millimeters. This folder also contains an Excel version of the table presented below.

Table C.1 below contains information about the tipping bucket rain gauges, including their name, the network they are part of, their elevation based on the LiDAR-derived DEM, and their period of data availability. Northing and easting in the UTM Zone 13N, WGS 1984 coordinate system is provided in the Excel version of this table, as well as the model number of each gauge. Multiple rows of data availability dates are present for gauges where data some data was removed. Note that missing data were not addressed since the gauge values of 0 were not included in the bias correction. The data availability is based on the life of the rain gauge and data that were removed at some gauges during the quality control procedure. Data from the JER automated rain gauge network were quality controlled by comparing monthly values to the nearest Jornada monthly rain gauge, since the tipping bucket gauges have been known to have some

issues. This resulted in several months or years being removed from these data before use in this thesis, and the data from these gauges should be used with caution.

Table C.1 Information for tipping bucket rain gauges used for bias correction of MRMS radar rainfall data.

Gauge Name	Gauge Network	Elevation (m)	Temporal Resolution	Start of Data	End of Data
Block 2	CSIS	1318.1	1 second	8/10/2017	10/31/2022
Block 3	CSIS	1327.8	1 second	8/11/2017	10/31/2022
Block 4	CSIS	1325.8	1 second	8/11/2017	10/31/2022
Block 5	CSIS	1329.0	1 second	8/11/2017	10/31/2022
Block 6	CSIS	1328.5	1 second	6/15/2016	10/31/2022
Block 7	CSIS	1324.9	1 second	8/11/2017	10/31/2022
Block 8	CSIS	1324.1	1 second	8/11/2017	10/31/2022
Block 9	CSIS	1325.5	1 second	8/11/2017	10/31/2022
Block 10	CSIS	1326.1	1 second	8/11/2017	10/31/2022
Block 11	CSIS	1325.7	1 second	8/11/2017	10/31/2022
Block 13	CSIS	1325.5	1 second	8/11/2017	10/31/2022
Block 14	CSIS	1326.4	1 second	8/11/2017	10/31/2022
Block 15	CSIS	1323.2	1 second	8/11/2017	10/31/2022
C-CALI	NPP	1371.3	1 second	6/15/2016	10/31/2022
C-GRAV	NPP	1376.4	1 second	6/15/2016	10/31/2022
C-SAND	NPP	1354.3	1 second	6/15/2016	10/31/2022
G-BASN	NPP	1316.9	1 second	6/15/2016	10/31/2022
G-IBPE	NPP	1324.4	1 second	6/15/2016	10/31/2022
G-SUMM	NPP	1386.9	1 second	6/15/2016	10/31/2022
M-NORT	NPP	1328.3	1 second	6/15/2016	10/31/2022
M-RABB	NPP	1325.1	1 second	6/15/2016	10/31/2022

Gauge Name	Gauge Network	Elevation (m)	Temporal Resolution	Start of Data	End of Data
M-WELL	NPP	1323.7	1 second	6/15/2016	10/31/2022
P-COLL	NPP	1313.2	1 second	6/15/2016	10/31/2022
P-SMAL	NPP	1322.5	1 second	3/28/2017	10/31/2022
P-TOBO	NPP	1314.5	1 second	6/15/2016	10/31/2022
T-EAST	NPP	1314.1	1 second	6/15/2016	10/31/2022
T-TAYL	NPP	1318.9	1 second	6/15/2016	10/31/2022
T-WEST	NPP	1314.3	1 second	6/15/2016	10/31/2022
3in Dikes	JER Automated	1338.0	1 minute	1/1/2019	12/31/2019
Antelope	JER Automated	1333.2	1 minute	6/15/2016	7/31/2018
				1/1/2019	12/31/2020
				4/1/2022	10/31/2022
Aristida	JER Automated	1331.9	1 minute	1/1/2019	12/31/2020
Brown Tank	JER Automated	1358.2	1 minute	1/1/2019	10/31/2022
Co-Op Well	JER Automated	1330.0	1 minute	1/1/2019	10/31/2022
Cross Tank	JER Automated	1394.1	1 minute	1/1/2018	10/31/2022
Dona Ana	JER Automated	1330.2	1 minute	6/15/2016	12/31/2020
Garcia Well	JER Automated	1413.8	1 minute	6/15/2016	12/31/2017
				1/1/2019	10/31/2022
Headquarters	JER Automated	1314.6	1 minute	6/15/2016	10/31/2022
IBP	JER Automated	1325.1	1 minute	1/1/2017	12/31/2021
Mesquite	JER Automated	1320.5	1 minute	1/1/2017	12/31/2017
				1/1/2021	12/31/2021
Middle Well	JER Automated	1316.6	1 minute	1/1/2018	10/31/2022
Nelson Tank	JER Automated	1313.6	1 minute	6/15/2016	9/30/2017
				1/1/2019	12/31/2020
New Well	JER Automated	1486.6	1 minute	1/1/2017	10/31/2022
Northeast	JER Automated	1318.5	1 minute	1/1/2018	10/31/2022

Gauge Name	Gauge Network	Elevation (m)	Temporal Resolution	Start of Data	End of Data
Parker Tank	JER Automated	1446.9	1 minute	1/1/2019	10/31/2022
Pasture 2	JER Automated	1329.0	1 minute	6/15/2016	12/31/2017
				1/1/2020	10/31/2022
Pasture 13	JER Automated	1323.0	1 minute	6/15/2016	12/31/2017
				1/1/2019	10/31/2022
Perm Exc 1	JER Automated	1332.9	1 minute	1/1/2018	12/31/2020
Perm Exc 6	JER Automated	1336.7	1 minute	1/1/2019	12/31/2020
Puddle Tank	JER Automated	1331.1	1 minute	1/1/2021	10/31/2022
Rabbit	JER Automated	1326.9	1 minute	6/15/2016	10/31/2022
Ragged Tank	JER Automated	1439.4	1 minute	1/1/2018	10/31/2022
Red Lake	JER Automated	1318.9	1 minute	1/1/2017	12/31/2020
				1/1/2022	10/31/2022
Rep 2	JER Automated	1317.0	1 minute	1/1/2018	12/31/2020
Road Tank	JER Automated	1412.5	1 minute	1/1/2018	10/31/2022
Ropes Springs	JER Automated	1725.1	1 minute	6/15/2016	12/31/2020
				1/1/2022	10/31/2022
Sandhill	JER Automated	1378.5	1 minute	6/15/2016	12/31/2017
				7/1/2020	4/30/2022
South Well	JER Automated	1313.8	1 minute	6/15/2016	12/31/2020
Taylor Well	JER Automated	1329.4	1 minute	6/15/2016	12/31/2020
Turney Well	JER Automated	1366.7	1 minute	1/1/2017	12/31/2020
Twin Hills	JER Automated	1509.0	1 minute	6/15/2016	12/31/2018
West Well	JER Automated	1323.5	1 minute	1/1/2017	10/31/2022
Wooton	JER Automated	1375.8	1 minute	1/1/2019	8/31/2020
Yucca	JER Automated	1321.1	1 minute	1/1/2018	10/31/2022
Transect 1	Tromble Weir	1456.3	1 minute	10/9/2016	10/31/2022

Gauge Name	Gauge Network	Elevation (m)	Temporal Resolution	Start of Data	End of Data
Transect 2	Tromble Weir	1457.4	1 minute	10/9/2016	10/31/2022
Transect 3	Tromble Weir	1463.2	1 minute	10/9/2016	10/31/2022
Plots 1&2	Tromble Weir	1460.6	1 minute	9/7/2019	10/31/2022
Plots 3&4	Tromble Weir	1460.5	1 minute	9/7/2019	10/31/2022
Tower	Tromble Weir	1470.2	1 minute	10/9/2016	10/31/2022

Citations for the NPP and CSIS gauge data, which are published on the Environmental Data Initiative (EDI) Data Portal, are included below:

Anderson, J. 2023a. Jornada Basin LTER: Wireless meteorological station at NPP T-EAST site: 1-second summary precipitation data: 2013 - ongoing ver 32. Environmental Data Initiative. https://doi.org/10.6073/pasta/75ae07283533103f36ee381a711a903d (Accessed 2023-07-24).

Anderson, J. 2023b. Jornada Basin LTER: Wireless meteorological station at NPP C-CALI site: 1-second summary precipitation data: 2013 - ongoing ver 33. Environmental Data Initiative. https://doi.org/10.6073/pasta/b0ac88e8832eb366e90d9241d8cf8877 (Accessed 2023-07-24).

Anderson, J. 2023c. Jornada Basin LTER: Wireless meteorological station at NPP P-COLL site: 1-second summary precipitation data: 2013 - ongoing ver 31. Environmental Data Initiative. https://doi.org/10.6073/pasta/973fe0271c8ac25544ff54a7802d11b9 (Accessed 2023-07-24).

Anderson, J. 2023d. Jornada Basin LTER: Wireless meteorological station at NPP M-WELL site: 1-second summary precipitation data: 2013 - ongoing ver 32. Environmental Data Initiative. https://doi.org/10.6073/pasta/087fe2e955fc44651ee399a0b996a5b5 (Accessed 2023-07-24).

Anderson, J. 2023e. Jornada Basin LTER: Wireless meteorological station at NPP M-RABB site: 1-second summary precipitation data: 2013 - ongoing ver 32. Environmental Data Initiative. https://doi.org/10.6073/pasta/f4e10183c929d9613a00eb4d08149450 (Accessed 2023-07-24).

Anderson, J. 2023f. Jornada Basin LTER: Wireless meteorological station at NPP M-NORT site: 1-second summary precipitation data: 2013 - ongoing ver 31. Environmental Data Initiative. https://doi.org/10.6073/pasta/b35845416b69e86ec62d110efbaab32b (Accessed 2023-07-24).

Anderson, J. 2023g. Jornada Basin LTER: Wireless meteorological station at NPP G-SUMM site: 1-second summary precipitation data: 2013 - ongoing ver 32. Environmental Data Initiative. https://doi.org/10.6073/pasta/28b4e00e30c4e5b24a9476d9bc33b933 (Accessed 2023-07-24).

Anderson, J. 2023h. Jornada Basin LTER: Wireless meteorological station at NPP G-IBPE site: 1-second summary precipitation data: 2013 - ongoing ver 33. Environmental Data Initiative. https://doi.org/10.6073/pasta/243488de45cd5f104a2fd3a9c8c9c80a (Accessed 2023-07-24).

Anderson, J. 2023i. Jornada Basin LTER: Wireless meteorological station at NPP G-BASN site: 1-second summary precipitation data: 2013 - ongoing ver 34. Environmental Data Initiative. https://doi.org/10.6073/pasta/e8f1f4c9ab8d5ba8d28409bde0b24559 (Accessed 2023-07-24).

Anderson, J. 2023j. Jornada Basin LTER: Wireless meteorological station at NPP T-WEST site: 1-second summary precipitation data: 2013 - ongoing ver 32. Environmental Data Initiative. https://doi.org/10.6073/pasta/d5ad418031b14daaa082f6b30f417eeb (Accessed 2023-07-24).

Anderson, J. 2023k. Jornada Basin LTER: Wireless meteorological station at NPP P-SMAL site: 1-second summary precipitation data: 2017 - ongoing ver 30. Environmental Data Initiative. https://doi.org/10.6073/pasta/c80d68d77a90e05a55b81c290a81bd3d (Accessed 2023-07-24).

Anderson, J. 2023l. Jornada Basin LTER: Wireless meteorological station at NPP C-GRAV site: 1-second summary precipitation data: 2013 - ongoing ver 31. Environmental Data Initiative. https://doi.org/10.6073/pasta/5221fceca2eabadd41f8aa121f22df64 (Accessed 2023-07-24).

Anderson, J. 2023m. Jornada Basin LTER: Wireless meteorological station at NPP T-TAYL site: 1-second summary precipitation data: 2013 - ongoing ver 31. Environmental Data Initiative. https://doi.org/10.6073/pasta/cf4f503c7f24b9ac5ebc9fe3ac09abb9 (Accessed 2023-07-24).

Anderson, J. 2023n. Jornada Basin LTER: Wireless meteorological station at NPP P-TOBO site: 1-second summary precipitation data: 2013 - ongoing ver 31. Environmental Data Initiative. https://doi.org/10.6073/pasta/0a92adad899eb9dedb6cc18563190344 (Accessed 2023-07-24).

Anderson, J. 2023o. Jornada Basin LTER: Wireless meteorological station at NPP C-SAND site: 1-second summary precipitation data: 2013 - ongoing ver 32. Environmental Data Initiative. https://doi.org/10.6073/pasta/039f83202c1014add690b5df2544f605 (Accessed 2023-07-24).

Anderson, J. 2023p. Jornada Basin LTER Cross-scale Interactions Study (CSIS) Block 2 meteorological station: 1-second summary precipitation data: 2017 - ongoing ver 25. Environmental Data Initiative. https://doi.org/10.6073/pasta/0f6125efd76fad0b6070aaa29ac2ed70 (Accessed 2023-07-24).

Anderson, J. 2023q. Jornada Basin LTER Cross-scale Interactions Study (CSIS) Block 10 meteorological station: 1-second summary precipitation data: 2017 - ongoing ver 27. Environmental Data Initiative. https://doi.org/10.6073/pasta/6adc90c8ad7461446a418dd61b6d5f81 (Accessed 2023-07-24).

Anderson, J. 2023r. Jornada Basin LTER Cross-scale Interactions Study (CSIS) Block 14 meteorological station: 1-second summary precipitation data: 2017 - ongoing ver 26. Environmental Data Initiative. https://doi.org/10.6073/pasta/93fe9fce86e1f0e4eb28815cc546d4a1 (Accessed 2023-07-24).

Anderson, J. 2023s. Jornada Basin LTER Cross-scale Interactions Study (CSIS) Block 15 meteorological station: 1-second summary precipitation data: 2017 - ongoing ver 27. Environmental Data Initiative. https://doi.org/10.6073/pasta/053ed25dae850516116f7872620fcde5 (Accessed 2023-07-24).

Anderson, J. 2023t. Jornada Basin LTER Cross-scale Interactions Study (CSIS) Block 13 meteorological station: 1-second summary precipitation data: 2017 - ongoing ver 27. Environmental Data Initiative. https://doi.org/10.6073/pasta/2fbd1678816461fd7daa2861ae7d76fd (Accessed 2023-07-24).

Anderson, J. 2023u. Jornada Basin LTER Cross-scale Interactions Study (CSIS) Block 11 meteorological station: 1-second summary precipitation data: 2017 - ongoing ver 28. Environmental Data Initiative. https://doi.org/10.6073/pasta/556b75e669609e7637e7d35033de06e1 (Accessed 2023-07-24).

Anderson, J. 2023v. Jornada Basin LTER Cross-scale Interactions Study (CSIS) Block 3 meteorological station: 1-second summary precipitation data: 2017 - ongoing ver 26. Environmental Data Initiative. https://doi.org/10.6073/pasta/ff7e34fea6ce10ce76057d294ec7b324 (Accessed 2023-07-24).

Anderson, J. 2023w. Jornada Basin LTER Cross-scale Interactions Study (CSIS) Block 4 meteorological station: 1-second summary precipitation data: 2017 - ongoing ver 27. Environmental Data Initiative. https://doi.org/10.6073/pasta/a5971c3cbfb90b5017bafee54c34ea56 (Accessed 2023-07-24).

Anderson, J. 2023x. Jornada Basin LTER Cross-scale Interactions Study (CSIS) Block 6 meteorological station: 1-second summary precipitation data: 2017 - ongoing ver 25. Environmental Data Initiative. https://doi.org/10.6073/pasta/cb7ca23a30919d3af3288929939fce88 (Accessed 2023-07-24).

Anderson, J. 2023y. Jornada Basin LTER Cross-scale Interactions Study (CSIS) Block 7 meteorological station: 1-second summary precipitation data: 2017 - ongoing ver 26. Environmental Data Initiative. https://doi.org/10.6073/pasta/416d8eccebd0cad4e7399fe8870b9669 (Accessed 2023-07-24).

Anderson, J. 2023z. Jornada Basin LTER Cross-scale Interactions Study (CSIS) Block 8 meteorological station: 1-second summary precipitation data: 2017 - ongoing ver 27. Environmental Data Initiative. https://doi.org/10.6073/pasta/ae21020297f8df352e957dca0444ccb6 (Accessed 2023-07-24).

Anderson, J. 2023aa. Jornada Basin LTER Cross-scale Interactions Study (CSIS) Block 9 meteorological station: 1-second summary precipitation data: 2017 - ongoing ver 27. Environmental Data Initiative. https://doi.org/10.6073/pasta/af957aebe091b18abe7c13c496a453b0 (Accessed 2023-07-24).

Anderson, J. 2023bb. Jornada Basin LTER Cross-scale Interactions Study (CSIS) Block 5 meteorological station: 1-second summary precipitation data: 2017 - ongoing ver 26. Environmental Data Initiative. https://doi.org/10.6073/pasta/57d436f6648fcc6d173b126ce0b8b533 (Accessed 2023-07-24).

APPENDIX D

PLAYA CATCHMENT DELINEATION

This appendix describes the playa catchment delineation process used to delineate the playa catchments analyzed in this thesis, specifically the extra steps taken since the playas are endorheic basins. A Word document version of the catchment delineation guide can be found in the shared Dropbox folder "KIMSAL_DIGITAL_APPENDIX" in the subfolder "APPENDIX_D," which can be accessed through the following link: https://www.dropbox.com/sh/uwg3ncpejd3wr1h/AADg8twJorODZqExkNnV98_Ea?dl=0.

The problem with the traditional delineation process is that the playas will get filled and there will be no more drainage points. That is why this method "burns a hole" in the DEM where playas are located. This guide explains how to burn the holes in the DEM in ArcMap 10.7.1. Two general comments for this process are that nothing should be saved to a geodatabase and the .tif extension should be added to the filenames of the output rasters. Saving to geodatabases and not adding the .tif extension to the filename of the output raster resulted in errors while delineating the playa catchments. For each step, it should be verified that the correct output is obtained so that errors can be resolved and the correct outputs can be achieved.

Identifying and Creating the Holes

1. If no shapefiles are available for the playas or other sinks in the area of interest, these will have to be identified. There are tools that exist to identify sinks, but for this work they were identified visually based on the DEM and satellite imagery. If one is not already provided, a shapefile should be created for these holes.

2. The holes can be polygons that partially or fully cover the playas/sinks, or they can be points located within the playas/sinks. Both methods have worked to similar degrees of success. If these are not provided, they should be manually created and added to the holes shapefile.
3. Once the holes are all identified and added to the shapefile, one of the attributes in the attribute table must be edited to a value of -1000 for each hole. This is to easily identify them once added to the DEM.
4. The holes shapefile needs to be converted to a raster in order to add it to the DEM. This can be done using the Conversion Tools > To Raster and either the Polygon to Raster or Point to Raster tools. The Input Feature will be the holes shapefile, the Value field will be the attribute that was changed to -1000, and the cellsize should be specified to the resolution of the DEM.

Burning the Holes in the DEM

5. The holes must be mosaicked into the DEM using the Data Management Tools > Raster > Raster Dataset > Mosaic to New Raster tool. The key settings for this step are the Input Rasters, for which the DEM should be listed above the holes raster; the Pixel Type, which should be "16_BIT_SIGNED"; the number of bands, which should be 1; the Mosaic Operator, which should be "MINUMUM"; and the Mosaic Colormap Mode, which should be "LAST". The output location and filename also need to be specified.

6. Now, with the mosaicked raster, the cells with holes need to be set to “NoData” pixels. This can be done using the Spatial Analyst Tools > Map Algebra > Raster Calculator tool. The expression should be:

    SetNull(“dem_with_holes” == -1000, “dem_with_holes”)

    where “dem_with_holes” is the DEM that has been mosaicked with the hole raaster. This step essentially converts all raster values of -1000, which are the holes, to “NoData” pixels.

Delineating the Catchments

7. If the above step has worked correctly, the “Fill” tool can be used as in the traditional catchment delineation process and the areas with playas/sinks will not be filled.
8. Next, the “Flow Direction”, “Flow Accumulation”, and “Watershed” tools can be used to continue with the delineation. It is important to use the “Snap Pour Point” tool to create the pour point and make sure all streams flowing into the playa are captured. The ideal pour point is a raster of the playa polygon.
9. It’s possible that the “Watershed” tool may produce a result with some gaps in the watershed or multiple polygons when converted to a shapefile. These polygons can be edited and joined to create a single polygon for the playa catchment.
10. If the resulting catchment seems unrealistic or included other sinks or playas within it, those should be added to the holes shapefile and the process should be repeated to exclude those areas.

APPENDIX E

INUNDATED AREA AND VOLUME RELATIONSHIPS

This appendix contains the inundated areas and volumes for each playa for water depths from 1 to 100 cm that were derived from the LiDAR DEM. The tables presented in this appendix are stored an two Excel files in the shared Dropbox folder "KIMSAL_DIGITAL_APPENDIX" in the subfolder "APPENDIX_E," which can be accessed through the following link: https://www.dropbox.com/sh/wtp9s79p14fmxin/AAAf7T-1d4ymJwoLP_F7ZQqba?dl=0.

The five tables each show the values for nine playas, with three tables for inundated area (m^2) and two tables for inundation volumes (m^3), and extend over multiple pages. The column headers for all tables show the corresponding playa numbers.

Table E1. DEM-derived inundated areas for Playas 3-11 in units of m^2, for depths of 1-100 cm.

Depth (cm)	3	5	6	7	9	11
1	11184	15924	168	14677	597	77322
2	12666	16922	290	17084	652	78057
3	14664	17805	550	19643	738	78906
4	16060	18569	926	21793	834	79655
5	17472	19495	1083	24591	943	80346
6	18753	20058	1408	27756	1088	81037
7	19913	20659	1715	31345	1253	81701
8	20991	21309	2015	35160	1461	82380
9	21590	21918	2292	39348	1624	82874
10	22561	22544	2545	45032	1782	83582
11	23535	23181	3028	49512	1947	84331
12	24456	23594	3390	53863	2097	85003

Depth (cm)	3	5	6	7	9	11
13	25435	24310	3800	58093	2211	85665
14	26342	24958	4190	62185	2385	86298
15	27618	25627	4537	66053	2512	87105
16	28499	26279	4921	69832	2698	87788
17	29291	26949	5073	72253	2904	88567
18	30045	27801	5428	75506	3091	89305
19	30789	28438	5749	78490	3287	90012
20	31489	29022	6062	81289	3508	90759
21	32187	29620	6350	84029	3737	91479
22	32538	30186	6633	86681	3959	91986
23	33105	30731	6988	90655	4187	92755
24	33679	31099	7225	93664	4414	93534
25	34295	31630	7492	96546	4671	94389
26	34896	32130	7714	99232	4949	95285
27	35477	32681	7944	101460	5160	96143
28	36286	33244	8182	103692	5404	97374
29	36847	33772	8404	104845	5646	98378
30	37398	34465	8553	106729	5912	99365
31	37956	34962	8771	108462	6199	100461
32	38587	35461	8982	110082	6472	101585
33	39352	35928	9206	111730	6810	102641
34	39802	36387	9419	113274	7051	103379
35	40748	36879	9653	115274	7282	104342
36	41748	37335	10002	116612	7533	105311
37	42689	37670	10303	117969	7758	106295
38	43744	38136	10552	119354	8001	107363
39	44765	38680	10819	120544	8224	108473

Depth (cm)	3	5	6	7	9	11
40	46308	39297	11069	121714	8395	109927
41	47319	39918	11300	122736	8602	111271
42	48468	40506	11447	123455	8807	112620
43	49675	41327	11692	124521	9010	113966
44	50988	41966	11929	125573	9219	115329
45	52475	42731	12167	126647	9426	116567
46	53902	43497	12408	127709	9693	117924
47	54536	44262	12654	128779	9902	118827
48	55794	44983	12974	130226	10111	120086
49	57022	45434	13179	131394	10337	121292
50	58144	46136	13404	132536	10548	122546
51	59226	46793	13636	133702	10772	123768
52	60232	47438	13921	134896	10923	125003
53	61666	48099	14181	136022	11115	126508
54	62664	48753	14479	136822	11306	127717
55	63563	49638	14720	137941	11525	129067
56	64453	50340	15053	139113	11733	130341
57	65228	51069	15379	140228	11948	131513
58	66032	51716	15701	141377	12193	132648
59	66510	52359	16061	142571	12414	133351
60	67338	52973	16368	144045	12634	134522
61	68135	53600	16823	145251	12852	135818
62	68937	54082	17159	146458	13078	137056
63	69744	54744	17476	147639	13293	138231
64	70557	55447	17793	148811	13495	139450
65	71712	56134	18111	150126	13644	141139
66	72544	56798	18391	151418	13858	142329

Depth (cm)	3	5	6	7	9	11
67	73384	57432	18633	152308	14115	143467
68	74196	58285	18943	153580	14374	144628
69	75125	58961	19217	154812	14619	145718
70	76069	59691	19526	156112	14843	146875
71	77033	60341	19850	157357	15092	148058
72	77593	60983	20154	158545	15307	148814
73	78591	61701	20571	160052	15505	150105
74	79558	62218	20896	161343	15699	151426
75	80575	62902	21222	162678	15928	152662
76	81584	63599	21570	163998	16120	153820
77	82667	64296	21873	165305	16267	154979
78	84405	65000	22228	166593	16504	156614
79	85661	65644	22537	167583	16708	157788
80	86853	66440	22775	168883	16932	158964
81	87952	67219	23125	170174	17174	160045
82	89053	67939	23412	171488	17412	161075
83	90154	68659	23761	172814	17668	162128
84	90744	69380	24104	174125	17887	162733
85	91759	70070	24462	175753	18103	163731
86	92831	70822	24894	177096	18299	164674
87	93866	71359	25247	178397	18528	165595
88	94939	72120	25592	179681	18752	166603
89	95976	72834	25966	180924	18952	167551
90	97276	73554	26364	182180	19101	168855
91	98172	74329	26714	183436	19334	169786
92	99085	75019	26998	184374	19535	170759
93	99992	75957	27397	185625	19728	171801

Depth (cm)	3	5	6	7	9	11
94	100917	76691	27774	186889	19896	172816
95	101856	77403	28170	188036	20088	173836
96	102855	78128	28593	189182	20341	174760
97	103429	78849	29025	190343	20558	175307
98	104343	79544	29557	191853	20781	176254
99	105247	80063	30006	193051	20999	177153
100	106058	80792	30410	194212	21208	178035

Table E2. DEM-derived inundated areas for Playas 12-22 in units of m^2, for depths of 1-100 cm.

Depth (cm)	12	14	17	18	21	22
1	17363	5497	8742	1870	689	769
2	17828	6332	10864	1945	892	826
3	18230	7308	14136	2025	1065	891
4	18619	8538	16550	2103	1251	945
5	19023	9811	18863	2235	1474	1031
6	19437	11167	21211	2315	1655	1096
7	19834	12897	23637	2394	1837	1147
8	20060	14331	26074	2478	2064	1221
9	20409	15614	27458	2558	2320	1276
10	20759	16870	29911	2635	2650	1323
11	21118	18057	32375	2699	3007	1388
12	21466	19077	35089	2780	3248	1429
13	21801	20013	38041	2865	3541	1496
14	22212	20686	41786	2960	3861	1562

Depth (cm)	12	14	17	18	21	22
15	22519	21468	47778	3060	4160	1628
16	22756	22147	52221	3177	4438	1695
17	23020	22799	56756	3319	4722	1783
18	23260	23418	60977	3429	5081	1890
19	23524	23996	65012	3536	5372	1968
20	23758	24653	69086	3622	5677	2043
21	23946	25154	73332	3720	5967	2128
22	24192	25659	76187	3814	6240	2194
23	24420	26149	81510	3895	6544	2251
24	24678	26682	87920	3980	6763	2299
25	24937	27252	95719	4093	7017	2385
26	25192	27708	105421	4190	7259	2454
27	25485	28364	116026	4307	7479	2523
28	25739	29028	131613	4432	7716	2596
29	26021	29705	142384	4539	7937	2678
30	26281	30363	152079	4704	8211	2805
31	26565	30990	161350	4818	8459	2895
32	26850	31737	170389	4939	8719	2990
33	27067	32323	179297	5080	8961	3079
34	27363	32915	184812	5221	9185	3194
35	27675	33459	193794	5351	9461	3306
36	28010	33984	203200	5468	9707	3423
37	28364	34455	212405	5620	9880	3512
38	28702	34897	221452	5773	10122	3621
39	29144	35217	230420	5922	10361	3742
40	29545	35634	242785	6073	10632	3849
41	29983	36016	251542	6214	10907	3956

Depth (cm)	12	14	17	18	21	22
42	30439	36386	259586	6417	11203	4087
43	30823	36744	266878	6570	11571	4288
44	31213	37092	273789	6727	11859	4481
45	31564	37509	280590	6874	12155	4686
46	31841	37864	287276	7017	12446	4895
47	32240	38197	291497	7178	12796	5118
48	32645	38585	298190	7328	13106	5329
49	33038	38989	304864	7486	13346	5471
50	33514	39457	311416	7649	13658	5713
51	33924	39858	317889	7834	13964	5911
52	34417	40419	323803	8003	14304	6137
53	34841	41107	331589	8172	14623	6377
54	35258	41732	337098	8328	14938	6593
55	35699	42314	342637	8527	15315	6919
56	36164	42846	348339	8713	15671	7156
57	36651	43490	354000	8890	15989	7383
58	36935	43945	359556	9060	16326	7622
59	37364	44412	363130	9209	16670	7828
60	37804	44885	368834	9379	17000	8031
61	38200	45287	374382	9527	17307	8216
62	38588	45660	379919	9701	17546	8381
63	39002	46028	385580	9910	17864	8624
64	39554	46286	391229	10127	18175	8819
65	39957	46647	398618	10320	18508	9055
66	40333	46946	403847	10517	18799	9253
67	40727	47269	408850	10722	19076	9480
68	41148	47544	413460	10906	19454	9775

Depth (cm)	12	14	17	18	21	22
69	41538	47816	418185	11090	19750	9997
70	41928	48160	422587	11297	20024	10199
71	42180	48419	426756	11523	20320	10444
72	42545	48668	429268	11716	20641	10672
73	42916	48914	433258	11944	20947	10880
74	43309	49169	437015	12125	21150	11066
75	43639	49438	440745	12352	21435	11292
76	43963	49643	444598	12588	21685	11522
77	44363	49905	448687	12833	21972	11743
78	44678	50164	454445	13076	22248	11948
79	45019	50454	458553	13317	22526	12177
80	45381	50705	462522	13564	22822	12442
81	45738	50987	466373	13781	23075	12678
82	46057	51349	470180	13999	23326	12942
83	46319	51624	474198	14180	23569	13227
84	46620	51895	476845	14403	23830	13458
85	46919	52183	481234	14623	24050	13721
86	47257	52443	485872	14808	24310	14024
87	47588	52720	490434	15023	24505	14251
88	47877	52967	494787	15234	24766	14570
89	48282	53134	499218	15456	25004	14856
90	48674	53372	505036	15684	25231	15150
91	49047	53593	509183	15911	25456	15450
92	49398	53869	513345	16179	25686	15729
93	49741	54137	517475	16411	25981	16109
94	50091	54417	521660	16640	26237	16424
95	50428	54731	525916	16872	26483	16699

Depth (cm)	12	14	17	18	21	22
96	50662	55000	529983	17093	26711	17005
97	51015	55223	532522	17343	26942	17310
98	51341	55476	536149	17581	27166	17634
99	51676	55724	539657	17786	27365	17883
100	52050	55967	543330	18013	27578	18220

Table E3. DEM-derived inundated areas for Playas 23-30 in units of m^2, for depths of 1-100 cm.

Depth (cm)	23	24	25	28	29	30
1	8606	1709	27	1342	29157	8189
2	11257	1851	40	1920	29652	8605
3	13233	1993	67	2839	30220	8980
4	14994	2096	109	4248	30719	9253
5	16761	2197	149	6289	31240	9594
6	18452	2315	190	11115	31764	9878
7	20247	2402	261	14434	32307	10168
8	22015	2466	387	17828	32803	10418
9	23328	2554	463	21098	33163	10648
10	25187	2630	535	24244	33626	10927
11	27107	2688	600	27229	34014	11100
12	29136	2788	689	28165	34356	11311
13	31393	2881	773	31171	34633	11506
14	33689	3010	850	34300	34900	11675
15	36722	3109	895	37815	35278	11830
16	39089	3234	978	41827	35542	11970
17	41378	3371	1070	46622	35804	12104

Depth (cm)	23	24	25	28	29	30
18	43608	3536	1172	57963	36032	12224
19	45757	3718	1254	66729	36282	12365
20	47926	3867	1358	77078	36545	12506
21	49442	4109	1513	88936	36802	12659
22	51477	4379	1631	101642	36994	12843
23	53564	4668	1746	115174	37247	12982
24	55573	4946	1855	129740	37486	13132
25	57495	5213	1974	132792	37734	13306
26	59219	5576	2159	148872	37990	13467
27	61392	5864	2272	165499	38281	13610
28	62937	6173	2431	182660	38624	13741
29	64457	6519	2627	198526	38917	13875
30	65988	6870	2807	213115	39181	14024
31	67452	7221	3024	235815	39451	14189
32	68853	7614	3299	246761	39709	14352
33	70250	7934	3670	257149	39974	14480
34	71134	8377	3949	266972	40169	14656
35	72401	8814	4275	276560	40420	14838
36	73623	9234	4585	285603	40662	14979
37	74809	9694	4933	287486	40912	15134
38	75948	10192	5348	296145	41133	15277
39	77069	10841	5792	304324	41365	15414
40	78563	11320	6078	311829	41656	15563
41	79763	11805	6532	318148	41938	15683
42	80882	12263	6986	323640	42185	15859
43	81859	12733	7412	332525	42453	15987
44	82787	13197	7839	337622	42704	16144

Depth (cm)	23	24	25	28	29	30
45	83679	13549	8282	342923	42948	16337
46	84243	14040	8902	348156	43180	16514
47	85112	14495	9377	353314	43382	16742
48	85950	14933	9843	358369	43611	16955
49	86830	15334	10265	363075	43846	17135
50	87601	15741	10720	364411	44084	17321
51	88448	16243	11142	369113	44337	17492
52	89440	16665	11423	373650	44542	17702
53	90232	17069	11822	377981	44844	17894
54	90978	17428	12246	382007	45084	18039
55	91737	17817	12661	385869	45320	18231
56	92439	18245	13120	392069	45549	18457
57	93167	18693	13617	395410	45779	18655
58	93867	19037	14153	398789	46021	18853
59	94335	19509	14573	402022	46207	19058
60	95011	20031	15053	405301	46460	19319
61	95653	20587	15572	408442	46722	19520
62	96349	21069	16011	409556	46973	19740
63	97040	21625	16518	412829	47182	19983
64	97699	22293	16982	416193	47429	20225
65	98647	22739	17343	419461	47685	20478
66	99423	23179	17876	422636	47891	20682
67	100104	23628	18379	425701	48134	20945
68	100819	24083	18890	430754	48377	21178
69	101487	24571	19384	433697	48592	21408
70	102198	24897	19955	436661	48803	21664
71	102635	25351	20731	439541	49051	21896

Depth (cm)	23	24	25	28	29	30
72	103280	25825	21368	442472	49227	22165
73	103909	26284	21949	445475	49457	22396
74	104599	26721	22520	448534	49700	22635
75	105261	27154	23119	449872	49938	22896
76	105936	27763	23764	453166	50165	23110
77	106766	28220	24199	456567	50401	23353
78	107482	28691	24793	459985	50658	23589
79	108181	29161	25445	463270	50903	23786
80	108852	29649	26092	466700	51122	24024
81	109541	30129	26751	471906	51342	24240
82	110223	30624	27429	475615	51553	24458
83	110980	30984	28231	479670	51793	24668
84	111507	31457	28894	483763	51982	24884
85	112209	31915	29526	488032	52223	25162
86	112962	32394	30160	492477	52409	25383
87	113724	32872	30803	494784	52623	25606
88	114516	33380	31407	499536	52816	25820
89	115293	33933	31980	504269	53019	26045
90	116288	34399	32444	509096	53255	26239
91	117038	34845	33028	513914	53483	26424
92	117781	35334	33665	518708	53687	26635
93	118520	35776	34260	526346	53856	26841
94	119226	36233	34876	531490	54063	27066
95	119998	36593	35550	536404	54273	27258
96	120484	37073	36438	541404	54452	27463
97	121218	37581	37129	546386	54603	27720
98	121902	38057	37786	551778	54805	27932

Depth (cm)	23	24	25	28	29	30
99	122640	38545	38428	557066	54997	28126
100	123390	38998	39107	559664	55192	28307

Table E4. DEM-derived inundation volumes for Playas 3-17 in units of m^3, for depths of 1-100 cm.

Depth (cm)	3	5	6	7	9	11	12	14	17
1	503	1178	2	1045	31	38552	3854	696	1317
2	626	1344	4	1203	37	39329	4030	757	1420
3	762	1519	8	1386	45	40114	4210	827	1545
4	913	1703	14	1594	53	40905	4393	909	1694
5	1077	1893	24	1830	62	41704	4580	1003	1867
6	1256	2090	37	2096	72	42510	4772	1110	2063
7	1447	2292	54	2395	84	43323	4967	1231	2282
8	1649	2501	73	2732	98	44142	5167	1365	2527
9	1861	2715	95	3109	113	44968	5370	1513	2795
10	2084	2937	120	3529	130	45801	5576	1674	3087
11	2316	3164	148	3994	149	46641	5786	1846	3403
12	2558	3398	179	4503	169	47489	5999	2030	3747
13	2810	3639	214	5054	190	48342	6215	2223	4120
14	3070	3886	253	5647	213	49203	6435	2426	4528
15	3340	4140	296	6280	238	50070	6658	2636	4977
16	3619	4401	342	6952	264	50943	6884	2855	5470
17	3906	4668	392	7659	293	51823	7113	3080	6007
18	4201	4942	445	8401	323	52711	7344	3311	6587
19	4504	5221	502	9174	356	53607	7577	3549	7210
20	4814	5508	562	9976	390	54509	7813	3791	7873

Depth (cm)	3	5	6	7	9	11	12	14	17
21	5131	5800	625	10806	427	55419	8051	4040	8577
22	5454	6098	690	11664	465	56336	8292	4293	9327
23	5784	6401	758	12549	505	57261	8535	4552	10127
24	6119	6710	829	13463	548	58193	8781	4815	10990
25	6460	7025	902	14407	594	59134	9029	5084	11927
26	6807	7344	977	15380	642	60083	9280	5359	12955
27	7160	7669	1055	16378	692	61041	9533	5641	14085
28	7519	8000	1135	17399	745	62009	9789	5929	15324
29	7883	8336	1218	18441	801	62986	10047	6223	16673
30	8254	8677	1303	19503	859	63973	10309	6524	18125
31	8629	9023	1390	20582	920	64970	10572	6832	19675
32	9010	9374	1479	21679	984	65978	10839	7145	21316
33	9399	9730	1570	22791	1050	66997	11108	7465	23048
34	9795	10091	1664	23919	1120	68027	11381	7790	24870
35	10200	10457	1760	25062	1191	69067	11656	8121	26781
36	10615	10827	1858	26219	1265	70116	11935	8457	28784
37	11039	11202	1959	27390	1341	71175	12217	8799	30881
38	11474	11582	2063	28574	1420	72245	12503	9145	33068
39	11919	11967	2170	29771	1501	73325	12792	9495	35345
40	12374	12358	2279	30981	1584	74417	13085	9850	37712
41	12840	12755	2390	32201	1669	75521	13382	10208	40168
42	13317	13158	2504	33432	1756	76638	13683	10570	42709
43	13804	13567	2620	34674	1846	77769	13989	10936	45327
44	14304	13982	2739	35926	1937	78913	14298	11305	48017
45	14817	14404	2859	37189	2030	80071	14611	11678	50777
46	15345	14834	2983	38462	2126	81241	14928	12055	53604
47	15887	15272	3108	39746	2224	82424	15249	12434	56498

Depth (cm)	3	5	6	7	9	11	12	14	17
48	16442	15717	3237	41042	2324	83620	15574	12818	59460
49	17009	16169	3367	42348	2426	84829	15903	13205	62487
50	17588	16628	3500	43667	2530	86050	16236	13597	65581
51	18177	17094	3635	44996	2636	87283	16574	13994	68739
52	18776	17566	3772	46338	2745	88528	16915	14396	71958
53	19386	18045	3912	47691	2855	89785	17261	14805	75235
54	20005	18530	4055	49055	2967	91054	17610	15220	78569
55	20635	19022	4201	50430	3082	92334	17964	15641	81958
56	21273	19521	4351	51817	3198	93629	18322	16067	85403
57	21920	20027	4503	53215	3317	94936	18685	16499	88905
58	22574	20540	4659	54625	3438	96254	19053	16935	92462
59	23237	21059	4819	56047	3560	97584	19425	17376	96075
60	23908	21585	4981	57480	3685	98924	19801	17821	99746
61	24587	22117	5147	58926	3813	100278	20182	18271	103473
62	25273	22656	5316	60382	3942	101645	20566	18725	107255
63	25968	23201	5489	61852	4073	103023	20954	19183	111093
64	26672	23753	5665	63333	4207	104413	21347	19644	114988
65	27382	24312	5844	64826	4343	105816	21743	20109	118937
66	28102	24878	6026	66332	4481	107230	22144	20577	122940
67	28830	25450	6212	67850	4621	108657	22548	21049	126994
68	29566	26028	6400	69382	4764	110095	22957	21523	131098
69	30311	26614	6591	70925	4909	111544	23369	22000	135247
70	31065	27206	6785	72482	5057	113004	23786	22480	139443
71	31828	27806	6982	74051	5207	114476	24206	22962	143682
72	32601	28412	7183	75632	5358	115960	24630	23447	147962
73	33384	29025	7387	77225	5512	117457	25058	23934	152282
74	34177	29644	7594	78831	5668	118967	25489	24424	156640

Depth (cm)	3	5	6	7	9	11	12	14	17
75	34979	30271	7804	80449	5826	120490	25924	24917	161036
76	35792	30904	8017	82081	5986	122024	26362	25412	165470
77	36616	31544	8234	83726	6148	123570	26804	25910	169943
78	37451	32192	8454	85384	6312	125128	27248	26411	174459
79	38299	32846	8678	87055	6479	126697	27696	26914	179018
80	39159	33506	8904	88739	6647	128278	28147	27420	183615
81	40031	34174	9134	90436	6818	129871	28602	27929	188254
82	40913	34849	9368	92147	6991	131474	29061	28441	192931
83	41807	35531	9604	93870	7167	133087	29522	28955	197647
84	42712	36221	9843	95607	7344	134711	29987	29472	202403
85	43626	36918	10086	97357	7524	136345	30455	29992	207202
86	44551	37621	10333	99119	7706	137988	30926	30515	212046
87	45486	38332	10583	100895	7890	139641	31401	31040	216937
88	46432	39051	10837	102684	8076	141303	31878	31568	221869
89	47389	39776	11095	104486	8264	142975	32359	32098	226848
90	48355	40509	11356	106300	8454	144657	32843	32631	231871
91	49331	41249	11621	108127	8647	146348	33331	33166	236934
92	50315	41997	11889	109966	8841	148050	33823	33703	242042
93	51309	42752	12162	111818	9038	149760	34318	34244	247190
94	52312	43514	12438	113682	9236	151481	34816	34786	252378
95	53324	44284	12719	115558	9436	153212	35318	35332	257609
96	54345	45061	13003	117446	9639	154953	35824	35880	262881
97	55376	45845	13292	119345	9843	156702	36332	36431	268193
98	56417	46636	13585	121256	10050	158461	36844	36984	273543
99	57466	47434	13882	123180	10258	160230	37360	37540	278927
100	58524	48239	14184	125114	10469	162007	37879	38097	284348

Table E5. DEM-derived inundation volumes for Playas 18-30 in units of m^3, for depths of 1-100 cm.

Depth (cm)	18	21	22	23	24	25	28	29	30
1	167	18	48	244	92	0.1	33	5400	810
2	186	26	56	345	110	1	51	5695	893
3	206	36	64	465	129	1	78	5994	980
4	226	48	74	604	149	2	119	6298	1071
5	248	62	84	760	171	4	179	6607	1166
6	271	78	94	934	193	5	264	6922	1263
7	294	96	105	1125	217	8	380	7241	1364
8	319	115	117	1335	241	11	530	7566	1467
9	344	137	130	1562	266	16	713	7896	1572
10	370	162	142	1808	292	21	928	8230	1680
11	396	190	156	2073	319	26	1175	8569	1790
12	424	221	170	2359	347	32	1452	8911	1902
13	452	255	185	2666	375	40	1759	9256	2015
14	482	293	200	2996	405	48	2098	9604	2131
15	512	334	216	3349	435	56	2472	9954	2248
16	543	377	233	3725	467	66	2885	10308	2367
17	576	423	250	4126	500	77	3345	10665	2488
18	609	472	269	4548	534	88	3864	11024	2609
19	644	524	288	4993	570	100	4456	11385	2732
20	680	580	308	5458	608	114	5136	11749	2856
21	717	638	329	5945	649	128	5921	12115	2982
22	754	698	350	6452	692	144	6824	12484	3110
23	793	762	372	6980	738	161	7855	12856	3239
24	832	829	395	7529	787	179	9020	13230	3369
25	873	898	419	8097	838	198	10333	13606	3501
26	914	969	443	8682	892	218	11807	13985	3635

Depth (cm)	18	21	22	23	24	25	28	29	30
27	957	1043	468	9286	949	241	13446	14366	3770
28	1001	1119	494	9905	1009	264	15257	14751	3906
29	1046	1198	520	10539	1072	290	17227	15138	4044
30	1092	1279	548	11189	1139	318	19343	15529	4184
31	1140	1362	576	11854	1209	348	21593	15922	4325
32	1188	1448	605	12533	1283	380	23962	16317	4468
33	1238	1536	636	13226	1361	415	26441	16715	4612
34	1290	1627	667	13932	1444	452	29022	17116	4758
35	1343	1720	699	14652	1531	493	31701	17519	4905
36	1397	1815	733	15384	1622	537	34476	17924	5054
37	1452	1913	768	16128	1717	584	37342	18332	5204
38	1510	2014	803	16883	1818	635	40293	18743	5356
39	1568	2116	840	17650	1923	690	43328	19156	5510
40	1629	2221	879	18428	2033	750	46437	19571	5664
41	1690	2330	918	19217	2148	814	49610	19988	5821
42	1753	2441	958	20019	2268	883	52840	20409	5978
43	1818	2555	1000	20831	2392	956	56121	20832	6138
44	1885	2671	1044	21652	2522	1033	59454	21257	6298
45	1953	2791	1089	22483	2655	1114	62838	21685	6461
46	2022	2914	1137	23322	2794	1200	66275	22115	6625
47	2093	3040	1187	24170	2938	1291	69764	22548	6791
48	2165	3169	1239	25027	3085	1387	73303	22983	6960
49	2240	3302	1293	25893	3237	1487	76893	23421	7130
50	2315	3437	1349	26766	3393	1591	80531	23861	7302
51	2393	3576	1408	27648	3553	1700	84214	24303	7476
52	2472	3717	1468	28537	3717	1813	87944	24747	7651
53	2554	3863	1531	29434	3885	1930	91718	25194	7829

Depth (cm)	18	21	22	23	24	25	28	29	30
54	2636	4011	1597	30339	4057	2051	95532	25644	8009
55	2721	4163	1664	31251	4233	2176	99385	26095	8190
56	2807	4317	1735	32171	4413	2306	103274	26549	8374
57	2895	4476	1807	33098	4597	2441	107200	27006	8560
58	2984	4637	1882	34032	4786	2580	111160	27465	8747
59	3076	4802	1959	34973	4979	2723	115153	27926	8937
60	3168	4970	2038	35921	5178	2870	119179	28389	9129
61	3263	5141	2119	36876	5382	3023	123236	28855	9323
62	3360	5315	2202	37837	5592	3180	127327	29324	9519
63	3458	5493	2288	38805	5806	3342	131450	29795	9717
64	3558	5673	2375	39780	6026	3509	135606	30268	9918
65	3661	5857	2465	40762	6250	3681	139795	30744	10121
66	3765	6044	2557	41751	6480	3858	144015	31222	10327
67	3872	6234	2651	42748	6713	4040	148267	31702	10535
68	3980	6427	2748	43751	6951	4227	152549	32184	10746
69	4090	6622	2846	44762	7194	4419	156863	32669	10959
70	4201	6821	2947	45779	7442	4617	161206	33155	11175
71	4315	7022	3050	46804	7694	4821	165579	33644	11393
72	4432	7227	3156	47835	7951	5030	169980	34136	11613
73	4550	7435	3263	48872	8212	5246	174412	34629	11836
74	4670	7645	3373	49915	8478	5468	178874	35125	12061
75	4793	7859	3485	50966	8748	5695	183367	35624	12288
76	4918	8075	3600	52023	9023	5929	187892	36125	12518
77	5045	8293	3716	53087	9302	6169	192451	36628	12750
78	5175	8514	3835	54157	9586	6415	197044	37133	12984
79	5307	8739	3956	55234	9875	6667	201669	37640	13221
80	5442	8965	4079	56319	10169	6926	206327	38150	13460

Depth (cm)	18	21	22	23	24	25	28	29	30
81	5578	9195	4205	57410	10467	7192	211020	38662	13701
82	5717	9426	4332	58507	10771	7464	215749	39177	13945
83	5858	9661	4463	59612	11079	7742	220516	39693	14191
84	6001	9897	4596	60725	11392	8028	225323	40212	14439
85	6146	10137	4732	61844	11710	8319	230173	40734	14689
86	6293	10379	4871	62972	12032	8617	235065	41257	14941
87	6442	10623	5012	64107	12359	8922	240001	41782	15196
88	6594	10869	5157	65250	12692	9232	244986	42310	15452
89	6748	11118	5305	66400	13028	9549	250018	42839	15711
90	6904	11370	5455	67558	13370	9871	255097	43370	15973
91	7062	11624	5609	68724	13716	10199	260224	43904	16236
92	7223	11879	5765	69897	14066	10534	265400	44439	16501
93	7385	12138	5925	71077	14422	10874	270626	44977	16769
94	7551	12399	6087	72265	14781	11221	275902	45516	17038
95	7718	12662	6252	73460	15146	11574	281230	46058	17310
96	7888	12928	6421	74663	15515	11935	286607	46601	17584
97	8060	13196	6592	75872	15889	12302	292034	47147	17860
98	8234	13467	6767	77089	16268	12676	297511	47694	18138
99	8411	13740	6944	78314	16652	13057	303042	48243	18418
100	8591	14015	7125	79545	17040	13444	308627	48794	18700

APPENDIX F

PHOTOS

This appendix contains select photos of the study area and playas. The photos in this appendix, in addition to photos of each individual playa are saved in the shared Dropbox folder "KIMSAL_DIGITAL_APPENDIX" in the subfolder "APPENDIX_F," which can be accessed through the following link: https://www.dropbox.com/sh/ejw1mqucs74q9ru/AAD2jn1V_zzLynjnbj2hJbkra?dl=0.

Figure F1. Drone photograph of the basin floor and Playa 17 facing North (Credit to Zhaocheng Wang).

Figure F2. Water level sensor at Playa 17, representative of how the sensors are installed at all playas.

Figure F3. Temperature/RH sensor on the fringe of Playa 17, representative of how the sensors are installed at all playas.

Figure F4. Flooding at Playa 5 in July 2008 (Credit to John Anderson).

Figure F5. Playa 5 with lush, green grasses in early September 2022.

Figure F6. Water level sensor at Playa 6 surrounded by vertisol-like soil trampled by cattle.

Figure F7. Large channel leading from dirt road to Playa 6.

Figure F8. Channel leading to Play 23, located in the sandy region of the basin floor with abundant mesquite coppice dunes.

Figure F9. Barren surface of Playa 28, with the water level sensor and an eddy covariance tower in the background.

APPENDIX G

FIGURES AND MATLAB SCRIPTS

This appendix describes the main MATLAB scripts used for data analysis and the creation of the figures in the thesis. Scripts and figure files are located in the shared Dropbox folder "KIMSAL_DIGITAL_APPENDIX" in the subfolder "APPENDIX_G," which can be accessed through the following link: https://www.dropbox.com/sh/vvfk5czbgurca1r/AAAL1SA3XCFjCOu3CLLDhNp_a?dl=0.

Figures and Tables

The majority of the figures in this thesis were generated in MATLAB and ArcMap. Figures 1, 2, 3, 5, 6, 7, 8, 10, 11, 26, and 29 were generated in ArcMap 10.7.1. Figure 32 was generated in the statistical software JMP Pro version 16.0.0. Figures 42 and 43 are images that came from other sources. Figure 4 was created in Microsoft PowerPoint, and figures 3, 8, 10, 11, 15, and 29 were edited in PowerPoint to add explanatory features, such as arrows or labels. All the other figures were created entirely in MATLAB. Within the "APPENDIX_G" folder, the folder titled "figures" contains subfolders titled with the naming convention "fig_XX_identifier" where XX is the figure number and identifier is a short description of the figure for quicker reference. Each figure's folder contains a MATLAB script (*.m) or ArcMap document (*.mxd) with the same name as the folder, a subfolder containing the data used to construct the figure or a reference to another digital appendix where the data is stored, and a final version of the figure as a *.png file and MATLAB figure file (*.fig). The folders for figures not generated in MATLAB or ArcMap contain information about the source or how the the figure was created, as well as the final version as a *.png file. The tables in this thesis are

stored in Excel files that are named with the table number in the “tables” folder located in “APPENDIX_G.”

MATLAB Scripts

The “analysis_scripts” folder located in “APPENDIX_G” contains the major MATLAB scripts used for the data analysis in this thesis.

The script called “hourly_rainfall_metrics.m” calculates the hourly rainfall metrics for each playa catchment and can use the corrected or raw hourly MRMS grids. This version loops through each playa and saves the metrics to a MATLAB structure file for each one, the save location of which can be changed. The metrics calculated in this script are the spatially averaged rainfall depth over the whole catchment, the spatial average of just the rainfall values within the catchment (core rainfall), the rainfall volume, the maximum intensity within the catchment, the mean intensity across the catchment, and the distance from the storm centroid to the playa.

The script “runoff_ratios.m” calculates the mean annual and mean monsoon season runoff ratios for all playa catchments. The script “correlate_inundation_rain_events” matches inundation event data to rainfall event data to find which rainfall events did and did not cause inundation. The script “determine_threshold” calculates the optimal inundation threshold for each playa based on the highest kappa agreement statistic and stores the thresholds and performance metrics. The script “historical_analysis” uses the historical rainfall data and calculates inundation threshold exceedances, calculates historical inundation volumes, and performs

Mann-Kendall tests for trend significance. These scripts are included in the

"APPENDIX_G" folder as well as in the text below.

hourly_rainfall_metrics.m

```
%% Calculation of Hourly Rainfall metrics
% Total rainfall for each hour within each catchment.
%       Spatial avg. including zeros based on proportion of
catchment in
%       each pixel
% Core rainfall - Spatial average of just rainfall pixels
based on the proportion of
%       the rainfall-experiencing catchment in each pixel.
% Total rainfall volume - sum of pixel values within the
catchment,
%       weighted by the percentage of each pixel within the
catchment, account
%       for units.
% Maximum I60 in a pixel fully or partially in the
catchment, each hour find max, then daily
%       max or event max later.
% Mean I60 is essentially the average pixel value in the
catchment,
% including pixels partially within the catchment with
equal weight
% Storm Distance - distance of storm centroid away from
playa centroid (km)
%
% Need - "mask" of each catchment with percentages of
pixels. Multiply
% this by rainfall grid, get the "weighted" matrix for each
hour, then do
% averages, sums, etc.
load("MRMS_corrected_hourly.mat"); % Can use corrected or
raw grid
grids=MRMS_corrected_hourly.grids;
dates=MRMS_corrected_hourly.dates;
depth_mask_list=dir('playa_*_catchment.mat');
vol_mask_list=dir('catch_*_mask.mat');
for i=1:18
    % Load catchment and playa polygon masks
```

```
    vol_catchfile=vol_mask_list(i).name;
    playa_no=vol_catchfile(7:8);
    load(vol_catchfile); % called "catch_mask"
    depth_catchfile=depth_mask_list(i).name;
    load(depth_catchfile); % called "playa_catchment"
    mat_name_poly=sprintf('playa_%s_poly.mat',playa_no);
    load(mat_name_poly);
    % Playa centroid
    playa_loc=double(cell2mat({playa_poly>0}));
    cent_playa = regionprops(true(size([playa_loc])),
playa_loc, 'WeightedCentroid');
    % Initialize vectors
    precip_amt=nan(55920,1);
    precip_amt_core=nan(55920,1);
    precip_vol=nan(55920,1);
    max_i60=nan(55920,1);
    mean_i60=nan(55920,1);
    storm_dist=nan(55920,1);
    % Loop through each hour
    for j=1:55920
        weighted_grid=grids(:,:,j).*catch_mask;
        precip_vals=weighted_grid(weighted_grid>=0.1);
        core_mask=playa_catchment.*(grids(:,:,j)>=0.1);
        rainfall_area=sum(core_mask,[1 2],'omitnan');
        i60_mask=(catch_mask>0).*grids(:,:,j);
        if precip_vals % If there was precipitation

precip_amt(j,1)=squeeze(sum(grids(:,:,j).*playa_catchment,[
1 2],'omitnan')); % Must be sum!!

precip_amt_core(j,1)=precip_amt(j,1)/rainfall_area; %
Spatial average of only rainfall pixels
            precip_vol(j,1)=(sum(precip_vals)/1000)*(10^6);
% Vol in cubic meters
            max_i60(j,1)=max(i60_mask,[],'all'); % Max I60
in a pixel
            mean_i60(j,1)=mean(i60_mask(i60_mask>0),[1 2]);
% Mean i60
            cent_storm=regionprops(true(size([i60_mask])),
i60_mask, 'WeightedCentroid'); % Storm distance from playa

storm_dist(j,1)=sqrt(((cent_storm.WeightedCentroid(1)-
cent_playa.WeightedCentroid(1))^2)+((cent_storm.WeightedCen
troid(2)-cent_playa.WeightedCentroid(2))^2));
        else % No precipitation
            precip_amt(j,1)=0;
```

```
            precip_amt_core(j,1)=0;
            precip_vol(j,1)=0;
            max_i60(j,1)=0;
            mean_i60(j,1)=0;
            storm_dist(j,1)=NaN;
        end
    end
    % Save metrics to a structure
    struct_name=sprintf('C:\\Users\\ckims\\Dropbox
(ASU)\\ms_data\\MRMS\\rain_metrics\\playa_%s_rain_metrics.m
at',playa_no);
    rain_metrics.dates=dates;
    rain_metrics.amounts=precip_amt;
    rain_metrics.core_amounts=precip_amt_core;
    rain_metrics.volumes=precip_vol;
    rain_metrics.intensity=max_i60;
    rain_metrics.mean_intensity=mean_i60;
    rain_metrics.distance=storm_dist;
    save(struct_name,'rain_metrics')
end
```

runoff_ratios.m

```
%% Runoff Ratios for playa catchment
playa_ids=[3,5,6,7,9,11,12,14,17,18,21,22,23,24,25,28,29,30
];
annual_ratios=nan(18,1); % Table of avg annual ratios for
all playas
monsoon_ratios=nan(18,1); % Table of avg monsoon season
ratio for all playas
% Loop through playas
for n=1:18
    playa_no=playa_ids(n);
    % Load playa event info
    playa_data=sprintf('p%02d_event_info.mat',playa_no);
    load(playa_data);
    % Calculate inundation volumes
    load('playa_vols.mat')
    vol_col=all_vols(:,n);
    num_floods=length(event_info.max_levels);
    max_volumes=nan(num_floods,1);
    % Loop through inundation events
    for v=1:num_floods
        depth=round(event_info.max_levels(v)*100);
```

```
        if depth>100
            max_volumes(v,1)=vol_col(100);
        else
            max_volumes(v,1)=vol_col(depth);
        end
    end

    % Monthly inundation volumes
    flood_dates=event_info.start_times;
    flood_tt=timetable(flood_dates,max_volumes);
    flood_monthly=retime(flood_tt,'monthly','sum');

    % Load precipitation data

mat_name_catch_precip=sprintf('playa_%02d_rain_metrics_raw.
mat',playa_no);
    load(mat_name_catch_precip); % Load Precip data (MRMS),
could be for catchment or playa
    dates_all=rain_metrics.dates;
    precip_all=rain_metrics.volumes;
    precip_tt=timetable(dates_all',precip_all);
    monthly_precip=retime(precip_tt,'monthly','sum');
    monthly_precip_2=monthly_precip(2:end,:); % remove June
2016 (only have half month)
    precip_months=datevec(monthly_precip_2.Time);
    load('reg2_factors_monthly.mat'); % Correction factors
for monthly precip
    monthly_factors(isnan(monthly_factors))=1;
    % Corrected monthly precip

precip_correct=(monthly_precip_2.precip_all).*monthly_facto
rs;

    % Create table to line up inundation and precip months
    monthly_vols=zeros(height(monthly_precip_2),1);
    for m=1:height(flood_monthly)

idx_mon=find(monthly_precip_2.Time==flood_monthly.flood_dat
es(m));

monthly_vols(idx_mon,1)=flood_monthly.max_volumes(m);
    end


monthly_table_all=timetable(monthly_precip_2.Time,monthly_v
ols,precip_correct);
```

```
    % Only monsoon months (JAS)

monthly_monsoons=monthly_table_all([1,2,3,13,14,15,25,26,27
,37,38,39,49,50,51,61,62,63,73,74,75],:);
    % Annual Ratios

yearly_table_all=retime(monthly_table_all,'yearly','sum');
    % Yearly ratios excluding 2016 and 2022

yearly_ratios=yearly_table_all.Var1(2:6)./yearly_table_all.
Var2(2:6);
    avg_ratio=mean(yearly_ratios);

    % Loop to calculate runoff ratio for each monsoon
season
    monsoons=nan(7,3);
    num=[1,4,7,10,13,16,19]; % indices of start of each
season
    for j=1:length(num)
        start_ind=num(j);

monsoons(j,1:2)=sum(monthly_monsoons{start_ind:start_ind+2,
1:2});
        monsoons(j,3)=monsoons(j,1)./monsoons(j,2);
    end

    % Calculate average ratio over monsoon seasons
    avg_monsoon_ratio=mean(monsoons(:,3));

    % Store in table for all playas
    monsoon_ratios(n,1)=avg_monsoon_ratio;

    % Store in table for all playas
    annual_ratios(n,1)=avg_ratio;
end
```

correlate_inundation_rain_events.m

```
%% Correlate inundation and rainfall event data
%% Results in rainfall metric and inundation tables for all
playas that have corresponding rows
playa_ids=[3,5,6,7,9,11,12,14,17,18,21,22,23,24,25,28,29,30
];
inundation_table=nan(700,18); % Inundation volumes
```

```
event_rain_table=nan(700,18); % Rainfall depth
event_vol_table=nan(700,18); % Rainfall volume
event_intensity_table=nan(700,18); % Max i60
event_mi60_table=nan(700,18); % Mean i60
event_distance_table=nan(700,18); % storm distance to playa
event_durations_table=nan(700,18); % Rainfall duration
interevent_table=nan(700,18); % Time since last rainfall
event_months_table=nan(700,18); % Month of rainfall
num_storms_table=nan(18,1); % Number of storms at each
playa
num_flood_table=nan(18,1); % Number of floods at each playa
% Loop through playas
for n=1:18
    playa_no=playa_ids(n);
    % Load playa data
    playa_data=sprintf('p%02d_event_info.mat',playa_no);
    load(playa_data);
    % Calculate inundation volumes
    load('playa_vols.mat')
    vol_col=all_vols(:,n);
    num_floods=length(event_info.max_levels);
    max_volumes=nan(num_floods,1);
    for v=1:num_floods
        depth=round(event_info.max_levels(v)*100);
        if depth>100
            max_volumes(v,1)=vol_col(100);
        else
            max_volumes(v,1)=vol_col(depth);
        end
    end
    % Load precip event data

storm_data=sprintf('p%02d_rain_event_info.mat',playa_no);
    load(storm_data);
    num_storms=length(rainfall_events.amounts);
    flood_events=zeros(num_storms,1);
    % Loop through floods to find corresponding storm
    for s=1:num_floods
        % find storm that started most recently before
inundation occurred
        time_diffs=event_info.start_times(s,1)-
rainfall_events.start_times;
        time_diffs(time_diffs<"-1:00:00")=nan;
        [minimum, min_ind]= min(time_diffs);
        % place inundation volume in same row as
corresponding storm
```

```
        flood_events(min_ind,1)=max_volumes(s,1);
    end
    inundation_table(1:num_storms,n)=flood_events;

event_rain_table(1:num_storms,n)=rainfall_events.amounts;

event_vol_table(1:num_storms,n)=rainfall_events.volumes;

event_intensity_table(1:num_storms,n)=rainfall_events.inten
sities;

event_mi60_table(1:num_storms,n)=rainfall_events.mean_inten
sities;

event_distance_table(1:num_storms,n)=rainfall_events.distan
ces;

event_durations_table(1:num_storms,n)=rainfall_events.durat
ions;
    % Interevent durations
    gaps=rainfall_events.start_times(2:end,:)-
rainfall_events.end_times(1:end-1,:);
    interevent=[1000;time2num(gaps,'hours')];
    interevent_table(1:num_storms,n)=interevent;
    % Get months
    event_start_dates=datevec(rainfall_events.start_times);
    event_months=event_start_dates(:,2);
    event_months_table(1:num_storms,n)=event_months;
    num_storms_table(n,1)=num_storms;
    num_flood_table(n,1)=num_floods;
    %% Delete missing dates
    nan_idcs=find(rainfall_events.start_times>'2020-11-12
00:00:00' & rainfall_events.start_times<'2021-03-27
23:00:00');
    if n==1
        nan_idcs=find(rainfall_events.start_times>'2020-06-
18 00:00:00' & rainfall_events.start_times<'2021-03-27
23:00:00');
    end
    inundation_table(nan_idcs,n)=nan;
    event_rain_table(nan_idcs,n)=nan;
    event_vol_table(nan_idcs,n)=nan;
    event_intensity_table(nan_idcs,n)=nan;
    event_mi60_table(nan_idcs,n)=nan;
    event_distance_table(nan_idcs,n)=nan;
    event_durations_table(nan_idcs,n)=nan;
```

```
    interevent_table(nan_idcs,n)=nan;
    event_months_table(nan_idcs,n)=nan;
end
```

determine_threshold.m

```
%% Determine P or I60 threshold
thresh_table = NaN(18,6);
for playa=1:18

    % X and Y data, should be 18 column table for playas
    Y=inundation_table(:,playa);
    X=rain_table(:,playa);

    % Only consider precip values greater than 1 mm
    Y=Y(X>1);
    X=X(X>1);

    % Number of observations
    N_OBS = length(X);

    P_OBS_FLOW = sum(Y>0)/length(X);
    P_OBS_NOFLOW = 1-P_OBS_FLOW;

    % Range of thresholds to test
    T = 0.1:0.1:100;

    % Initialize performance metrics
    p0 = NaN(length(T),1);
    k = NaN(length(T),1);
    FP = NaN(length(T),1);
    FN = NaN(length(T),1);

    for ind = 1:length(T)

        % Indices correctly predicted above threshold

        IND_DUM = X>T(ind);

        N_Flow_Above_Threshold = sum(Y(IND_DUM) > 0);

        % Indices correctly predicted below threshold

        IND_DUM_2 = X<T(ind);
```

```
        N_NoFlow_Below_Threshold = sum(Y(IND_DUM_2) == 0);

        % Calculate p0

        p0(ind) = (N_Flow_Above_Threshold +
N_NoFlow_Below_Threshold)/N_OBS;

        % Calculate pe

        pT_flow = sum(IND_DUM)/N_OBS;
        pT_noflow = sum(IND_DUM_2)/N_OBS;
        pe = P_OBS_FLOW * pT_flow + P_OBS_NOFLOW *
pT_noflow;

        % Calculate k

        k(ind) = (p0(ind) - pe)/(1 - pe);

        % Calculate FP and FN

        FP(ind) = (sum(Y(IND_DUM) == 0)/N_OBS)*100;
        FN(ind) = (sum(Y(IND_DUM_2) > 0)/N_OBS)*100;

    end

    % Find the maximum kappa

    [Max_k, IND_MAX] = max(k);

    % Your threshold is:

    threshold = T(IND_MAX);

    p0_val = p0(IND_MAX);
    FP_val = FP(IND_MAX);
    FN_val = FN(IND_MAX);

    thresh_table(playa,1) = playa_ids(playa);
    thresh_table(playa,2) = threshold;
    thresh_table(playa,3) = p0_val;
    thresh_table(playa,4) = Max_k;
    thresh_table(playa,5) = FP_val;
    thresh_table(playa,6) = FN_val;

end
```

historical_analysis.m

```
%% Historical analysis script
%% Convert historical precip to mm
precip_dates=longtermprecip1914{:,6};
precip_in=longtermprecip1914{:,7};
precip_mm=precip_in.*25.4;

%% Separate into time periods
early_precip=precip_mm(523:36008,1);
early_dates=precip_dates(523:36008,1);
early_years=[1916:1:2015]';
study_precip=precip_mm(36170:38452,1);
study_dates=precip_dates(36170:38452,1);

%% Daily thresholds
daily_thresholds=[39.4;33.0;16.8;48.2;15.1;33.0;15.3;15.2;2
0.4;22.3;23.0;14.5;29.9;18.9;23.4;29.9;22.3;34.9];

%% Calculate historical volumes, assume threshold
exceedances inundate playa
load('playa_regressions.mat') % contains reg_mat
for p=1:18

flood_dates=early_dates(early_precip>daily_thresholds(p),1)
;

flood_rains=early_precip(early_precip>daily_thresholds(p),1
);
    flood_vols=reg_mat(p,2)+flood_rains.*reg_mat(p,1); %
Based on regressions between daily rainfall and water
volume
    flood_tt=timetable(flood_dates,flood_vols);
    flood_yearly=retime(flood_tt,'yearly','sum');
    yearly_average=sum(flood_yearly.flood_vols)/100;
    yearly_vec=[flood_yearly.flood_vols;zeros(100-
height(flood_yearly),1)];
    avg_vec(p,1)=mean(yearly_vec); % mean annual inundation
    avg_vec(p,2)=std(yearly_vec); % standard deviation of
annual inundation
end

%% Average playa inundation frequency
avg_thresh=22.7; % Median threshold across playas
num_exc=sum(early_precip>avg_thresh); % Num rain events
above the threshold
```

```
exc_dates=early_dates(early_precip>avg_thresh); % Dates of
threshold exceedences
exc_vals=early_precip(early_precip>avg_thresh); % Values of
threshold exceedences
precip_sorted=sort(rmmissing(early_precip),'descend'); %
Sorted precip values to identify top ones
pot_events=early_precip(early_precip>avg_thresh);
pot_dates=early_dates(early_precip>avg_thresh);
pot_datevec=datevec(pot_dates);
idx=1;
sum_vec=nan(100,1);
for j=1916:2015
    num_evs=sum(pot_datevec(:,1)==j);
    sum_vec(idx,1)=num_evs;
    idx=idx+1;
end

% Cool season threshold exceedances, can be easily changed
to warm season
idx=1;
sum_vec_wint=nan(100,1);
for j=1916:2015
    num_evs=sum(pot_datevec(:,1)==j & (pot_datevec(:,2)>9 |
pot_datevec(:,2)<4));
    sum_vec_wint(idx,1)=num_evs;
    idx=idx+1;
end

%% Calculate annual precpip
precip_tt=timetable(precip_dates,precip_mm);
precip_annual=retime(precip_tt,'yearly','sum');
annual_precip=precip_annual.precip_mm(3:103);

%% Mann-Kendall Test for Annual Precip
n=length(annual_precip);
num_tied_groups=0;
deltaP_vec=nan(n-1,1);
for i=2:n
    deltax_precip=annual_precip(i)-annual_precip(1:i-1);
    deltax_precip(deltax_precip<0)=-1;
    deltax_precip(deltax_precip>0)=1;
    s_deltaP=sum(deltax_precip);
    deltaP_vec(i-1,1)=s_deltaP;
end
s_precip=sum(deltaP_vec);
```

```
var_s_precip=(1/18)*(n*(n-1)*(2*n+5));

z_precip=(s_precip-1)/sqrt(var_s_precip);


%% Mann-Kendall Test for Frequency of Large Events
n=length(sum_vec);
num_tied_groups=6;
for t=0:5
    tied_counts(t+1,1)=sum(sum_vec==t);
end
deltaP_vec=nan(n-1,1);
% deltaT_vec=nan(69,1);
for i=2:n
    deltax_precip=sum_vec(i)-sum_vec(1:i-1);
    deltax_precip(deltax_precip<0)=-1;
    deltax_precip(deltax_precip>0)=1;
    s_deltaP=sum(deltax_precip);
    deltaP_vec(i-1,1)=s_deltaP;
end
s_precip=sum(deltaP_vec);

var_s_precip=(1/18)*(n*(n-1)*(2*n+5)-
sum((tied_counts.*(tied_counts-1).*(2*tied_counts+5))));

z_precip=(s_precip-1)/sqrt(var_s_precip);

normcdf(-2)
normpdf(x,0,var_s_precip)

%% Mann-Kendall Test for Frequency of Large Cool Season
Events
n=length(sum_vec_wint);
num_tied_groups=3;
for t=0:2
    tied_counts(t+1,1)=sum(sum_vec_wint==t);
end
deltaP_vec=nan(n-1,1);
for i=2:n
    deltax_precip=sum_vec_wint(i)-sum_vec(1:i-1);
    deltax_precip(deltax_precip<0)=-1;
    deltax_precip(deltax_precip>0)=1;
    s_deltaP=sum(deltax_precip);
    deltaP_vec(i-1,1)=s_deltaP;
end
s_precip=sum(deltaP_vec);
```

```
var_s_precip=(1/18)*(n*(n-1)*(2*n+5)-
sum((tied_counts.*(tied_counts-1).*(2*tied_counts+5))));

z_precip=(s_precip-1)/sqrt(var_s_precip);

%% Calculate number of days with rain each year
precip_logical=precip_mm>0;
days_tt=timetable(precip_dates,precip_logical);
days_annual=retime(days_tt,'yearly','sum');
annual_days=days_annual.precip_logical(3:103);

%% Mann-Kendall Test for Number of days with rain
n=length(annual_days);
num_tied_groups=27;
tied_counts=[3;2;2;4;3;5;2;5;4;6;2;4;4;4;3;6;4;2;6;3;2;2;2;
2;3;2;3];
deltaP_vec=nan(n-1,1);
for i=2:n
    deltax_precip=annual_days(i)-annual_days(1:i-1);
    deltax_precip(deltax_precip<0)=-1;
    deltax_precip(deltax_precip>0)=1;
    s_deltaP=sum(deltax_precip);
    deltaP_vec(i-1,1)=s_deltaP;
end
s_precip=sum(deltaP_vec);

var_s_precip=(1/18)*(n*(n-1)*(2*n+5)-
sum((tied_counts.*(tied_counts-1).*(2*tied_counts+5))));

z_precip=(s_precip-1)/sqrt(var_s_precip);


%% College Playa Floods 1970-1989
pcoll_dates=precip_dates(19398:26379,1);
pcoll_precip=precip_mm(19398:26379,1);
pcoll_thresh=25.3;

% Precip over threshold
exceedence=find(pcoll_precip>pcoll_thresh);
flood_dates=pcoll_dates(exceedence);
```

APPENDIX H

TROMBLE WEIR TELEMETRY NETWORK

This appendix describes the telemetry network at the Tromble Weir watershed and how to remotely connect to the dataloggers. Detailed information about the telemetry equipment, including a parts list and photographs of the equipment setup, a schematic of the network, and screenshots of datalogger and radio settings with explanations in *.txt files, are located in the shared Dropbox folder "KIMSAL_DIGITAL_APPENDIX" in the subfolder "APPENDIX_H," which can be accessed through the following link: https://www.dropbox.com/sh/rzr41ik94v27exw/AAC-bImz3RB1oCn_XeECEE-ma?dl=0.

The purpose of this network is to access data from the Tromble Weir Watershed instrument array remotely as well as monitor the status of the site from ASU to see when sensors go down. Currently, John Anderson is downloading the data via a server running LoggerNet that is scheduled to collect the data each hour. Data is shared via Dropbox as a more permanent data sharing plan is developed.

Communication among the dataloggers within the watershed is through a 900 MHz spread spectrum network. This consists of 9 "slave" radios (RF450 or RF451), connected through the CS/IO port to each of the CR800s collecting data, that use Yagi antennas to send their signal to the "master" RF450 radio connected to a CR800 and omnidirectional antenna at the EC tower. This radio acts as a router and connects through the RS-232 port to an NL201 device that connects via ethernet cable to the Ubiquiti Bullet M2HP radio at the top of the tower that transmits the data to Jornada Headquarters (HQ) using a parabolic grid antenna. The CR5000 is connected to an NL100 device that also connects to the Bullet radio via ethernet. The ethernet switch receiving these two

inputs and sending one cable up to the Bullet radio has one open port that could be used for other devices, such as a PhenoCam.

Some currently known issues with the telemetry network are related to the connection strength between the EC tower and Jornada HQ. This could be improved by placing a repeater Bullet M2HP radio between the tower and headquarters, which the radio at the UTEP tower could potentially function as. Other options are repositioning or better securing the antenna, or simply replacing it. Another current limitation is that the EC tower data is not being downloaded through telemetry due to large file sizes.

Remote Connection to Tromble Weir Dataloggers via LoggerNet

The setup for connecting remotely to the dataloggers in Tromble Weir Watershed is through two IP ports: one for the network of CR800s and one for the tower's CR5000. See "Tromble Weir Datalogger Setup Information" for the necessary IP addresses and PakBus addresses associated with the dataloggers.

Connection to CR800s:

1. Open the LoggerNet Setup Screen and change it from EZ View to Standard View.
2. Click "Add Root"
    a. On the menu that opens, click "IPPort"
        i. This IP port will have an IP address of 128.123.38.219:6782, which can be changed by clicking on the IPPort on the left panel and editing the settings in the "Hardware" tab in the center.

b. Add a PakBusPort to this IPPort, then add a CR800Series device. This will represent the “master” or “PakBus router” CR800 that is located at the EC tower and receives the radio signal from the other stations. Click on this datalogger in the left panel, and on the “Hardware” tab, specify this logger’s PakBus address of 710.
c. For the remaining CR800s, add each device to the master CR800 and specify its PakBus address. Make sure that the master CR800 is highlighted in the left panel when adding these dataloggers so that they will all end up being nested under the master CR800. See the following page for the PakBus addresses of all dataloggers and a screenshot of what the final setup screen should look like. Ports and dataloggers can be named however is convenient.

3. Apply changes.
4. Now in the Connect Screen you should be able to connect to any of these dataloggers.

Connection to CR5000:

1. Open the LoggerNet Setup Screen and make sure it is in Standard View.
2. Click “Add Root”
    a. On the menu that opens, click “IPPort”
        i. This IP port will have an IP address of 128.123.38.219:6781
    b. To add the CR5000 to this IPPort, choose the “Other Loggers” option and then “CR5000”. No PakBus or other information is needed.
3. Apply changes.

Tromble Weir Datalogger Setup Information

CR800 Setup:

IPPort: 128.123.38.219:6782

PakBusPort

Master CR800: PakBus address=710

Outlet Flume: 701

Channel 3: 702

Transect 1: 703

Channel 2: 704

Transect 2: 705

Plots 3 & 4: 706

Plots 1 & 2: 707

Channel 1: 708

Transect 3: 709

CR5000 Setup:

IPPort: 128.123.38.219:6781

EC Tower CR5000